SUPPORTING INFORMATION

Enhanced Electrophilicity of Heterobimetallic Bi-Rh Paddlewheel Carbene Complexes: A Combined Experimental, Spectroscopic and Computational Study

Lee R. Collins, Maurice van Gastel, Frank Neese,* and Alois Fürstner*

Max-Planck-Institut für Kohlenforschung, Mülheim/Ruhr 45470, Germany

Corresponding Author : *fuerstner@kofo.mpg.de

Corresponding Author : *frank.neese@kofo.mpg.de

TABLE OF CONTENTS

GENERAL REMARKS

All reactions were carried out under Argon in flame-dried glassware, ensuring rigorously inert conditions. The solvents were purified by distillation over the indicated drying agents and were stored and handled under Argon: CH_2Cl_2 (CaH_2), chlorobenzene (CaH_2), Ph_2O (CaH_2), hexane (Na/K), pentane (Na/K), toluene (Na/K). NMR spectra were recorded on Bruker AV300 or AV400 spectrometers at 298 K unless otherwise indicated with the chemical shifts (δ) given in ppm relative to TMS and the coupling constants (J) in Hz. The solvent signals were used as references and the chemical shifts converted to the TMS scale (CD_2Cl_2: ^1H = 5.32 ppm, ^{13}C = 53.8 ppm; C_6D_6: ^1H = 7.16 ppm, ^{13}C = 128.0 ppm; $CDCl_3$: ^1H = 7.26 ppm, ^{13}C = 77.0 ppm). ^{19}F NMR resonances were referenced to an internal standard of $C_6H_5CF_3$ (–63.72 ppm). HRMS (ESI): ESQ3000 (Bruker). UV-Vis spectra were recorded at 228 K on a Cary 8454 diode Array UV-Vis spectrometer equipped with an actively temperature controlled cuvette. Raman spectra were recorded on a TriVista 555 triple monochromator equipped with a liquid nitrogen cooled Roper Scientific 400BR Excelon CCD camera, using Cobalt diode lasers at fixed wavelength. The samples were frozen as drops on a pre-cooled glass pipette which was pre-shaped to feature a small loop at the end. A temperature of 100 K was maintained by positioning the frozen droplet into a cold nitrogen gas stream provided by a Cryostream 800 unit. As such, no quartz windows were necessary. The Raman light was collected in 180° using a parabolic silver mirror (with hole for laser excitation) and focused onto the entrance slit of a spectrograph with a 100 mm diameter f/4 lens. The scattered light was dispersed with gratings of 900 mm^{-1}, 900 mm^{-1} and 1800 mm^{-1} at the three different stages, respectively. Slit widths at the first and third stages were set to 50 μm, giving rise to a spectral resolution at the CCD camera of typically 0.8 cm^{-1} (wavelength dependent). Spectra were collected for 30 min for a given wavelength and spectral window; corresponding spectral

windows were despiked, normalized to the solvent band at 300 cm^{-1}. A solvent spectrum has subsequently been subtracted and remaining first derivative lines at the position of the solvent signals resulting from imperfect subtraction have been removed manually. Calibration of the Raman shifts has been achieved to an accuracy of 1 cm^{-1} by using Na_2SO_4 as well as the solvent signals as a reference.

All quantum chemical calculations were carried out using the ORCA quantum chemistry program.[1] Geometry optimization and frequency analysis were performed with the BP86 and B3LYP functionals at the level of density functional theory (DFT).[2] The def2-TZVP basis set was used for all atoms.[3] The resolution of identity RI approximation has been employed to speed up calculation time.[4] Scalar relativistic effects are included in zero order regular approach (ZORA).[5] Broken symmetry calculations invariably converged to a closed-shell singlet wave function. The Cartesian coordinates of all optimized structures are provided as supporting information. Vibrational frequencies and Raman intensities have been calculated from diagonalization of the Hessian matrix and from the polarizability tensor as implemented in ORCA.[1] A Doppler broadening with a band width at half height of 10 cm^{-1} has been used to dress the calculated spectra. The accuracy of this method is typically 25 cm^{-1}.[6] Resonance Raman calculations have been performed as described in reference 7.[7] Assignments are based on comparison of both experimental and calculated band positions and intensities. For calculations of the UV-Vis spectra, the B3LYP functional was used. QTAIM analyses were performed with the AimAll program (TK Gristmill, http://aim.tkgristmill.com/).

SINGLE CRYSTAL X-RAY STRUCTURE ANALYSIS OF BiRh(esp)$_2$·H$_2$O

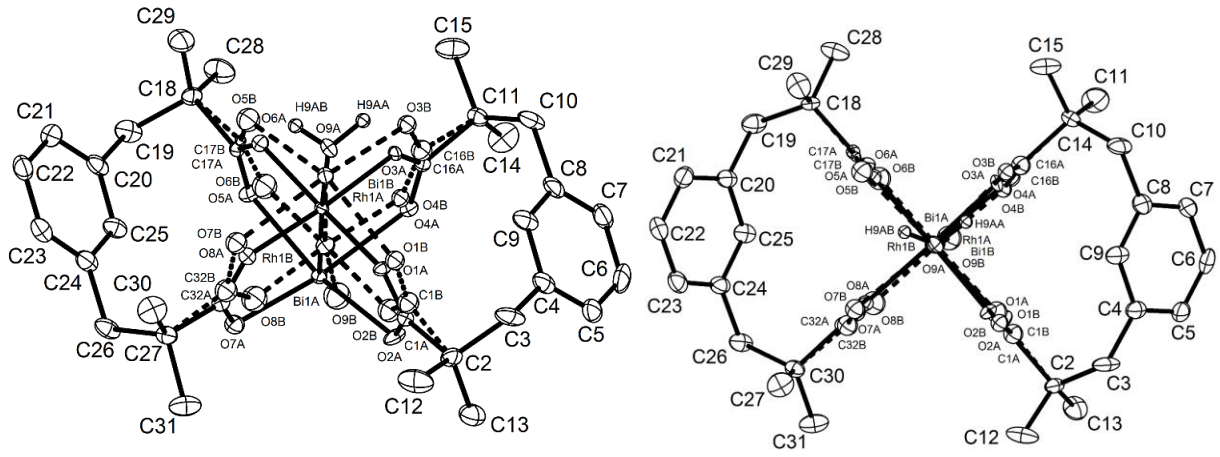

Figure X1. Two views of the molecular structure of bis(μ$_2$-2,2,2',2'-tetramethyl-1,3-benzene-dipropanoato-O,O')-aqua-rhodium-bismuth, BiRh(esp)$_2$·H$_2$O, showing the slight disorder [ca. 28 %] at the core of the molecule (dotted lines).

X-ray Crystal Structure Analysis of BiRh(esp)$_2$·H$_2$O. [$C_{32}H_{41.44}BiO_9Rh$], M_r = 881.98 g · mol^{-1}, light-yellow prism, crystal size 0.023 x 0.062 x 0.103 mm^3, monoclinic, space group *P*c [No. 7], a = 6.5384(7) Å, b = 19.201(2) Å, c = 12.6755(14) Å, β = 92.199(2)°, V = 1590.2(3) Å^3, T = 100(2) K, Z = 2, D_{calc} = 1.842 g · cm^3, λ = 0.71073 Å, μ(*Mo-K*$_\alpha$) = 6.097 mm^{-1}, Gaussian absorption correction (T_{min} = 0.62391, T_{max} = 0.90053), Bruker AXS Enraf-Nonius Kappa Mach3 IμS Apex-II diffractometer, 1.060 < θ < 31.425°, 44832 measured reflections, 10470 independent reflections, 9690 reflections with $I > 2\sigma(I)$, R_{int} = 0.0512.

INTENSITY STATISTICS FOR DATASET

Resolution	#Data	#Theory	%Complete	Redundancy	Mean I	Mean I/s	Rmerge	Rsigma
Inf - 2.84	81	85	95.3	9.39	130.86	79.92	0.0380	0.0109
2.84 - 1.89	189	189	100.0	10.90	107.24	73.27	0.0365	0.0112
1.89 - 1.48	282	282	100.0	11.12	64.56	61.97	0.0459	0.0132
1.48 - 1.29	258	258	100.0	10.84	44.26	50.32	0.0571	0.0164
1.29 - 1.17	288	288	100.0	10.69	44.91	46.22	0.0557	0.0177
1.17 - 1.08	280	280	100.0	10.02	46.78	41.46	0.0533	0.0192
1.08 - 1.02	264	264	100.0	9.75	41.08	38.06	0.0568	0.0218
1.02 - 0.97	254	254	100.0	9.08	33.97	31.75	0.0637	0.0262
0.97 - 0.92	310	310	100.0	8.67	30.60	27.25	0.0707	0.0300
0.92 - 0.89	246	246	100.0	8.41	26.54	23.70	0.0789	0.0346
0.89 - 0.86	263	263	100.0	8.10	24.58	22.04	0.0860	0.0388
0.86 - 0.83	293	293	100.0	7.77	22.78	19.63	0.0958	0.0436
0.83 - 0.80	351	351	100.0	7.44	20.30	17.13	0.1009	0.0504
0.80 - 0.78	272	272	100.0	7.39	19.01	16.04	0.1080	0.0548
0.78 - 0.76	294	294	100.0	7.06	18.63	14.70	0.1071	0.0593
0.76 - 0.75	145	145	100.0	6.88	17.34	13.32	0.1218	0.0643
0.75 - 0.73	340	340	100.0	6.66	16.26	12.33	0.1228	0.0709
0.73 - 0.71	387	387	100.0	6.49	14.46	10.71	0.1432	0.0812
0.71 - 0.70	205	205	100.0	6.47	13.42	10.13	0.1551	0.0890
0.70 - 0.69	216	216	100.0	6.05	12.42	8.45	0.1573	0.1012
0.69 - 0.68	188	199	94.5	5.15	10.85	7.42	0.1807	0.1302
0.78 - 0.68	1775	1786	99.4	6.44	14.98	11.20	0.1335	0.0795
Inf - 0.68	5406	5421	99.7	8.27	32.19	27.73	0.0655	0.0317

The structure was solved by dual methods and refined by full-matrix least-squares against F^2 to R_1 = 0.0418 [$I > 2\sigma(I)$], wR_2 = 0.0887, 469 parameters, 51 restraints. A number of low-angle reflections were shadowed by the beamstop and removed from the data set before the final refinement cycles. The central core of the molecule is slightly (ca. 28 %) disordered (see Figure S1). In addition, the crystal is partially twinned [TWIN -1 0 0 0 1 0 0 0 -1]. Most likely, the crystal is primarily composed of columns of molecules bridged by water that exhibit some local centrosymmetric arrangements ($P2_1/c$). Two crystals were investigated. Both showed similar disorder. Two C-O distances in one of the carboxylate groups of the minor component were restrained to be equal with an effective standard deviation of 0.02. For the disordered atoms C1A, C16A, C17A, C32A, O4A, O6A, O8A, O9A, C1B, C16B, C17B and C32B the Uij components

were restrained to be isotropic with an effective standard deviation of 0.001. The H atoms on the water molecule bonded to Rh1B of the minor component could not be located on a difference Fourier map and were not included in the model. As a result of the disorder, the diffracted intensities decreased more than expected with increasing resolution leading to relatively high goodness of fit for the weak reflections [e.g., 1.875 for Fc/Fcmax 0.0-0.051] and a much higher than expected second term in the WGHT card [7.3772]. The four most disagreeable reflections are given below and refer to weak reflections. None has an error/esd greater than 15. The error/esd is calculated as sqrt(wD^2/<wD^2>) where w is given by the weight formula, D = Fo^2-Fc^2 and <> refers to the average over all reflections. H atoms riding, *S* = 1.222, residual electron density 1.72 (0.69 Å from C32B)/ -3.90 (0.84 Å from Rh1A) e $Å^{-3}$. **CCDC-1847633**.

h	k	l	Fo2	Fc2	Error/esd	Fc/Fc(max)	Resolution(A)
-3	2	1	1253.33	76.12	14.31	0.034	2.11
-3	1	0	1062.29	99.49	11.34	0.039	2.16
-4	1	-2	664.69	28.69	10.88	0.021	1.56
1	1	-8	1358.86	211.12	10.66	0.057	1.55

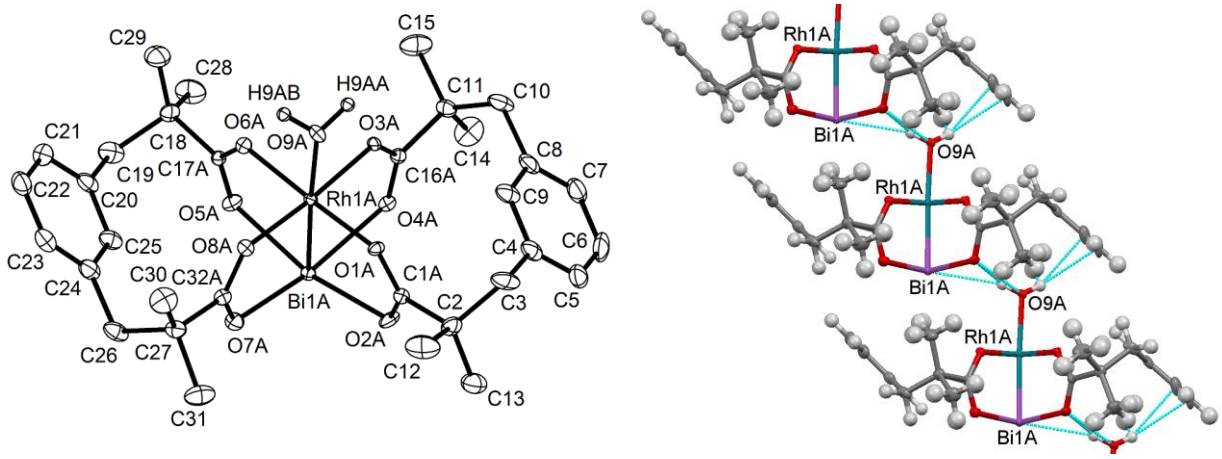

Figure X2. The major (ca. 72 %) component of $BiRh(esp)_2 \cdot H_2O$ and a section of the lattice showing the packing of the molecules in the crystal.

PREPARATIVE DATA

$Bi(TFA)_3$

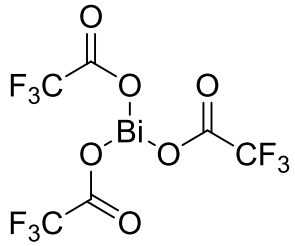

Prepared according to reference 8.[8]

$^{19}F\{^{1}H\}$ NMR (282 MHz, C_6D_6, $C_6H_5CF_3$ as internal standard): δ = -76.0 (s) ppm.

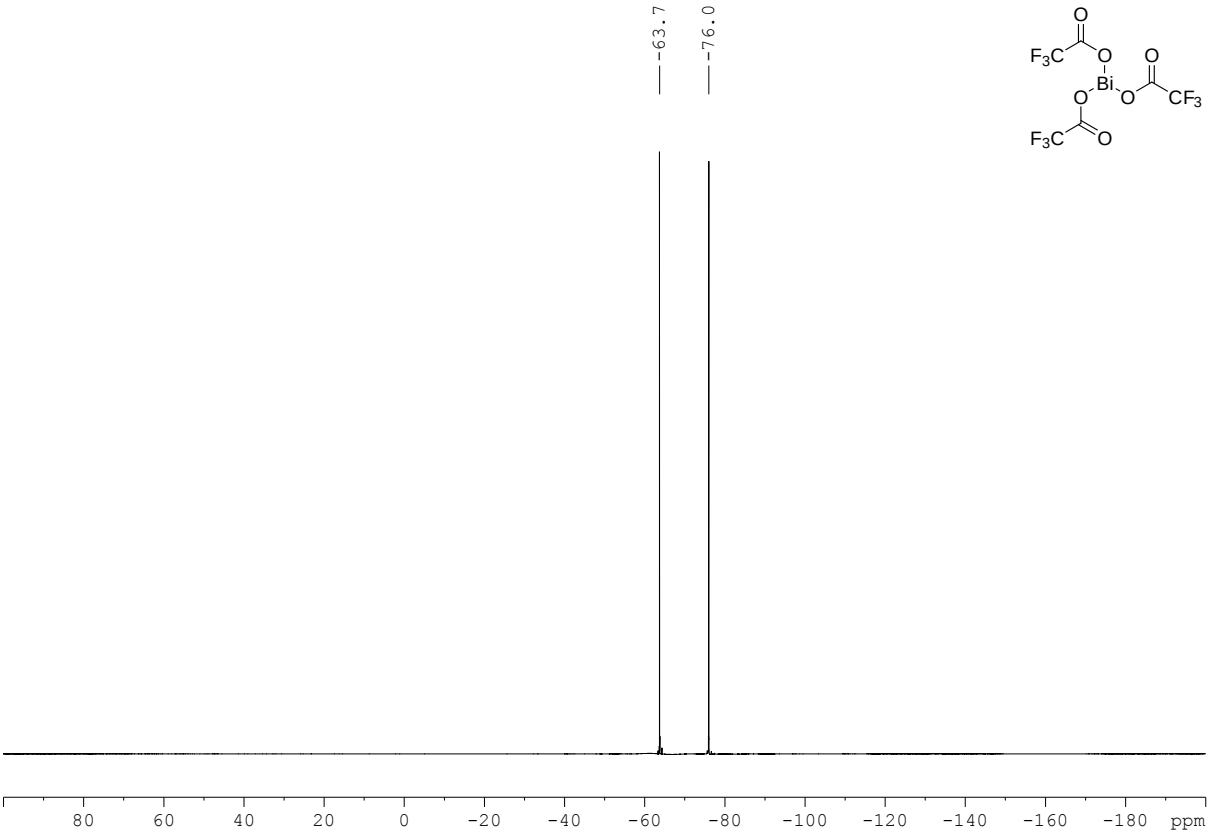

BiRh(TFA)$_4$

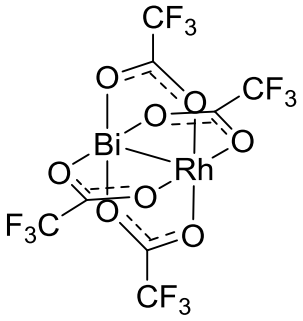

Prepared according to reference 9.[9]

$^{19}F\{^{1}H\}$ NMR (282 MHz, C_6D_6, $C_6H_5CF_3$ as internal standard): δ -74.2 ppm.

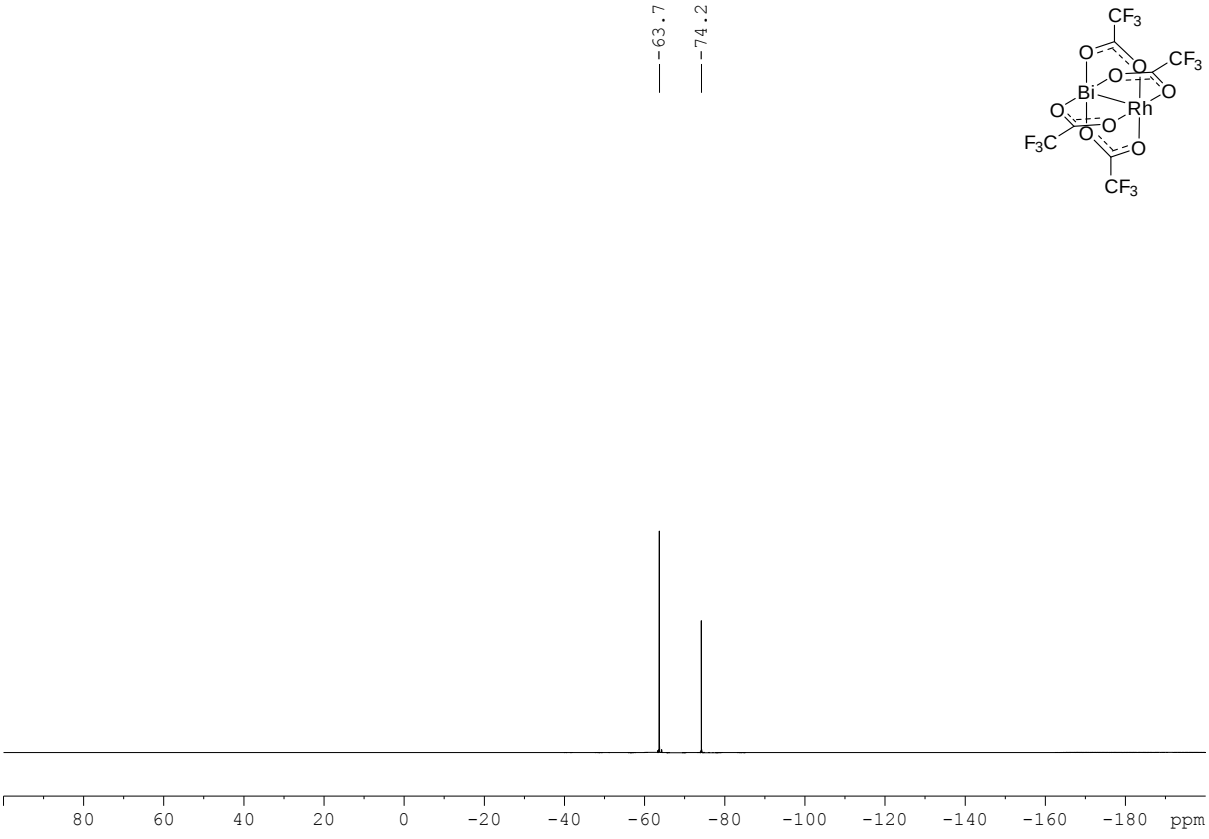

BiRh(Piv)$_4$

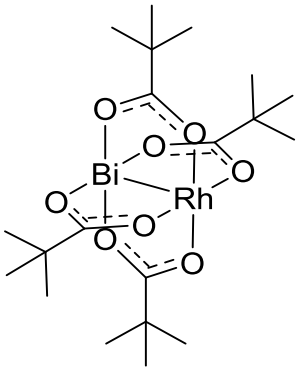

Prepared according to reference 10. Spectroscopic data matched those reported in the literature.[10]

BiRh(TPA)$_4$

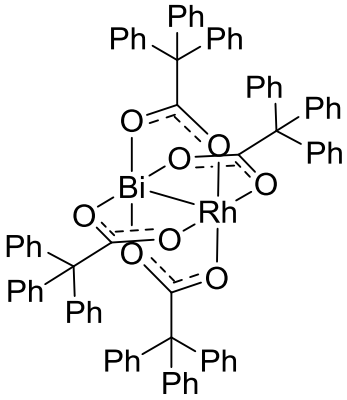

Prepared according to reference 10. Spectroscopic data matched those reported in the literature.[10]

BiRh(esp)$_2$

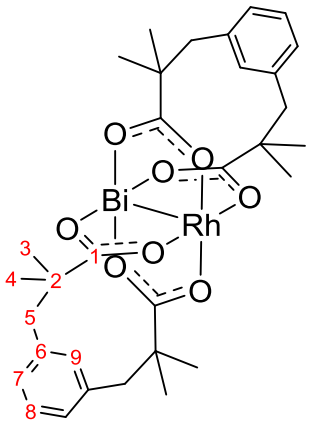

Prepared according to reference 10.[10]

^{1}H NMR (400 MHz, CD_2Cl_2, 298 K): δ = 7.08 (t, 7.6 Hz, 2 H, H_8), 6.88 (dd, 7.6 Hz, 1.6 Hz, 4 H, H_7), 6.74 (br. s, 2 H, H_9), 2.75 (d, 12.7 Hz, 4 H, H_5), 2.59 (d, 12.7 Hz, 4 H, H_5), 1.10 (s, 12 H, H_3), 1.03 (s, 12 H, H_4) ppm.

^{13}C{^{1}H} NMR (100 MHz, CD_2Cl_2, 298 K): δ = 190.3 (s, C_1), 138.5 (s, C_6), 130.8 (s, C_9), 128.5 (s, C_7), 127.2 (s, C_8), 47.9 (s, C_5), 46.0 (s, C_2), 26.7 (s, C_4), 25.5 (s, C_3) ppm.

Single crystals suitable for X-ray diffraction were grown by the following procedure: A sample of BiRh(esp)$_2$ was dissolved in pyridine, filtered and volatiles were removed. The resulting pyridine adduct is significantly more soluble than the unligated complex. Dissolving this sample in CH_2Cl_2, layering with hexane and, after diffusive mixing was complete, allowing the resultant solution to slowly evaporate yielded crystals.

BiRh(esp)$_2$

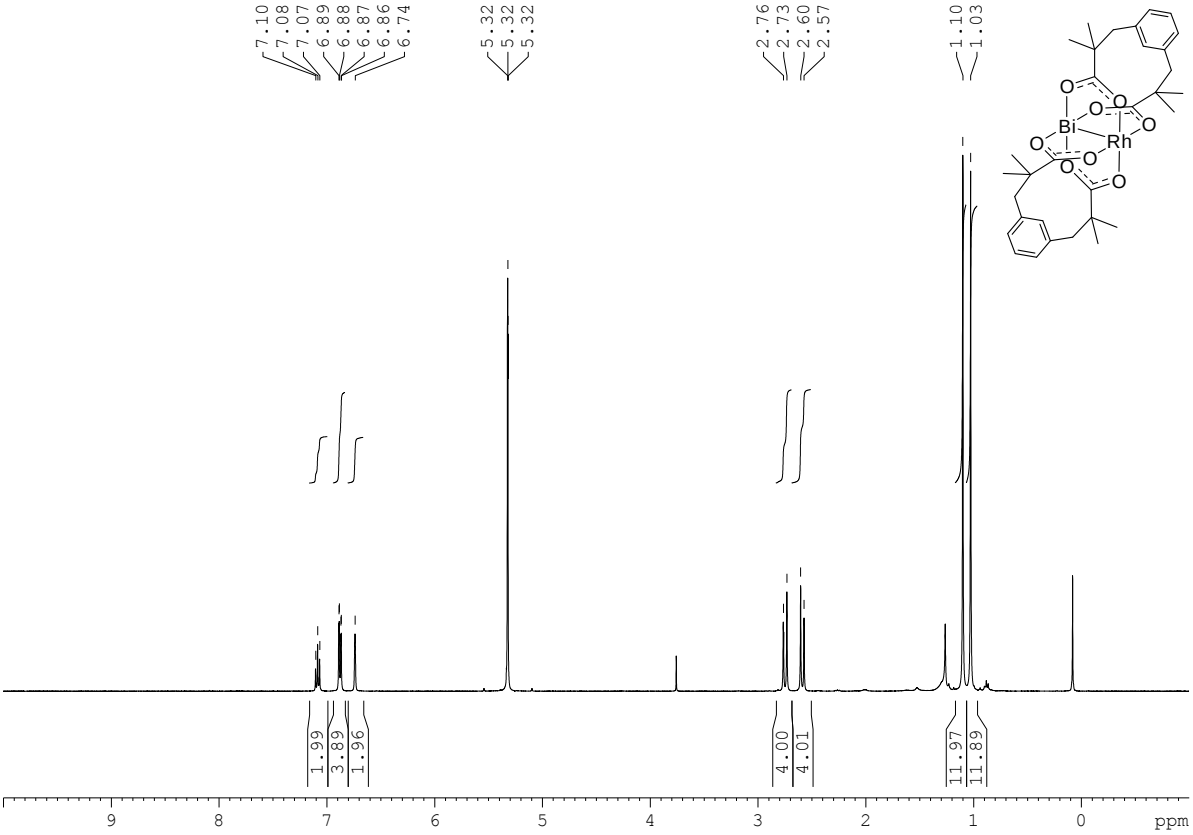
7.10
7.08
7.07
6.89
6.88
6.87
6.86
6.74
5.32
5.32
5.32
2.76
2.73
2.60
2.57
1.10
1.03
1.99
3.89
1.96
4.00
4.01
11.97
11.89
9
8
7
6
5
4
3
2
1
0
ppm
Bi
Rh
O

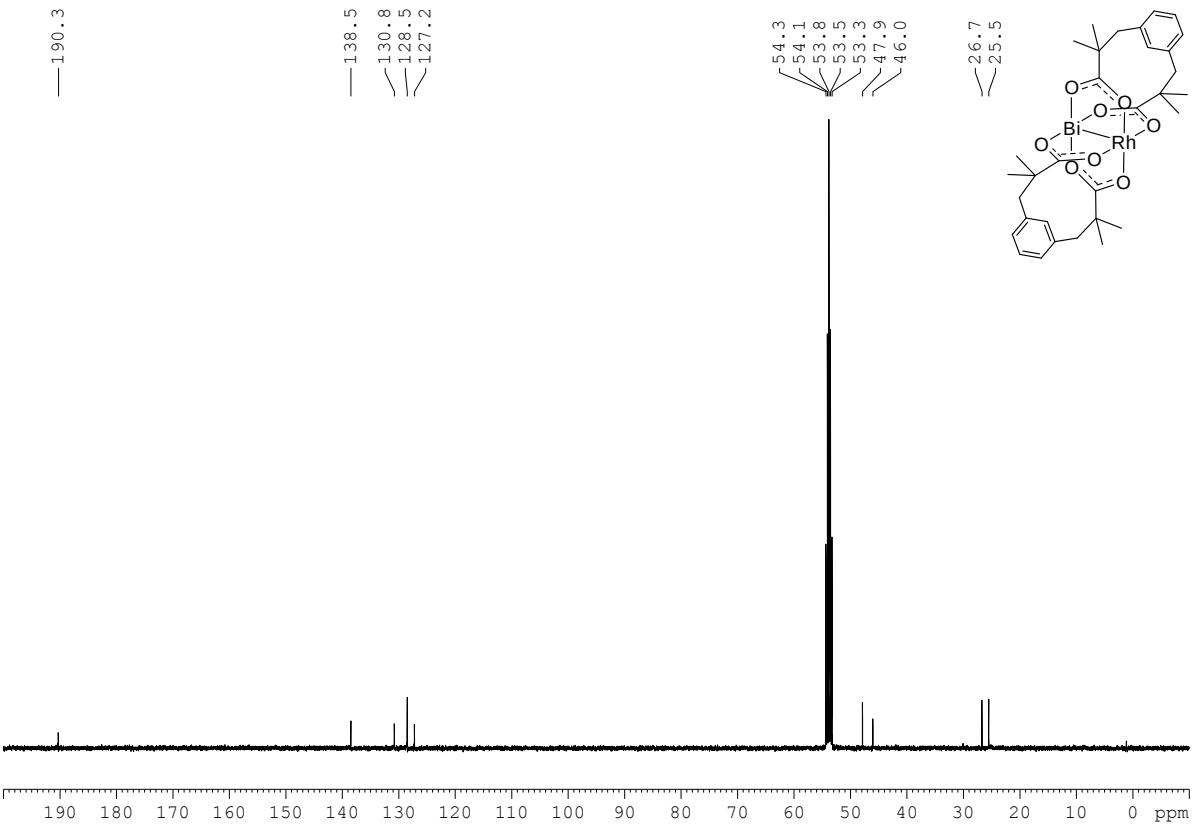
190.3
138.5
130.8
128.5
127.2
54.3
54.1
53.8
53.5
53.3
47.9
46.0
26.7
25.5
190
180
170
160
150
140
130
120
110
100
90
80
70
60
50
40
30
20
10
0
ppm
Bi
Rh
O

$Rh_2(esp)_2$

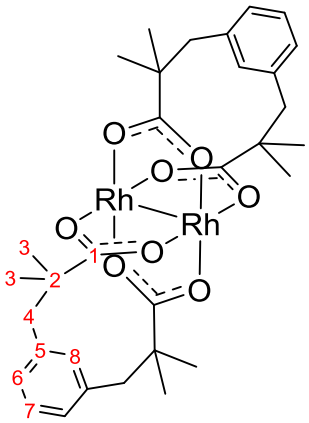

Purchased from Sigma Aldrich and used as received.

^{1}H NMR (400 MHz, CD_2Cl_2, 255 K): δ = 7.08 (t, 7.7 Hz, 2 H, H_7), 6.87-6.83 (overlapping, 6 H, H_6 and H_8), 2.61 (br. s, 8 H, H_4), 0.96 (br. s, 24 H, H_3) ppm.

^{13}C{^{1}H} NMR (100 MHz, CD_2Cl_2, 298 K): δ = 196.9 (s, C_1), 137.9 (s, C_5), 130.9 (s, C_8), 128.0 (s, C_6), 126.9 (s, C_7), 46.7 (s, C_4), 46.4 (s, C_2), 25.3 (s, C_3) ppm.

$Rh_2(esp)_2$

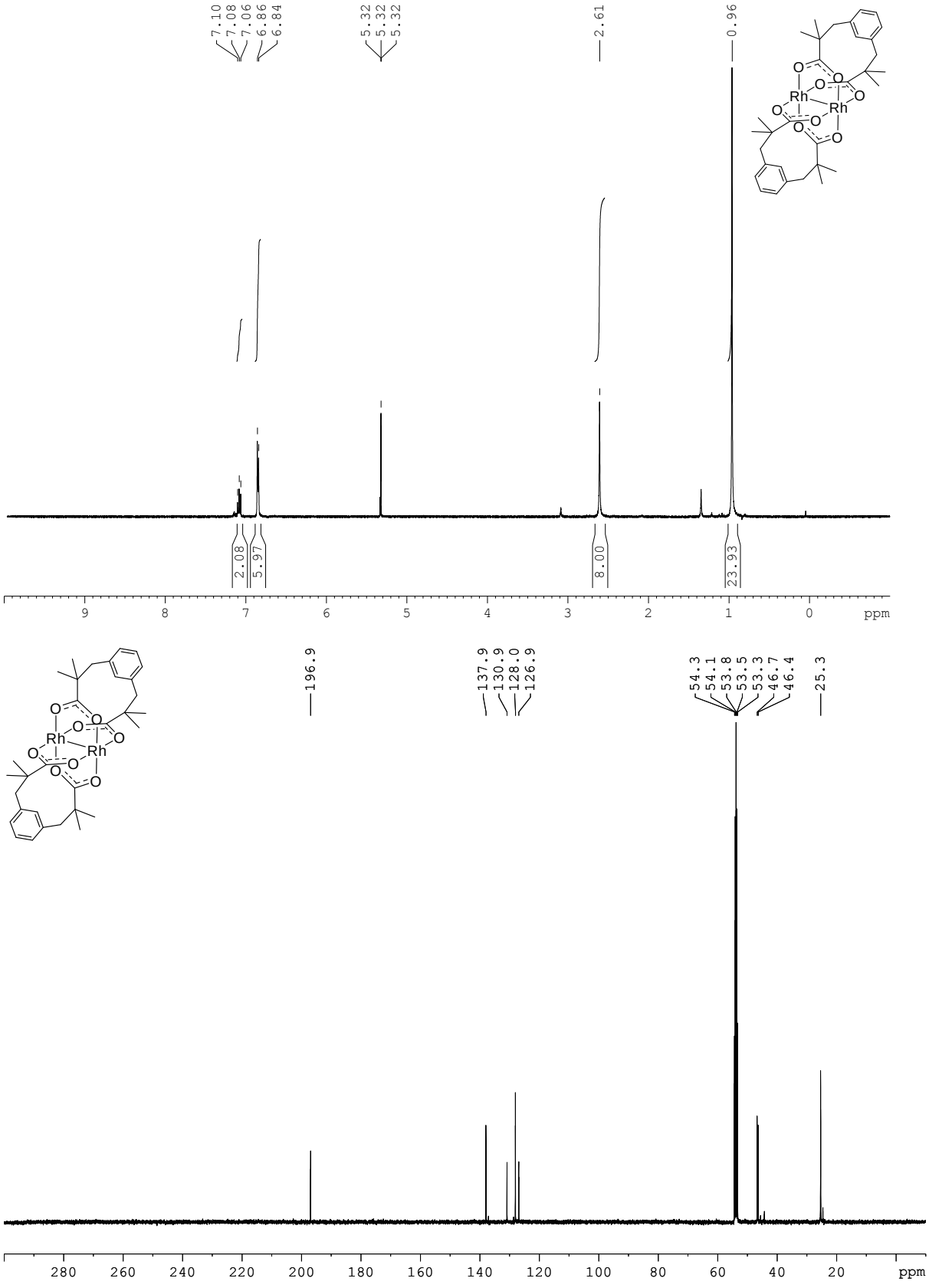
7.10
7.08
7.06
6.86
6.84
5.32
5.32
5.32
2.61
0.96
2.08
5.97
8.00
23.93
ppm
196.9
137.9
130.9
128.0
126.9
54.3
54.1
53.8
53.5
53.3
46.7
46.4
25.3
ppm

Prenyl diazoacetate (1)

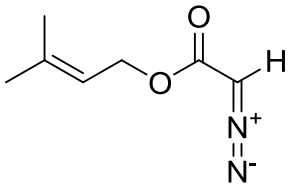

Prepared according to reference 11.[11]

^{1}H NMR (400 MHz, $CDCl_3$): δ = 5.34 (m, 1 H, $Me_2CC\underline{H}$), 4.74 (s, 1 H, $C(N_2)H$), 4.65 (d, J = 7.3 Hz, 2 H, CH_2), 1.76 (s, 3 H, $\underline{Me}_2CCH$), 1.72 (s, 3 H, $\underline{Me}_2CCH$) ppm.

$^{13}C\{^{1}H\}$ NMR (100 MHz, $CDCl_3$): δ = 167.9 ($O\underline{C}(O)C(N_2)H$), 139.3 ($Me_2\underline{C}CH$), 118.5 ($Me_2C\underline{C}H$), 61.7 (CH_2), 46.1 ($OC(O)\underline{C}(N_2)H$), 25.7 ($\underline{Me}_2CCH$), 18.0 ($\underline{Me}_2CCH$) ppm.

IR (oil): ν = 3098, 2964, 2936, 2924, 2103, 1684, 1444, 1386, 1356, 1234, 1172, 1047, 995, 915, 834, 779, 739, 551, 461, 432 cm^{-1}.

HRMS (ESI+): calcd. for $[C_7H_{10}N_2O_2Na]^+$: 177.063446; found 177.063290.

Prenyl diazoacetate (1)

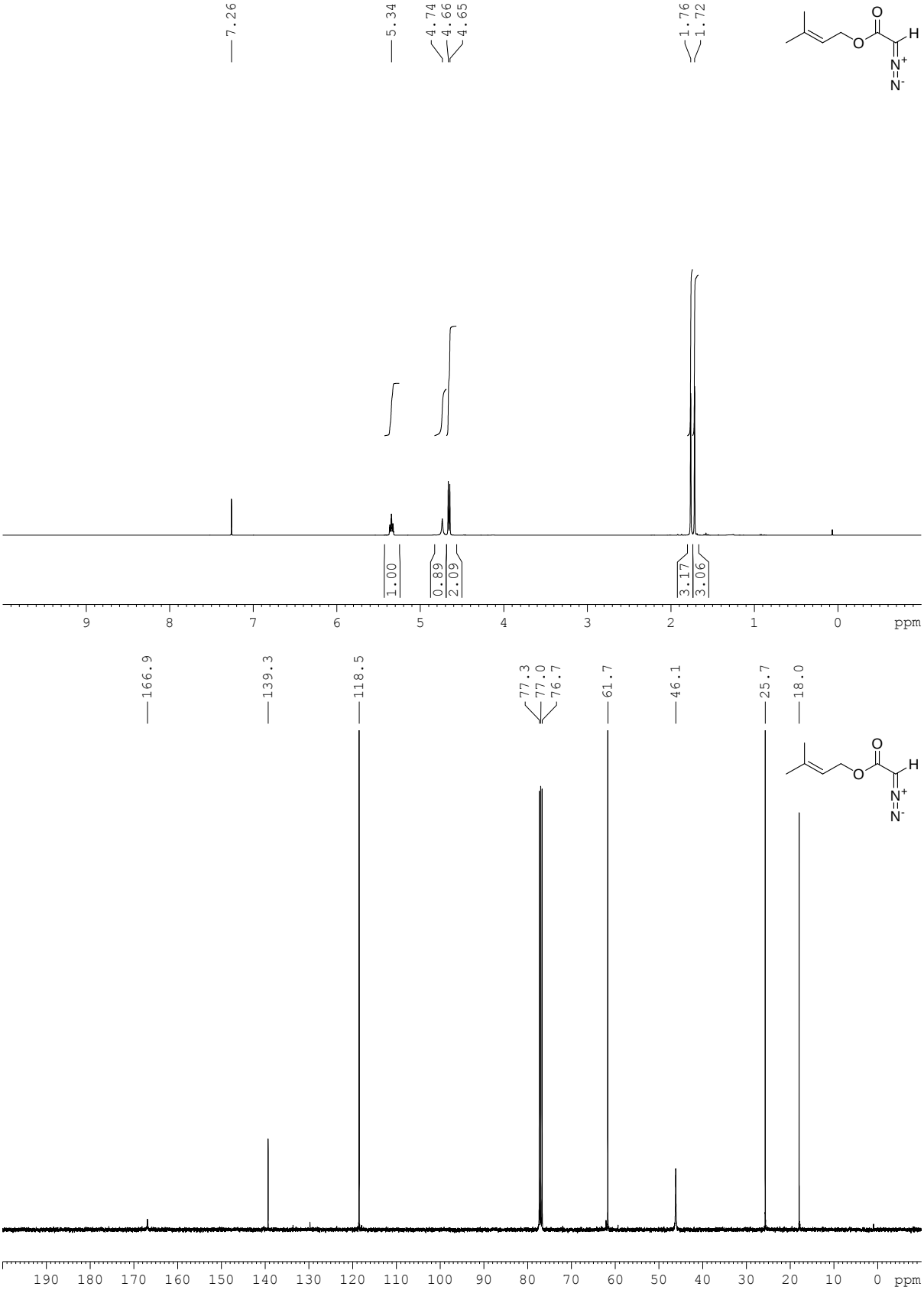

Prenyl 2,3-dichloropropanoate (3)

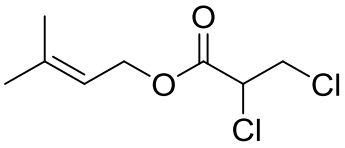

To a stirring solution of $BiRh(esp)_2$ (0.009 g, 0.01 mmol) in CH_2Cl_2 (5.0 mL) at 333 K was added a CH_2Cl_2 solution (5 mL) of prenyl diazoacetate (0.077 g, 0.50 mmol) by syringe pump over 2 h. After 3 h, the reaction was cooled and the product was isolated by column chromatography. Yield = 38 % yield.

^{1}H NMR (400 MHz, $CDCl_3$): δ 5.37 (m, 1 H, $Me_2CC\underline{H}$), 4.72 (d, J = 7.4 Hz, 2 H, CH_2), 4.42 (dd, J = 5.4, 8.3 Hz, 1 H, $ClCH_2C\underline{H}Cl$), 3.96 (dd, J = 8.4, 11.2 Hz, 1 H, $ClC\underline{H_2}CHCl$), 3.79 (dd, J = 5.4, 11.2 Hz, 1 H, $ClC\underline{H_2}CHCl$), 1.78 (s, 3 H, $\underline{Me}_2CCH$), 1.73 (s, 3 H, $\underline{Me}_2CCH$) ppm.

$^{13}C\{^1H\}$ NMR (100 MHz, $CDCl_3$): δ 167.0 (OCO), 140.8 ($Me_2\underline{C}CH$), 117.3 ($Me_2C\underline{C}H$), 63.4 (CH_2), 55.2 ($ClCH_2\underline{C}HCl$), 44.0 ($Cl\underline{C}H_2CHCl$), 25.7 ($\underline{Me}_2CCH$), 18.1 ($\underline{Me}_2CCH$) ppm.

IR (oil): ν = 2970, 2916, 1744, 1673, 1566, 1443, 1403, 1377, 1351, 1287, 1261, 1224, 1177, 1157, 1071, 1046, 982, 925, 823, 775, 735, 703, 634, 531, 449 cm^{-1}.

HRMS (ESI+): calcd. for $[C_8H_{12}O_2Cl_2Na_1]^+$: 233.010760; found 233.010655.

Rf = 0.30 (SiO_2, Hex : EtOAc, 30 : 1)

Prenyl 2,3-dichloropropanoate (3)

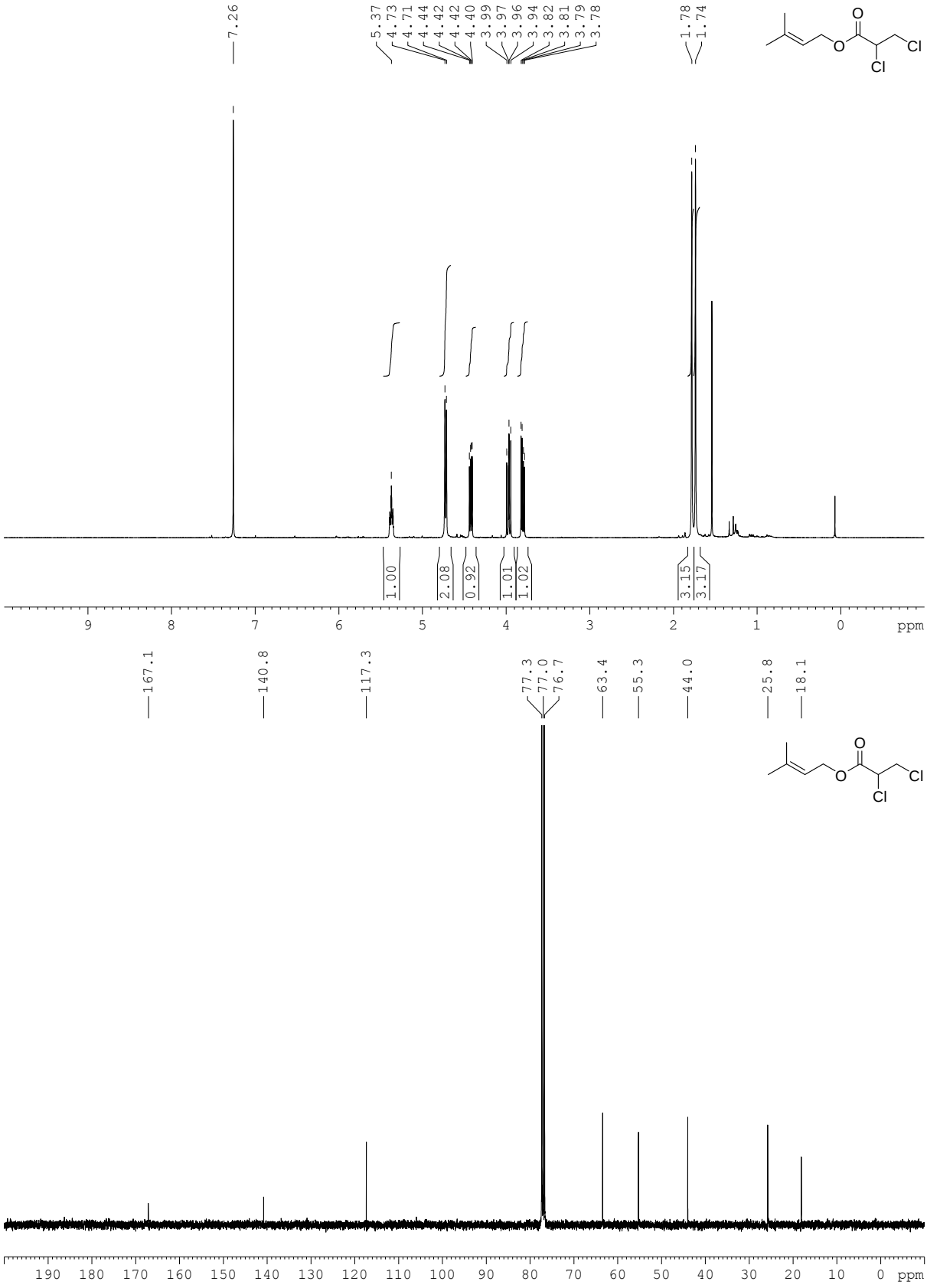

General Procedure A for Catalytic Solvent Activation with $BiRh(esp)_2$

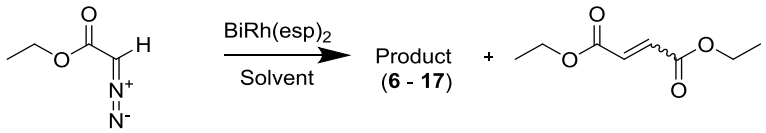

To a stirring solution of $BiRh(esp)_2$ (0.005 mmol) in solvent (5.0 mL) at 313 K was added EDA (0.775 mmol, 85 % solution in CH_2Cl_2) in one portion. After 2 h, the reaction was cooled and MesH (28.0 uL, 0.20 mmol) added as an internal standard for analysis. The crude reaction mixture was analysed by NMR and GCMS. Products were isolated by column chromatography.

Ethyl 2,3-dichloropropanoate (6)

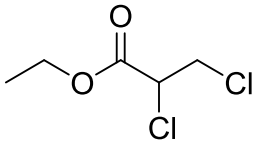

Isolated as a yellow oil in 51 % yield by General Procedure A (DCM as solvent; modified with: EDA added by syringe pump over 2 h, 0.02 mmol $BiRh(esp)_2$, 333 K, 3 h).

Spectroscopic data matched those reported in the literature.[12]

Ethyl 2-phenylcyclopropane-1-carboxylate (7)

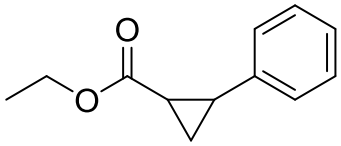

Isolated in 20 % yield by General Procedure A (modified to match the conditions reported in reference 13 with: DCM as solvent (40 mL), 5 eq styrene, EDA added by syringe pump over 2 h, 0.02 mmol $BiRh(esp)_2$, 3 h).[13]

Spectroscopic data matched those reported in the literature.[14]

Ethyl n-methylcyclohepta-2,4,6-triene-1-carboxylate (8)

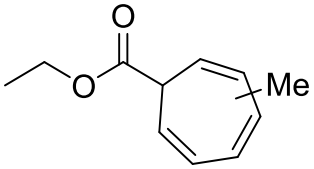

Isolated in 75 % yield by General Procedure A (toluene as solvent).

Spectroscopic data matched those reported in the literature.[15]

Ethyl cyclohexylacetate (9)

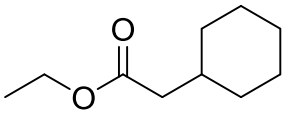

Isolated as a colourless oil in 53 % yield by General Procedure A (cyclohexane as solvent; modified with: 323 K, 3 h).

Spectroscopic data matched those reported in the SDBS Structural Database for Organic Chemicals (SDBS No. 18306)

5-ethoxy-2-methyloxazole (10)

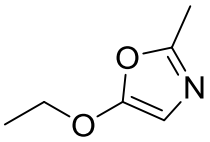

NMR yield of 89 % recorded by General Procedure A (MeCN as solvent; modified with: 363 K, 16 h).

Spectroscopic data matched those reported in the literature.[16]

Ethyl 2,3,3-trichloropropanoate (11)

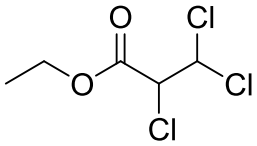

Isolated as a colourless oil in 53 % yield by General Procedure A ($CHCl_3$ as solvent).

Spectroscopic data matched those reported in the literature.[12]

Ethyl chloroacetate (12)

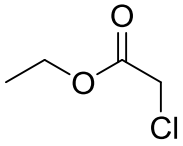

Isolated as a yellow oil in 46 % yield by General Procedure A (^{t}BuCl as solvent).

Spectroscopic data matched those reported in the literature.[17]

Ethyl trans-2,3-dichlorocyclopropane-1-carboxylate (13)

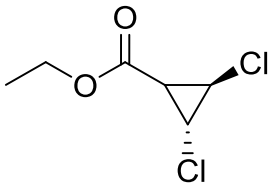

Isolated as a colourless oil in 63 % yield by General Procedure A (trans-1,2-dichloroethylene as solvent (20 mL); modified with: EDA added by syringe pump over 16 h, 318 K, 18 h).

^{1}H NMR (400 MHz, $CDCl_3$): δ = 4.23 (q, J = 7.2 Hz, 2 H, CH_2), 3.76 (dd J = 3.7, 4.8 Hz, 1 H, CHCl), 3.55 (dd, J = 3.7, 9.0 Hz, 1 H, CHCl), 2.42 (dd, J = 4.8, 9.0 Hz, 1 H, CH), 1.30 (t, 7.2 Hz, 3 H, CH_3) ppm.

^{13}C{^{1}H} NMR (100 MHz, $CDCl_3$): δ = 165.1 (CO), 60.8 (CH_2), 37.7 (CHCl), 36.2 (CHCl), 30.6 (CH), 13.2 (CH_3) ppm.

IR (oil): ν = 3062, 2983, 1732, 1608, 1466, 1446, 1400, 1384, 1306, 1259, 1224, 1200, 1162, 1097, 1056, 1035, 1011, 967, 893, 860, 837, 805, 785, 710, 689, 646 cm^{-1}.

HRMS (ESI+): calcd. for $[C_6H_8Cl_2O_2Na_1]^+$: 204.979355; found 204.979520.

Rf = 0.55 (SiO_2, Pent : Et_2O, 5 : 1).

Ethyl trans-2,3-dichlorocyclopropane-1-carboxylate (13)

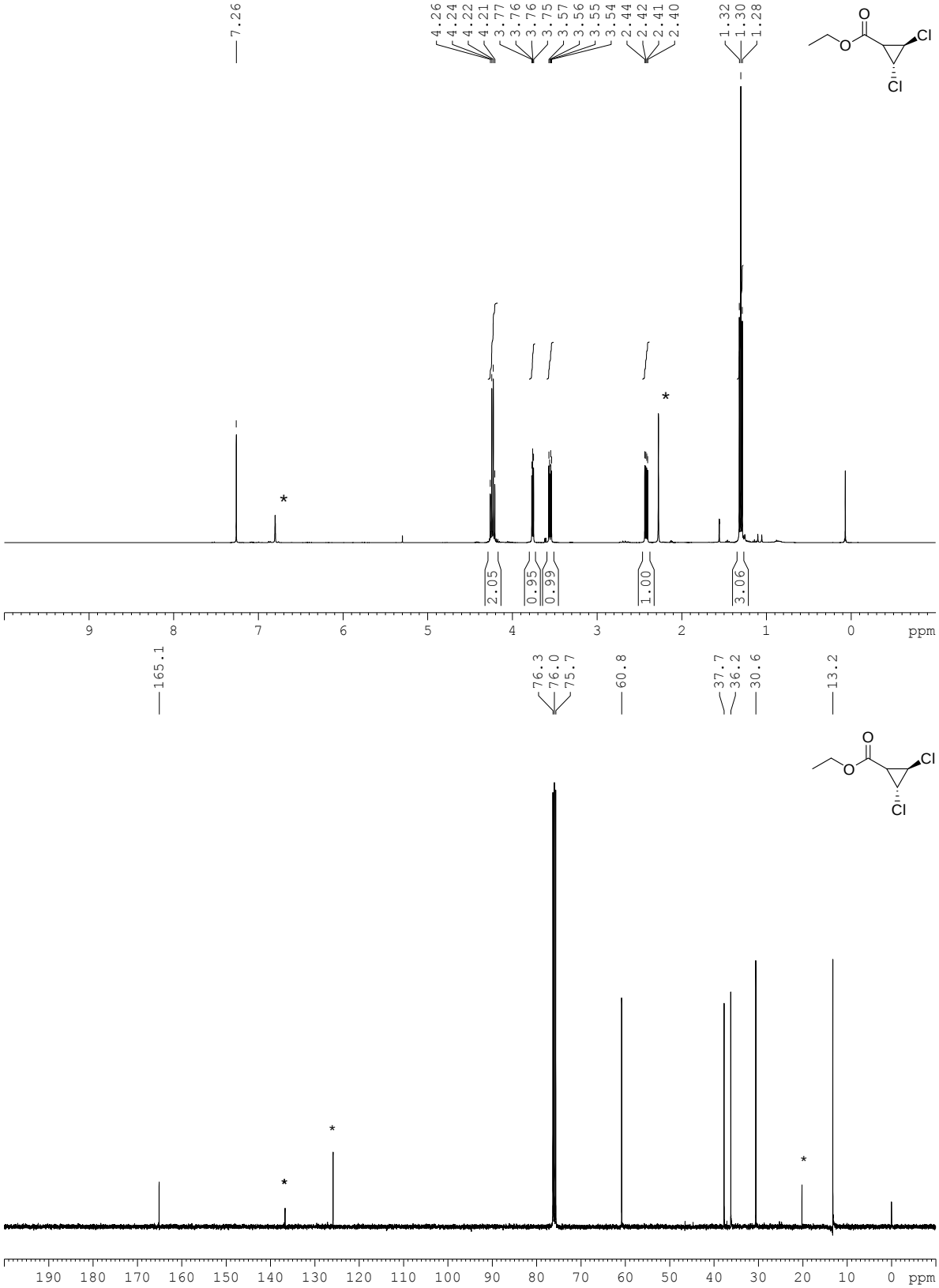

* Denotes mesitylene

Ethyl *cis*-2,2,3-trichlorocyclopropane-1-carboxylate (*cis*-14)

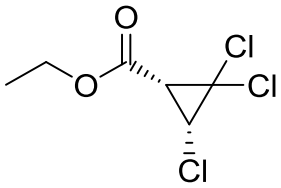

Isolated as a colourless oil in 61 % yield by General Procedure A (trichloroethylene as solvent (20 mL); modified with: EDA added by syringe pump over 16 h, 333 K, 18 h).

^{1}H NMR (400 MHz, $CDCl_3$): δ = 4.25 (q, J = 7.2 Hz, 2 H, CH_2), 3.84 (d, J = 9.6 Hz, 1 H, CHCl), 2.76 (d, J = 9.6 Hz, 1 H, CH), 1.31 (t, 7.2 Hz, 3 H, CH_3) ppm.

^{13}C{^{1}H} NMR (100 MHz, $CDCl_3$): δ = 162.7 (CO), 61.9 (CH_2), 59.4 (CCl_2), 43.1 (CHCl), 35.7 (CH), 14.0 (CH_3) ppm.

IR (oil): ν = 3054, 2984, 1744, 1466, 1446, 1395, 1374, 1352, 1296, 1217, 1158, 1096, 1028, 981, 919, 862, 833, 676, 532, cm^{-1}.

HRMS (ESI+): calcd. for $[C_6H_7O_2Cl_3Na_1]^+$: 238.940383 ; found 238.940520.

Rf = 0.3 (SiO_2, Pent : Et_2O, 10 : 1).

Ethyl *cis*-2,2,3-trichlorocyclopropane-1-carboxylate (*cis*-14)

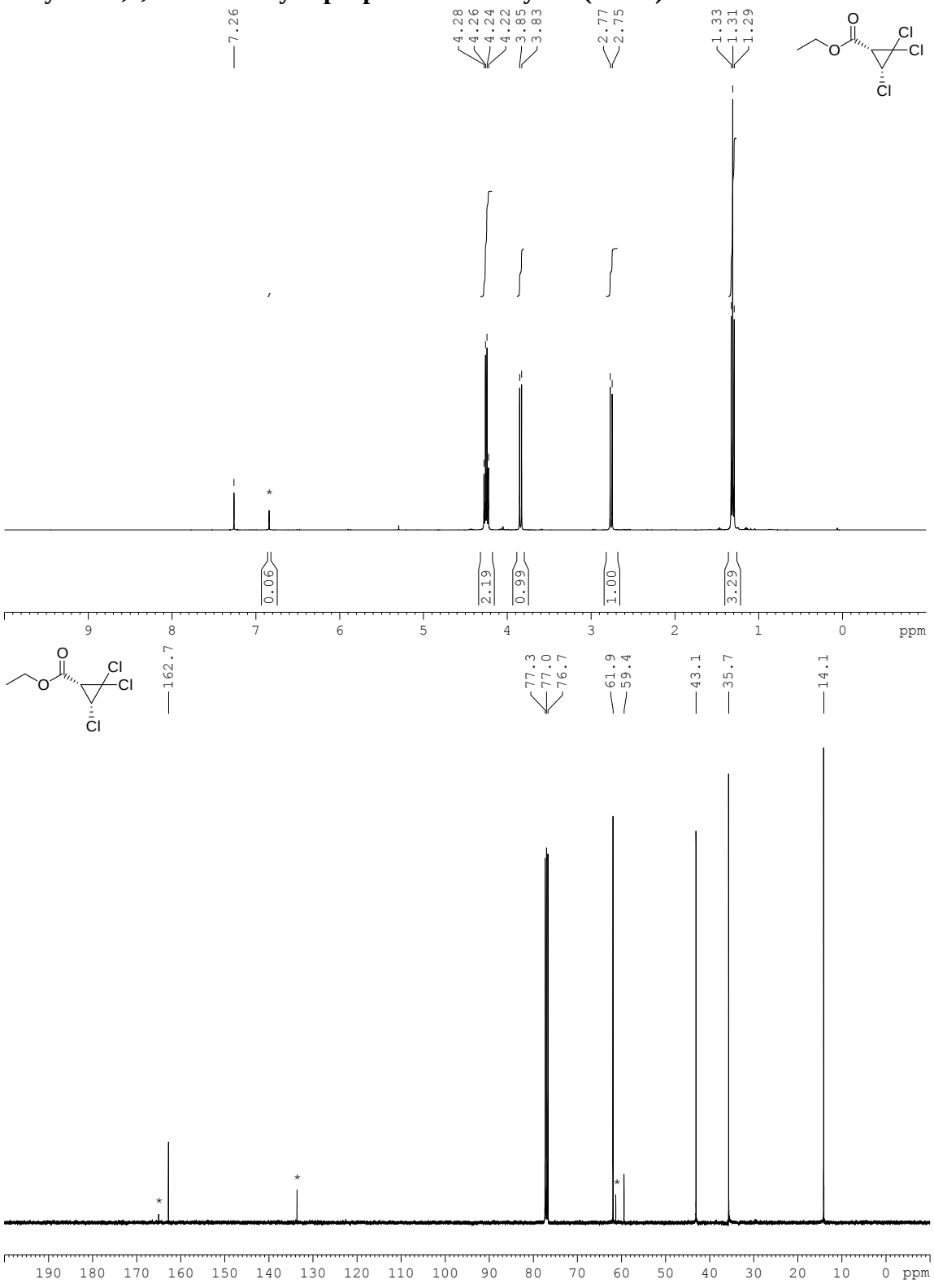

* Denotes a product of HCl elimination, formed during chromatography. These resonances are not present in crude reaction NMR analyses.

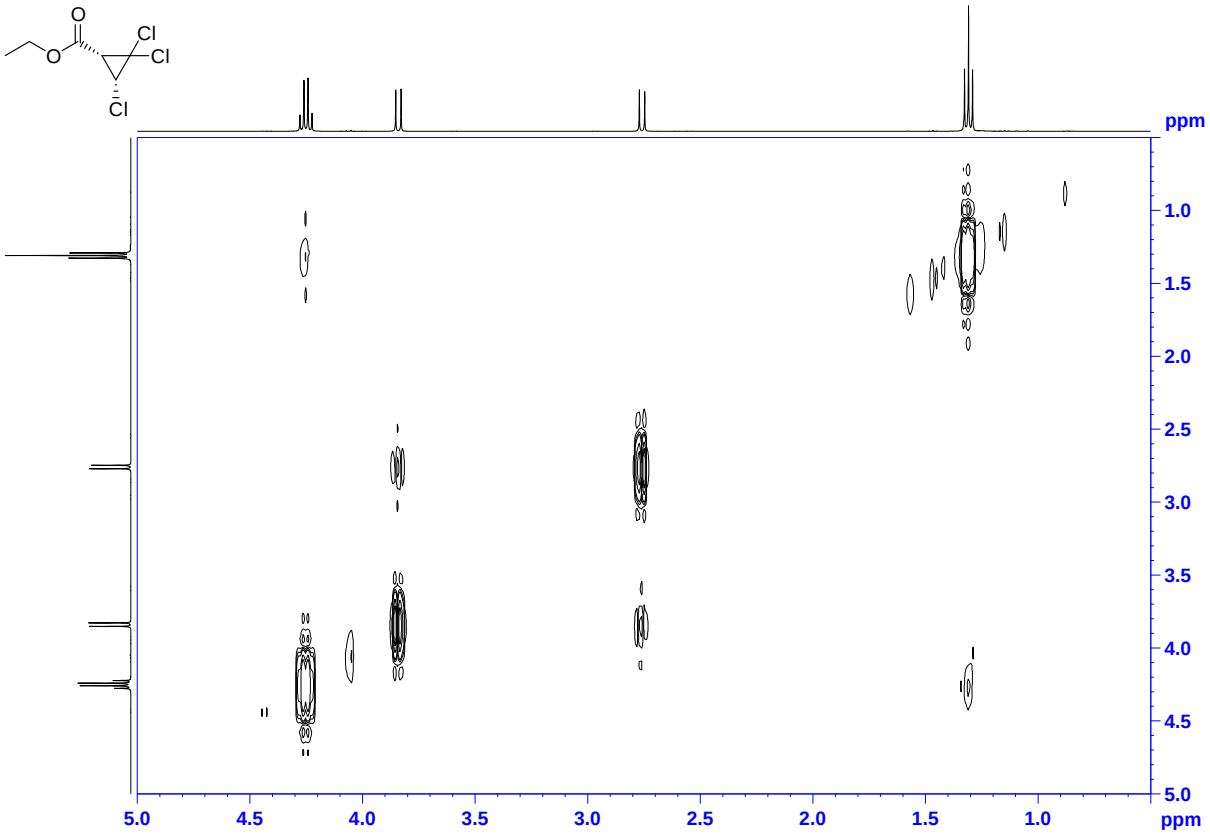

^{1}H-^{1}H NOESY NMR spectrum (400 MHz, $CDCl_3$).

Ethyl *trans*-2,2,3-trichlorocyclopropane-1-carboxylate (*trans*-14)

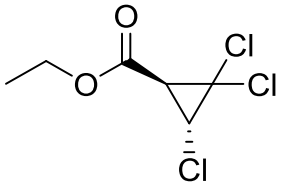

Isolated as a colourless oil in 11 % yield by General Procedure A (trichloroethylene as solvent (20 mL); modified with: EDA added by syringe pump over 16 h, 333 K, 18 h).

^{1}H NMR (400 MHz, $CDCl_3$): δ = 4.26 (q, J = 7.1 Hz, 2 H, CH_2), 4.00 (d, J = 6.4 Hz, 1 H, CHCl), 2.60 (d, J = 6.4 Hz, 1 H, CH), 1.32 (t, 7.1 Hz, 3 H, CH_3) ppm.

^{13}C{^{1}H} NMR (100 MHz, $CDCl_3$): δ = 162.7 (CO), 61.9 (CH_2), 59.4 (CCl_2), 43.1 (CHCl), 35.7 (CH), 14.1 (CH_3) ppm.

IR (oil): ν = 3051, 2983, 2929, 2856, 1740, 1610, 1466, 1446, 1378, 1274, 1214, 1175, 1027, 967, 914, 852, 743, 530 cm^{-1}.

HRMS (ESI+): calcd. for $[C_6H_7O_2Cl_3Na_1]^+$: 238.940383 ; found 238.940430.

Rf = 0.5 (SiO_2, Pent : Et_2O, 10 : 1).

Ethyl *trans*-2,2,3-trichlorocyclopropane-1-carboxylate (*trans*-14)

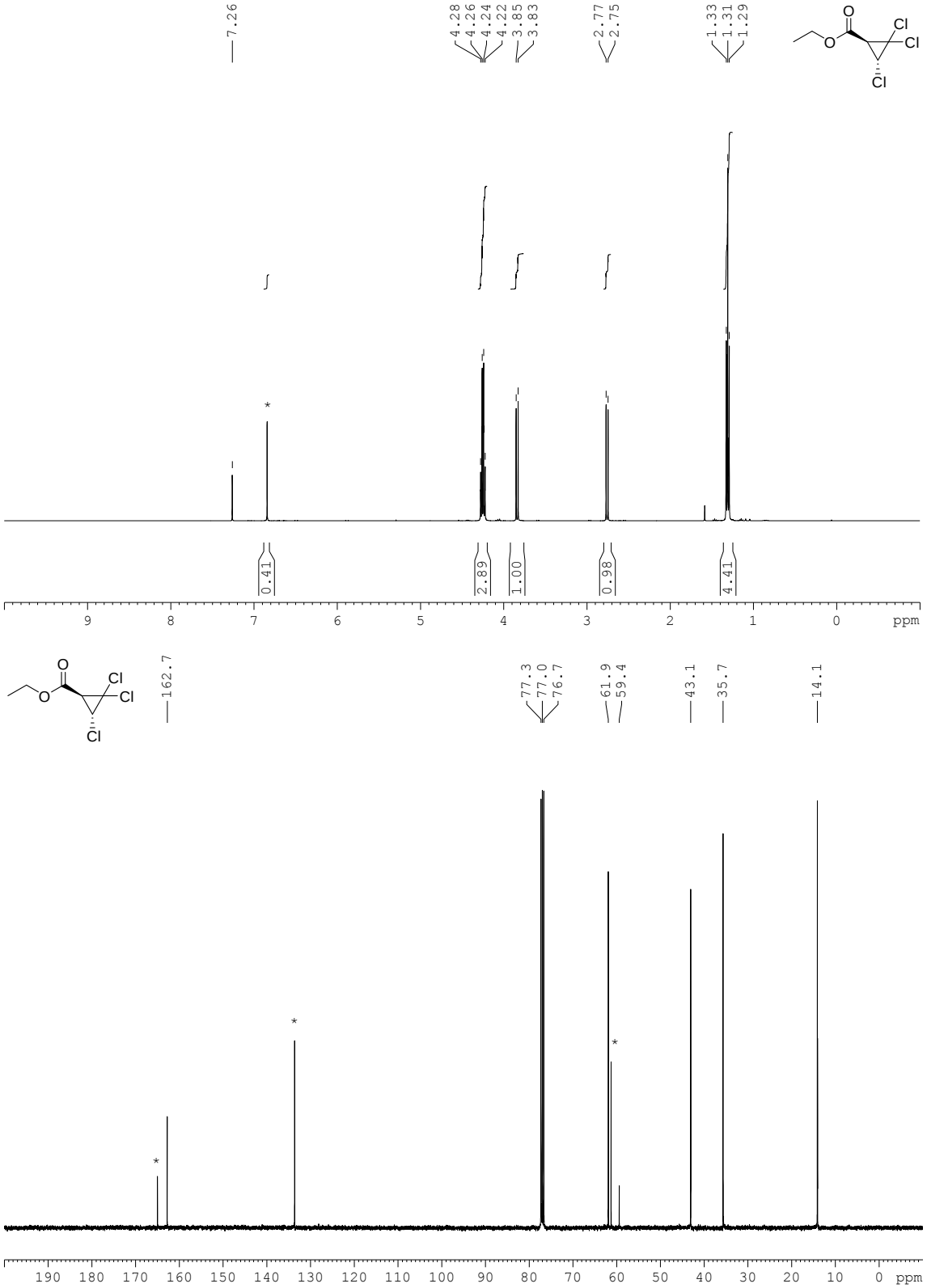

* Denotes a product of HCl elimination, formed during chromatography. These resonances are not present in crude reaction NMR analyses.

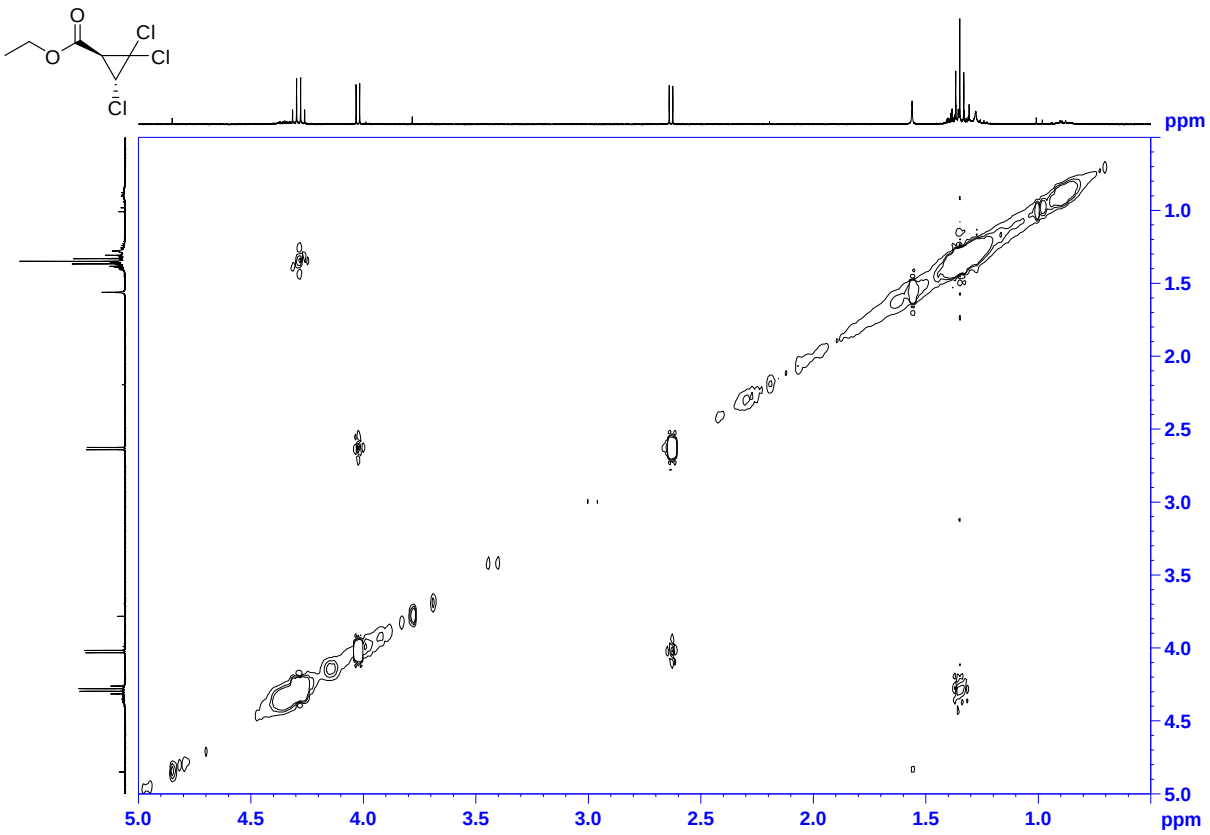

^{1}H-^{1}H NOESY NMR spectrum (400 MHz, $CDCl_3$).

Cyclopropanation of Trichloroethylene with EDA:

GC of the Reaction Catalyzed by [BiRh(esp)$_2$]

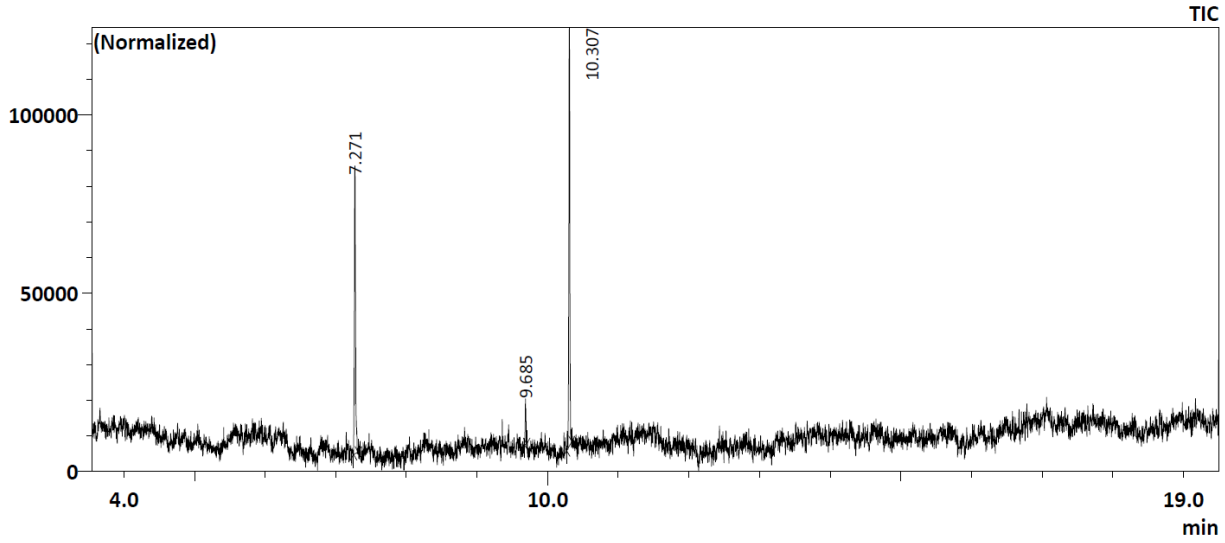

Peak	Time	%
1 (= mesitylene, internal standard)	7.27	42.2
2 (*trans*-**14**)	9.69	4.0
3 (*cis*-**14**)	10.31	53.9

GC of the Reaction under UV Irradiation (UV lamp emitting 100 -380 nm radiation, 1hr, internal temperature 70°C) without any Metal Catalyst

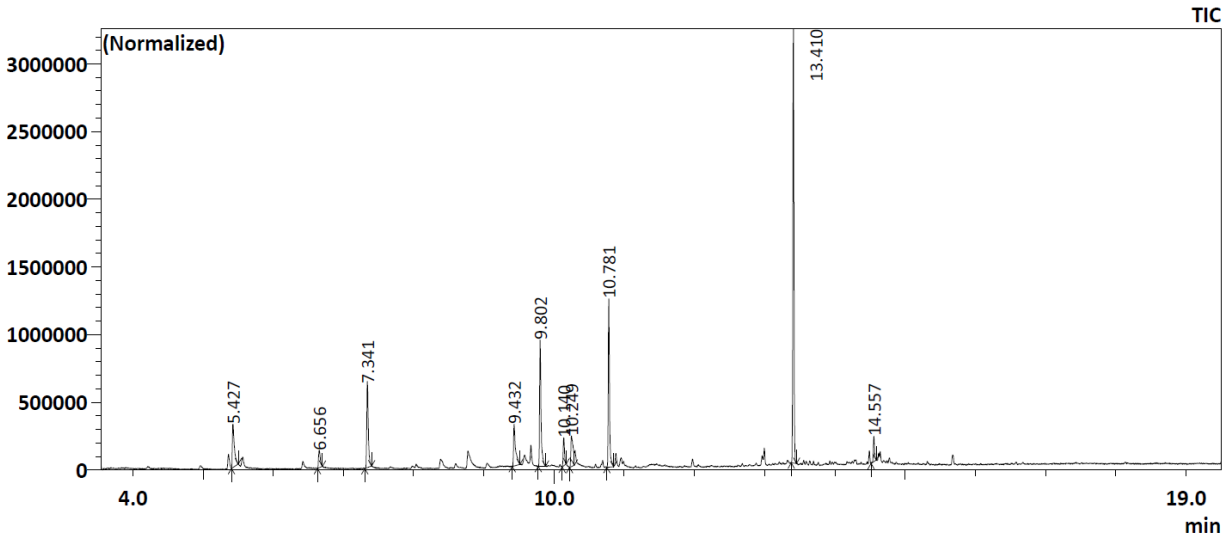

GC/MS and comparison with authentic material show that the peaks at 9.80 and 10.25 min correspond to *trans*- and *cis*-**14**

Ethyl 2-(cyclohex-2-en-1-yl)acetate (15)

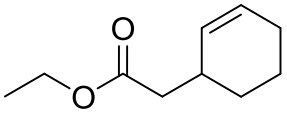

Isolated as a colourless oil in 28 % yield by General Procedure A (cyclohexene as solvent; modified with: 0.005 mmol $BiRh(TPA)_4$, 323 K, 4 h).

Spectroscopic data matched those reported in the literature.[18]

Ethyl exo-bicyclo[4.1.0]heptane-7-carboxylate (16)

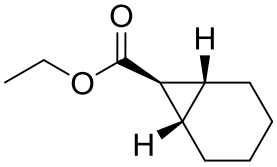

Isolated as a colourless oil in 74 % yield by General Procedure A (cyclohexene as solvent; modified with: 0.005 mmol $BiRh(Piv)_4$, 323 K, 4 h).

Spectroscopic data matched those reported in the literature.[18]

Ethyl exo-bicyclo[4.1.0]heptane-7-carboxylate (17)

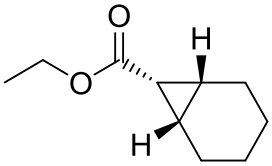

Isolated as a colourless oil in 29 % yield by General Procedure A (cyclohexene as solvent; modified with: 0.005 mmol $BiRh(TPA)_4$, 323 K, 4 h).

Spectroscopic data matched those reported in the literature.[19]

(*p*-MeOPh)$_2$CN$_2$ (18)

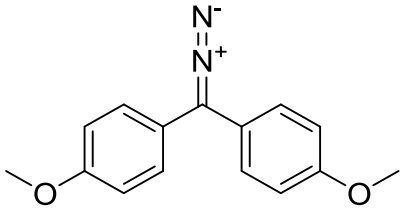

Prepared according to reference 20.[20]

^{1}H NMR (400 MHz, C_6D_6): δ 7.07 (d, J = 8.5 Hz, 4 H, *o*-ArH), 6.75 (d, J = 8.5 Hz, 4 H, *m*-ArH), 3.29 (s, 6 H, OMe) ppm.

^{13}C{^{1}H} NMR (100 MHz, C_6D_6): δ 158.4 (Ar), 126.9 (Ar), 121.9 (Ar), 115.2 (Ar), 61.0 (CN_2), 54.9 (MeO) ppm.

(*p*-MeOPh)$_2$CN$_2$ (18)

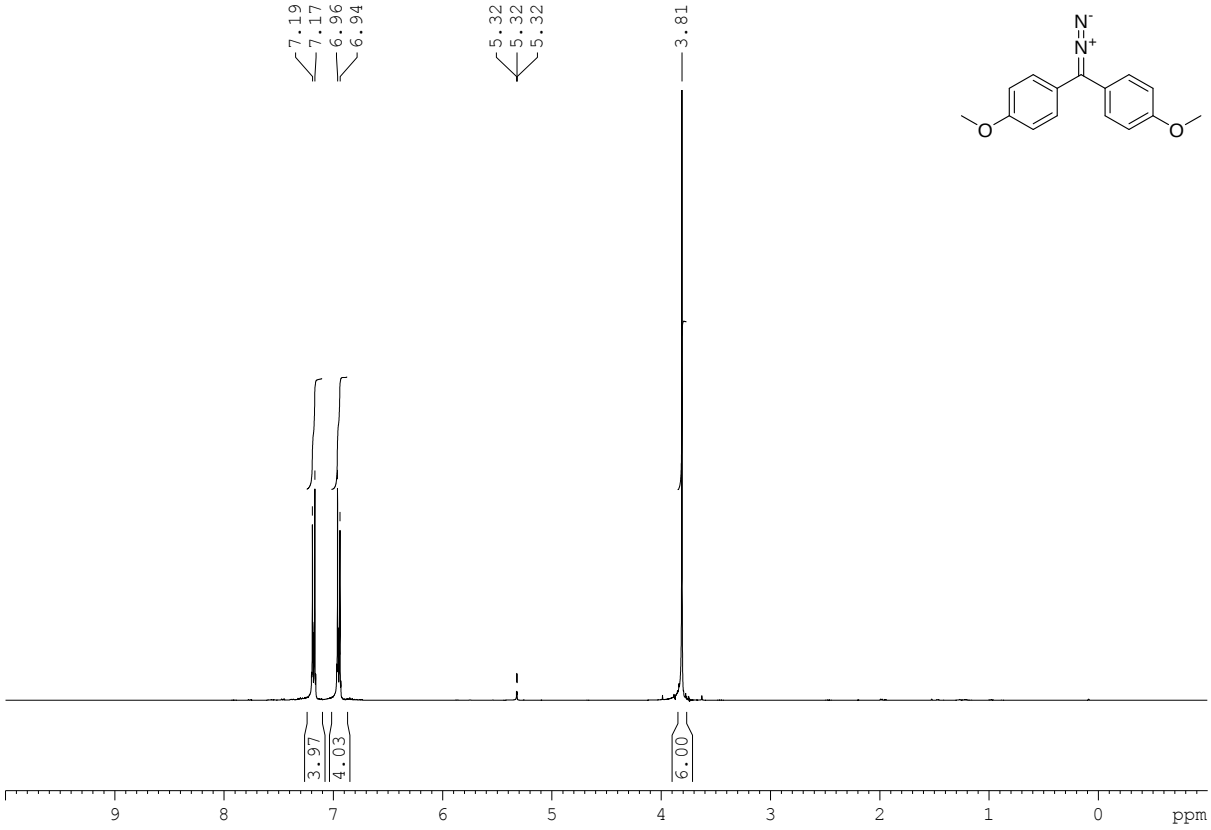

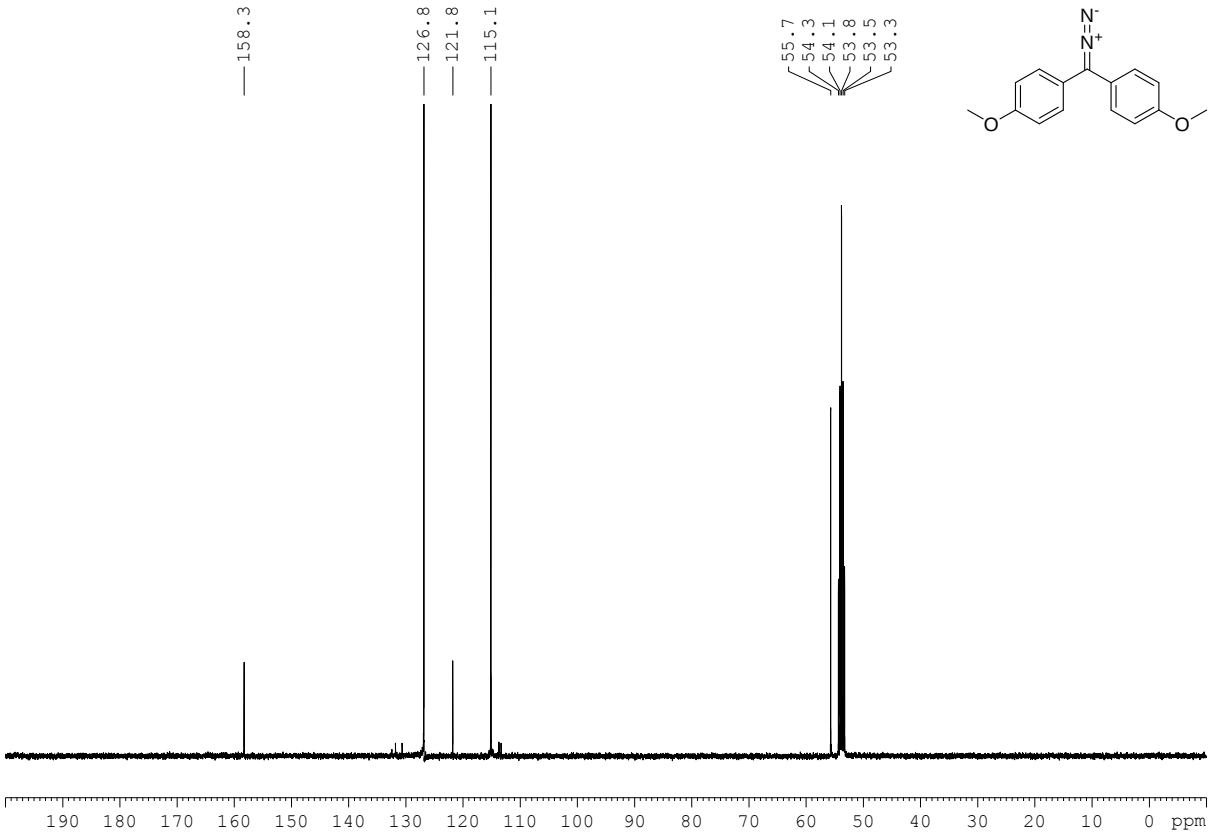

General Procedure (B) for Carbene Formation for Spectroscopic Analysis

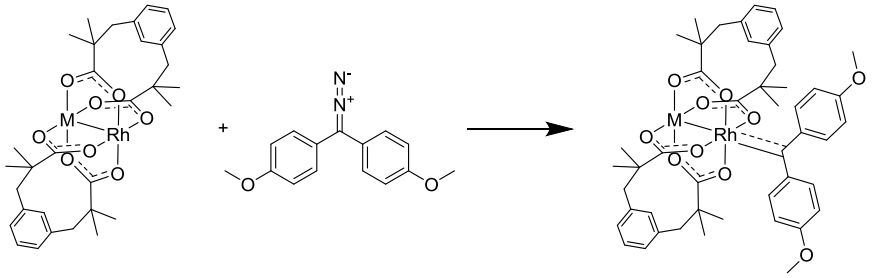

Under rigorously anaerobic conditions: 1 mL of a stock solution of complex (0.005 mmol) in CH_2Cl_2 (5.0 mL) at 195 K was added 0.5 mL of a stock solution of (*p*-MeOPh)$_2$CN$_2$ (0.01 mmol) in CH_2Cl_2 (5.0 mL) dropwise over 2 min. The crude, dark green reaction mixture was analysed by various spectroscopic techniques. Concentrations were adjusted as necessary by dilution with CH_2Cl_2.

$Rh_2(esp)_2C(p\text{-}MeOPh)_2$ (19)

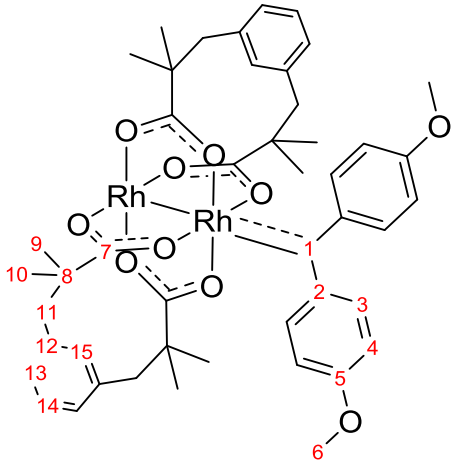

To a solution of $Rh_2(esp)_2$ (0.017 g, 0.022 mmol) in CD_2Cl_2 (2.0 mL) at 195 K was slowly added a solution of $(p\text{-}MeOPh)_2CN_2$ (0.006 g, 0.024 mmol) in CD_2Cl_2 (0.5 mL), resulting in the immediate formation of a dark green solution. This solution was transferred to a pre-cooled NMR tube.

^1H NMR (400 MHz, CD_2Cl_2, 263 K): δ = 7.81 (d, 8.8 Hz, 4 H, H_3), 7.12 (t, 7.4 Hz, 2 H, H_{14}), 6.85-6.78 (overlapping, 8 H, H_4 and H_{13}), 6.62 (s, 2 H, H_{15}), 3.93 (s, 6 H, H_6), 2.60 (d, 12.4 Hz, 4 H, H_{11}), 2.27 (d, 12.4 Hz, 4 H, H_{11}), 0.85 (s, 12 H, H_9), 0.76 (s, 12 H, H_{10}) ppm.

$^{13}C\{^1H\}$ NMR (100 MHz, CD_2Cl_2, 263 K): δ = 262.2 (br. s, C_1), 194.7 (s, C_7), 164.9 (s, C_5), 147.1 (s, C_2), 138.1 (s, C_{12}), 136.9 (s, C_3), 131.4 (s, C_{15}), 127.9 (s, C_{13}), 126.5 (s, C_{14}), 113.7 (s, C_4), 56.1 (s, C_6), 46.9 (s, C_{11}), 46.2 (s, C_8), 26.1 (s, C_{10}), 24.5 (s, C_9) ppm.

$Rh_2(esp)_2C(p\text{-}MeOPh)_2$ (19)

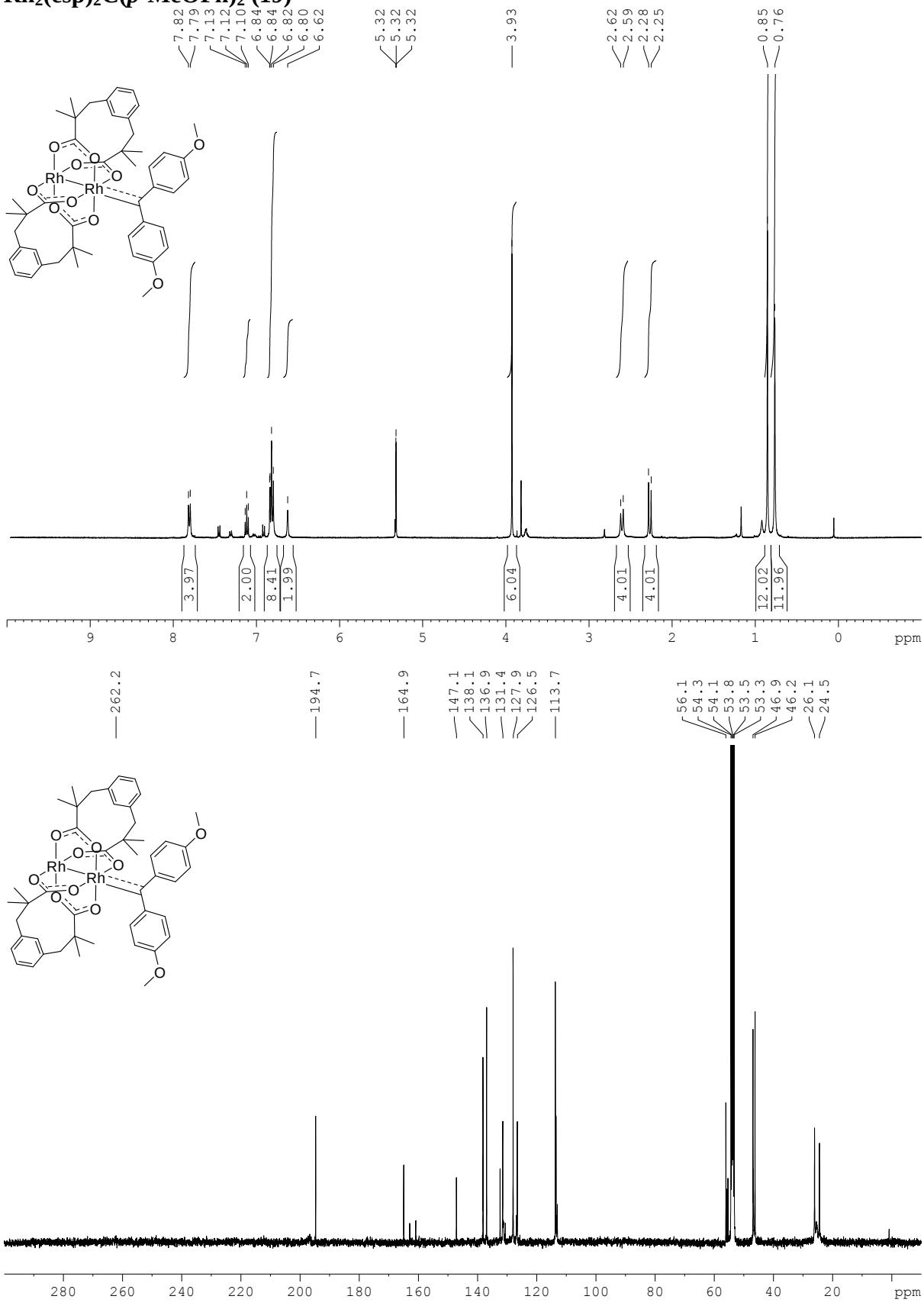

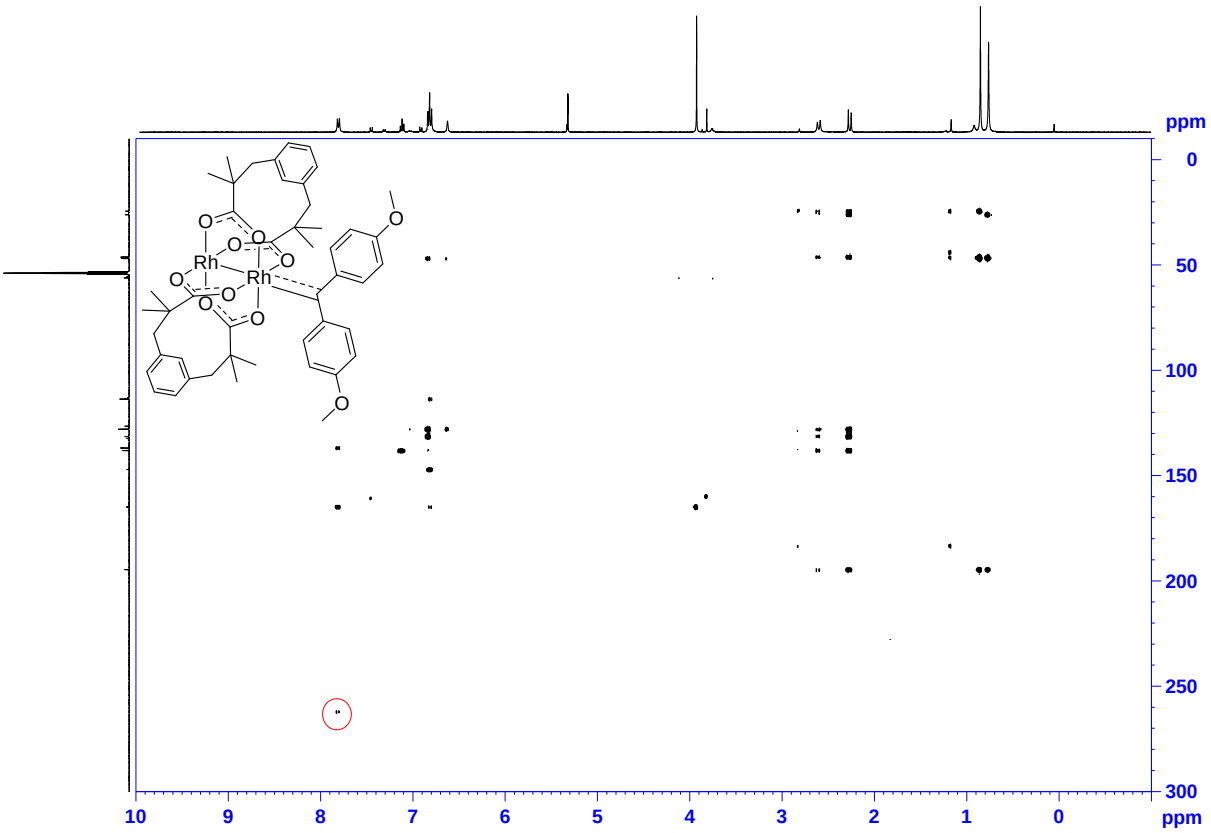

^{1}H-^{13}C HMBC NMR spectrum (400 MHz, CD_2Cl_2, 263 K) of the reaction mixture. Highlighted signal represents the $H_3 - C_1$ ^{3}J correlation.

BiRh(esp)$_2$C(*p*-MeOPh)$_2$ (20)

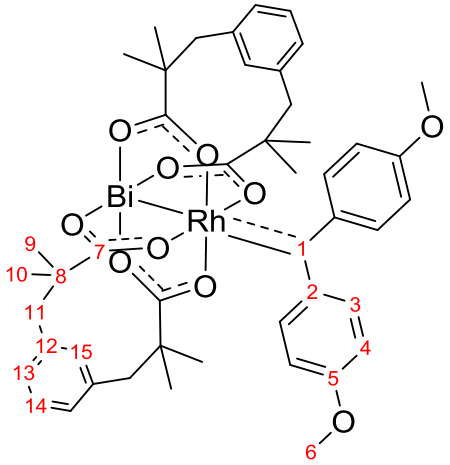

To a solution of BiRh(esp)$_2$ (0.004 g, 0.005 mmol) in CD_2Cl_2 (2.0 mL) at 195 K was slowly added a solution of (*p*-MeOPh)$_2$CN$_2$ (0.001 g, 0.005 mmol) in CD_2Cl_2 (0.5 mL), resulting in brown homogeneous solution which turned green over the course of 30 min. This solution was transferred to a pre-cooled NMR tube.

The sample was mostly comprised of azine (**21**) and BiRh(esp)$_2$. Selected resonances for complex **20** could be identified by comparison with reference samples of **21** and BiRh(esp)$_2$, and by observing its decomposition:

^{1}H NMR (400 MHz, CD_2Cl_2, 225 K): δ = 6.65 (shoulder, H_{15}), 3.91 (s, 6 H, H_6), 3.08 (d, 12.1 Hz, 4 H, H_{11}), 2.20 (d, 12.1 Hz, 4 H, H_{11}), 1.00 (s, overlapping, H_9), 0.60 (s, 12 H, H_{10}) ppm.

BiRh(esp)$_2$C(*p*-MeOPh)$_2$ (20)

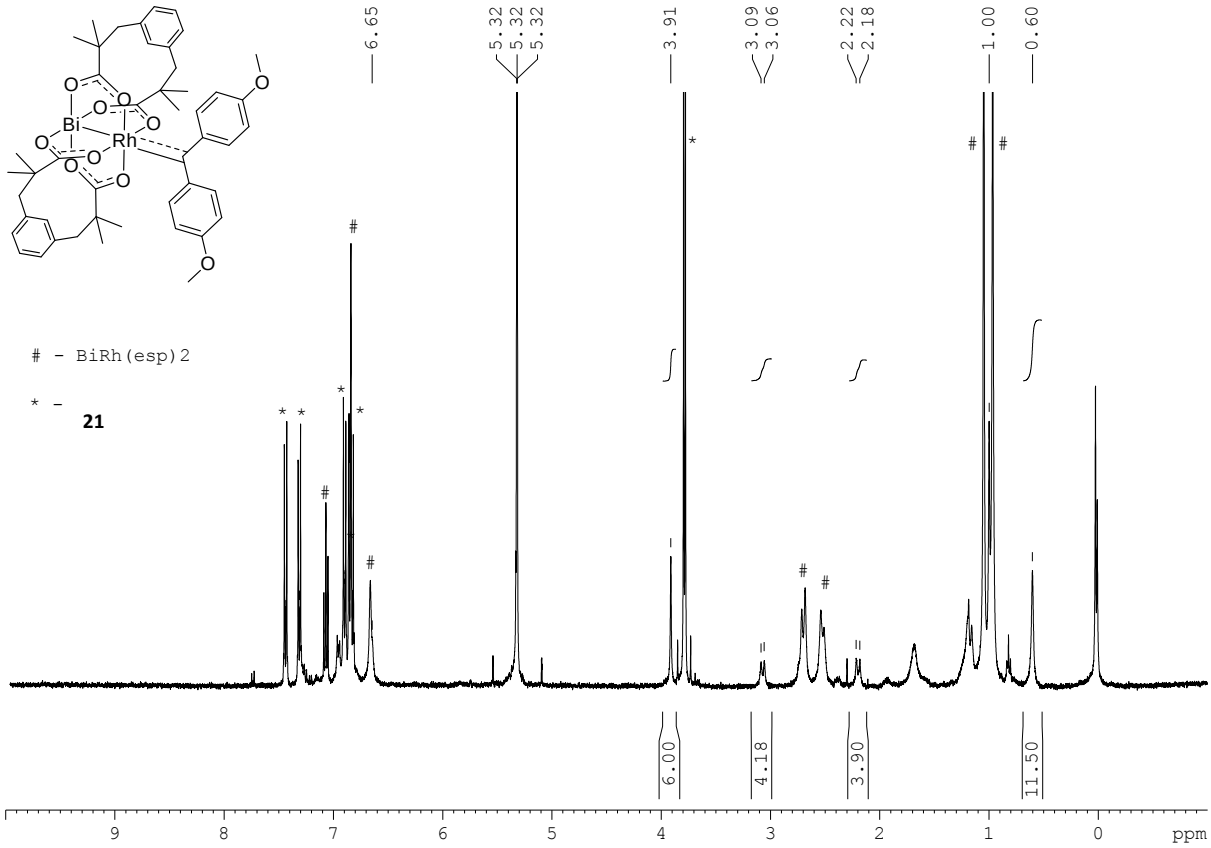

^{1}H NMR spectrum (400 MHz, CD_2Cl_2, 225 K) of the reaction mixture at 225 K. # denotes resonances attributed to BiRh(esp)$_2$, as confirmed by comparison to a clean sample. * denotes resonances attributed to azine **21**, as confirmed by comparison to a clean sample.

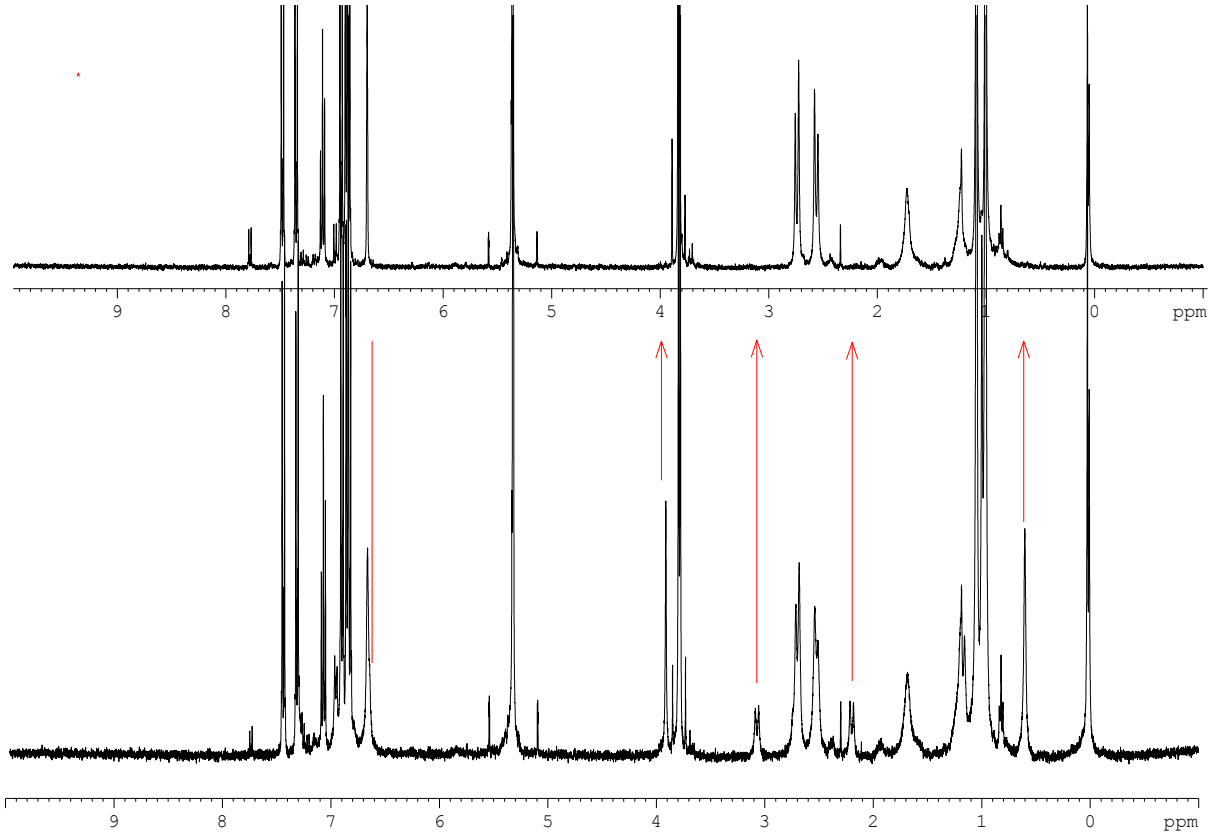

Below: ^{1}H NMR spectrum (400 MHz, CD_2Cl_2, 225 K) of the reaction mixture at 225 K; Above: ^{1}H NMR spectrum (400 MHz, CD_2Cl_2, 225 K) of the reaction mixture after being warmed to room temperature and then returned to 225 K. Red arrows highlight the disappearance of signals attributed to complex **20**.

(*p*-MeOPh)$_2$CNNC(*p*-MeOPh)$_2$ (21)

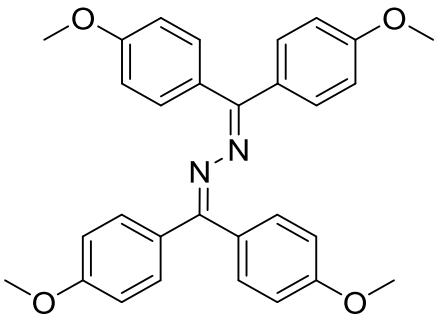

To a stirring purple pentane (5 mL) solution of (*p*-MeOPh)$_2$CN$_2$ (0.050 g, 0.197 mmol) was added Rh$_2$(esp)$_2$ (0.001 g, 0.001 mmol) resulting in the formation of a red solution which precipitated a white solid over the course of 30 min. After 1 h, volatiles were removed and the brown powder was re-precipitated from CH_2Cl_2 and pentane, washed with pentane and dried in vacuo to yield a cream powder. Yield = 0.034 g (72 %).

^{1}H NMR (400 MHz, $CDCl_3$): δ = 7.48 (d, 8.8 Hz, 4 H, *o*-ArH), 7.33 (d, 8.8 Hz, 4 H, *o*-ArH), 6.91 (d, 8.8 Hz, 4 H, *m*-ArH), 6.82 (d, 8.8 Hz, 4 H, *m*-ArH), 3.84 (s, 6 H, OMe), 3.81 (s, 6 H, OMe) ppm.

^{13}C{^{1}H} NMR (100 MHz, $CDCl_3$): δ = 160.7 (*p*-Ar), 159.6 (*p*-Ar), 159.2 (CN_2), 131.6 (*i*-Ar), 131.4 (*o*-Ar), 130.3 (*o*-Ar), 128.0 (*i*-Ar), 113.3 (*m*-Ar), 113.0 (*m*-Ar), 55.3 (OMe), 55.2 (OMe) ppm.

IR (solid): *v* = 3035, 3009, 2968, 2838, 1608, 1580, 1505, 1325, 1299, 1244, 1167, 1156, 1117, 1027, 843, 832, 805, 742, 611, 567 cm^{-1}.

(*p*-MeOPh)$_2$CNNC(*p*-MeOPh)$_2$ (21)

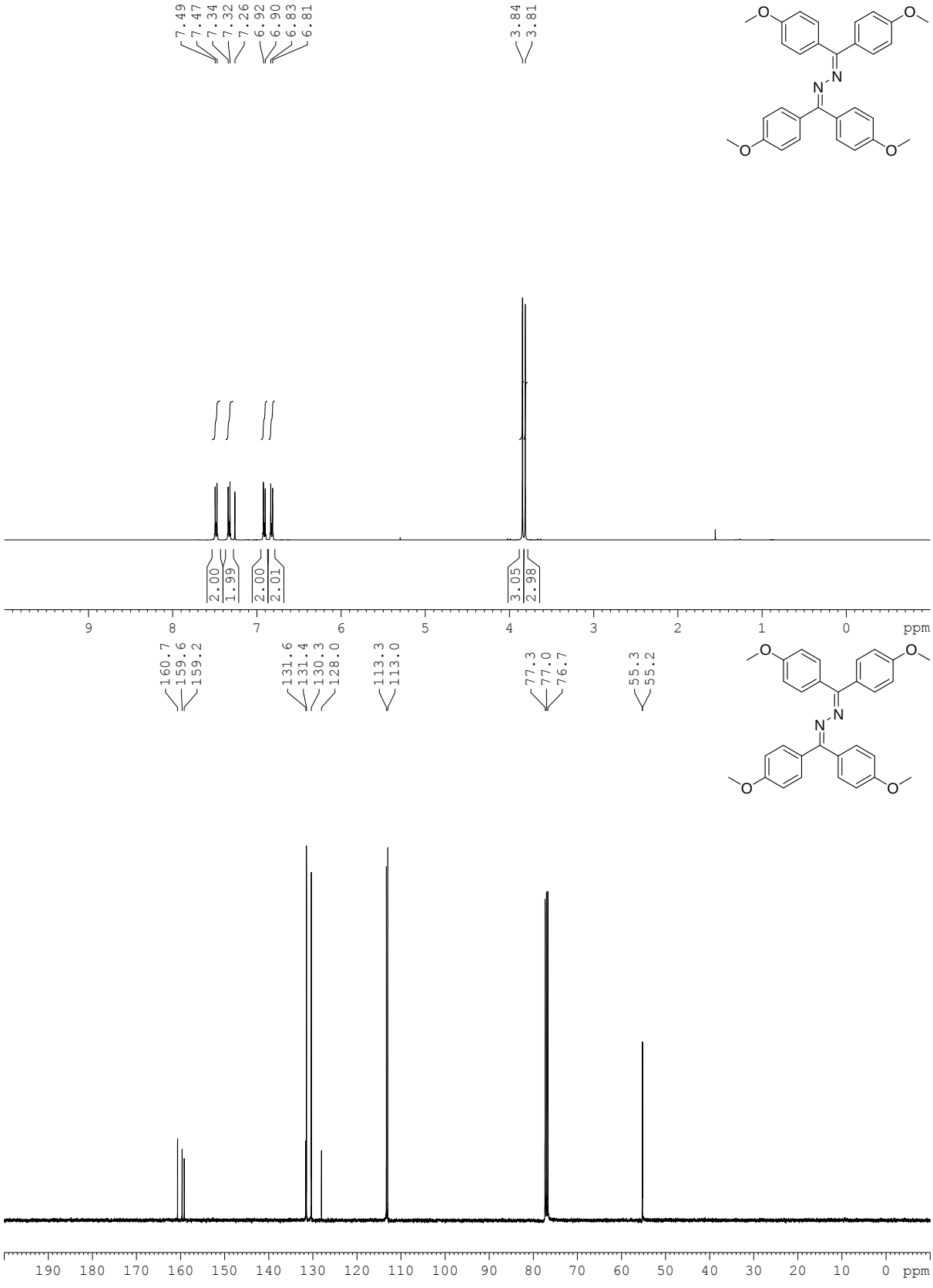

THEORY AND SPECTROSCOPY

Geometric Structure of $Rh_2(esp)_2$ and $BiRh(esp)_2$. The optimized (BP86/Def2-TZVP) structures of $Rh_2(esp)_2$ and $BiRh(esp)_2$ are shown in Figure S1. The two esp ligands are oriented such that they form a boat conformation. In the case of $Rh_2(esp)_2$, the Rh-O distances are not identical and amount to 2.058 Å and 2.064 Å, with the lower Rh^{2+} in Figure S1 featuring the longer Rh-O bond distances. This difference, albeit small, is significant and has its origin in the lower symmetry of the second coordination sphere. The Rh-Rh distance is calculated to be 2.385 Å, which is slightly longer than the distance of 2.275 Å between any two oxygen atoms of the same carboxylate, putting a minor strain on the paddlewheel.

A comparison of the optimized structures with experimental data is possible to some extent, although the crystal structure of $Rh_2(esp)_2$ features an additional acetone molecule axially coordinated to each Rh centre.[21] The Rh-Rh bond distance of 2.382 Å compares well to the calculated value. The crystal structure features both esp ligands in a chair conformation and, like in the calculation, small differences are still present in the crystallographically determined Rh-O distances (2.03 Å, 2.04 Å, 2.04 Å and 2.05 Å), whereby the shortest and longest distances occur for Rh-O bonds *trans* to each other. A selection of bond distances is summarized in Table S1.

For $BiRh(esp)_2$, the larger radius of Bi^{2+} gives rise to a longer Bi-O optimized bond distance of 2.408 Å, and thereby a more distorted paddlewheel. The Bi-Rh distance of 2.538 Å is much larger than the distance between the two oxygen atoms within the same carboxylate (2.275 Å). Therefore, whereas the O-Rh-O fragments are able to form an almost linear arrangement (angle larger than 176°), the O-Bi-O fragments are more bent (angle of 161°), as is shown in Figure S1.

The crystallographically determined structure of $BiRh(esp)_2 \cdot H_2O$ displays a Bi-Rh distance of 2.53(1) Å (this value represents a weighted average of the two Bi-Rh bond lengths determined in

the disordered solid-state structure, vide supra), similar to that found in the optimized geometry. The experimentally determined Rh-O and Bi-O distances are all slightly different, but fall within the ranges of 1.97-2.06 Å and 2.36-2.42 Å, respectively. The crystallographically determined solid state structure also features a chair-like conformation of the two esp ligands, in contrast to the boat-like structure obtained by the geometry optimization.

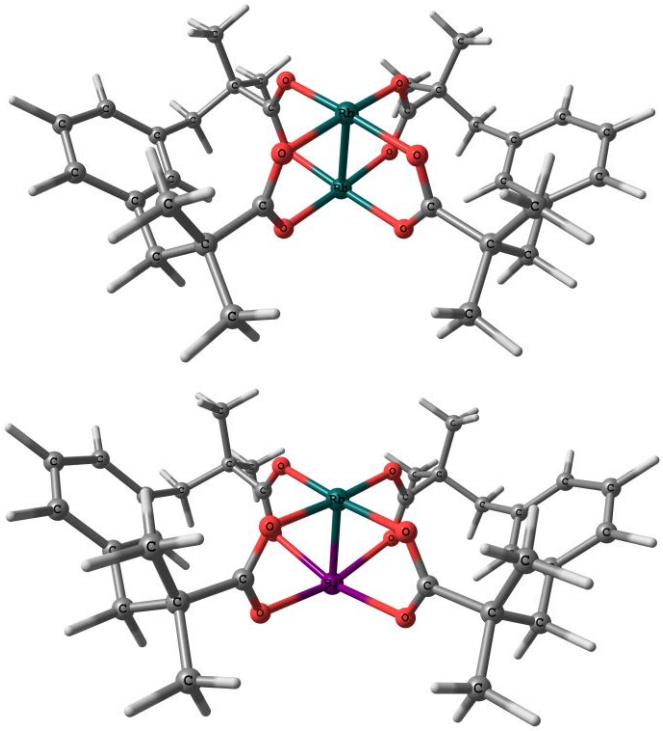

Figure S1. Geometry optimized structures of $Rh_2(esp)_2$ (top) and $BiRh(esp)_2$ (bottom).

Table S1. Selected Structural Parameters (Å) of Geometry Optimized and Crystallographically Determined Structures

	$Rh_2(esp)_2$		$BiRh(esp)_2$	
	DFT	**Exp[a]**	**DFT**	**Exp[b]**
M-Rh	2.385	2.382	2.538	2.53(1)
Rh-O	2.058	2.02-2.04	2.051	1.97-2.06
M-O	2.064	2.02-2.04	2.408	2.36-2.42

[a] $Rh_2(esp)_2 \cdot 2(OCMe_2)$.[21] [b] $BiRh(esp)_2 \cdot H_2O$.

Geometric Structure of $Rh_2(esp)_2C(p\text{-}MeOPh)_2$ (19) and $BiRh(esp)_2C(p\text{-}MeOPh)_2$ (20). The geometry optimized structure of $Rh_2(esp)_2C(p\text{-}MeOPh)_2$ (**19**), calculated at the BP86 level of theory, is given in Figure S2. It closely resembles the experimentally determined crystal structures of $Rh_2(TPA)_4C(p\text{-}MeOPh)_2$ and $Rh_2(esp)_2C(p\text{-}Me_2NPh)_2$ with similar Rh-Rh and Rh-C bond lengths (Table S2).[20,22]

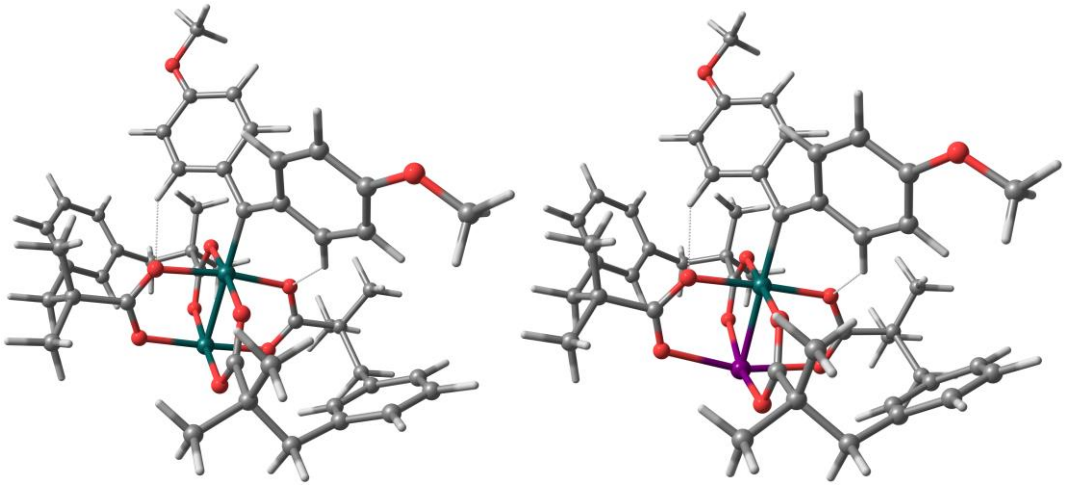

Figure S2. Geometry optimized structures of (left) $Rh_2(esp)_2C(p\text{-}MeOPh)_2$ (**19**) and (right) $BiRh(esp)_2C(p\text{-}MeOPh)_2$ (**20**).

Table S2. Selected Structural Parameters of Geometry Optimized and Crystallographically Determined Structures

	19		20
	DFT	**Exp[a]**	**DFT**
M-Rh	2.477 Å	2.438 Å	2.656 Å
Rh-C	2.022 Å	2.021 Å	2.139 Å
∠M-Rh-C	179.9°	177.4°	179.0°
Rh-O	2.087 Å	2.051 Å	2.088 Å
M-O	2.064 Å	2.043 Å	2.420 Å
C-C_{Ph}	1.449 Å	1.447 Å	1.444 Å

[a] $Rh_2(esp)_2C(p\text{-}Me_2NPh)_2$.[22]

The bismuth-rhodium analogue $BiRh(esp)_2C(p\text{-}MeOPh)_2$ (**20**), as before, exhibits significantly longer Bi-O bond distances than **19** owing to the larger ionic radius of Bi as compared to Rh. The paddlewheel core is essentially unchanged with respect to the starting compound.

A significant effect arising from changes in the M-Rh interaction relates to the elongated Rh-C distance of 2.139 Å for complex **20** as compared to 2.022 Å for complex **19**, which is a first and significant indication that the Bi-Rh and Rh-Rh cores interact in a fundamentally different way with the carbene ligand. Other noteworthy features are that the carbene ligand adopts a staggered conformation with respect to the carboxylate ligands in both complexes. Weak interactions between aryl C-H bonds and carboxylates are also apparent, in accordance with previous calculations as well as available experimental evidence.[20,22]

Electronic Structure of $Rh_2(esp)_2$. The $Rh_2(esp)_2$ complex features two Rh^{2+}, $4d^7$ ions. The complex (as well as all related complexes considered in this study) is diamagnetic, as confirmed by NMR spectroscopy. Quantum chemical calculations have been performed to investigate the electronic structure of this complex. Attempts to find a broken-symmetry singlet wave function invariably led to convergence to a closed-shell singlet state.

The overall 4d orbital structure as given by the DFT calculations is shown in Figure S3. Assignment of the orbitals in terms of symmetry labels has been performed under approximate D_{4h} symmetry of the first coordination sphere. Virtually every molecular orbital of Rh(4d) character is evenly delocalized over both Rh ions. The HOMO is a δ antibonding orbital of b_{2u} symmetry. The LUMO comprises the Rh-Rh σ^* orbital. The most stabilized orbital with Rh(4d) character is the Rh-Rh σ orbital. When considering the orbital energies as a crude approximation, the $\sigma \rightarrow \sigma^*$ transition is expected to be in the UV region of the electronic spectrum. The other

two unoccupied orbitals are formed by the $1b_{2u}$ and $1b_{1g}$ set, which is indeed expected for a square planar coordination geometry.

As a final note, since it is relevant for the observed spectroscopy (*vide infra*), a set of orbitals located on the aromatic part of the esp ligand has been located in between the $1e_u$ and $1b_{2g}$ orbitals.

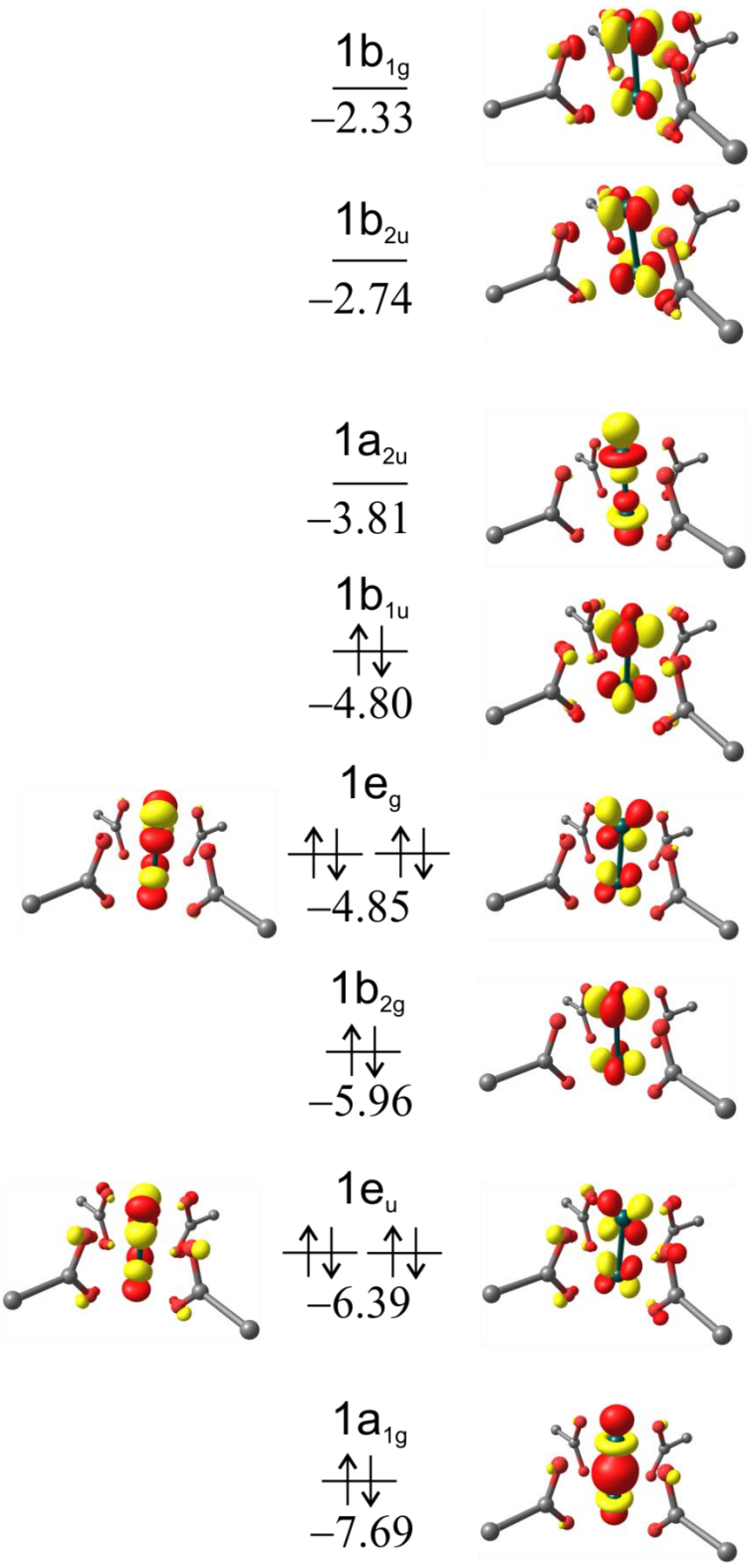

Figure S3. Molecular orbital scheme for $Rh_2(esp)_2$ with symmetry labels under approximate D_{4h} symmetry. The ligand structure has been truncated for purposes of clarity. Orbital energies in eV.

Electronic Structure of BiRh(esp)$_2$. As with the $Rh_2(esp)_2$ complex, $BiRh(esp)_2$ (Bi^{2+}, $6p^1$ and Rh^{2+}, $4d^7$) is diamagnetic and calculations did not give rise to broken symmetry solutions.

The frontier Bi(6p) and Rh(4d) centered molecular orbitals are depicted in Figure S4 and, in contrast to the corresponding dirhodium complex, the Bi(6p) and Rh(4d) orbitals are notably localized. Similarly to $Rh_2(esp)_2$, the Bi-Rh σ^* orbital constitutes the LUMO and the Bi-Rh σ orbital is lowest in energy within the Rh(4d)-Bi(6p) set. The σ^* orbital has more Bi($6p_z$) character and the σ orbital has mainly Rh($4d_{z^2}$) character. Within the Rh(4d) set, only the $1b_1$ orbital is unoccupied, as is again to be expected for a square planar environment. The 2e set of Bi(6p) orbitals is also unoccupied.

In a similar manner to the dirhodium case, it is worth noting that a set of esp-centered π orbitals has been found between the occupied $1a_1$ and 1e orbitals.

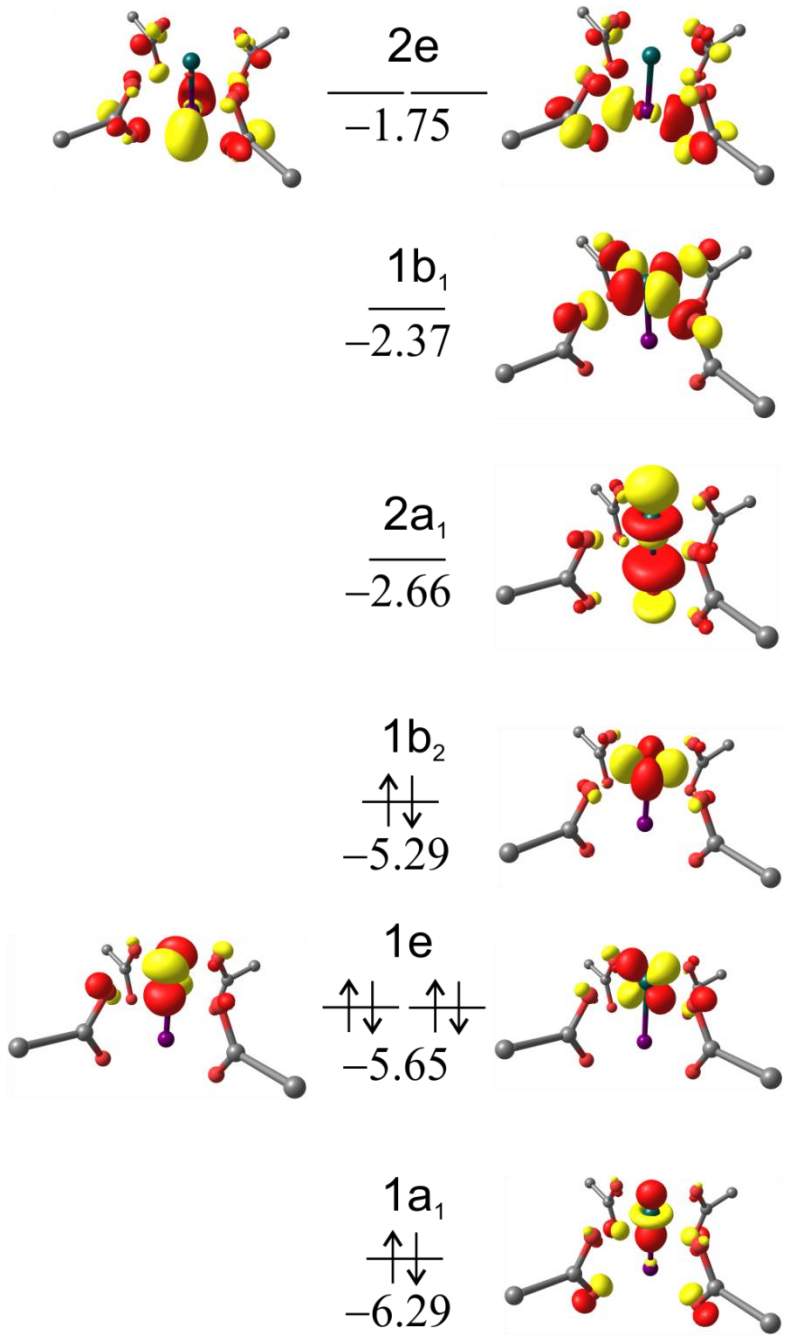

Figure S4. Molecular orbital scheme for $BiRh(esp)_2$ with symmetry labels under approximate C_{4v} symmetry. The structure has been truncated for purposes of clarity. Orbital energies in eV.

Electronic Structure of $Rh_2(esp)_2C(p\text{-}MeOPh)_2$ (19). The electronic structure of the $Rh_2(esp)_2C(p\text{-}MeOPh)_2$ carbene complex (**19**) largely mirrors that of $Rh_2(esp)_2$. The carbene is expected to engage in a σ-donating interaction with the Rh_2 $1a_{2u}$ orbital. Additionally, π-back-bonding is expected to occur, splitting each of the Rh e sets into two non-degenerate orbitals whose shape depends on the particular orientation of the carbene ligand, which in this complex takes up a staggered conformation.

Inspection of the resulting Rh(4d) orbitals and the carbene π* orbital (Figure S5) reveals exactly these interactions, with σ donation of the carbene ($1a_1$) and π back-donation from the $Rh_2(esp)_2$ e_g orbitals, now labelled as $2b_1$ and $2b_2$ owing to the reduction in symmetry to C_{2V} upon carbene binding. Otherwise, the orbital structure largely parallels that of $Rh_2(esp)_2$.

Other noteworthy aspects of the orbital structure are that the LUMO is now largely localized on the carbene π* orbital; the Rh-Rh σ* orbital, even more destabilized by the presence of the carbene, is now the LUMO+2. Similarly, the Rh-Rh $1a_1$ σ orbital is also destabilized and no longer lowest in energy. Rather, the $2b_2$ orbital now takes up this role. Most importantly, in contrast to $Rh_2(esp)_2$, the two Rh atoms are no longer equivalent, as is reflected by their unequal contributions to all orbitals in Figure S5.

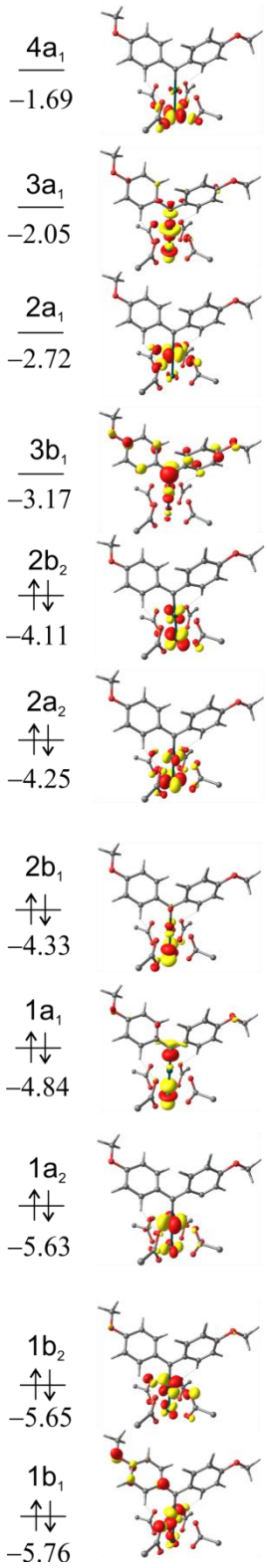

Figure S5. Molecular orbital scheme for $Rh_2(esp)_2C(p\text{-}MeOPh)_2$ (**19**) with symmetry labels under approximate C_{2V} symmetry. The ligand structure has been truncated for purposes of clarity. Orbital energies in eV.

Electronic Structure of $BiRh(esp)_2C(p\text{-}MeOPh)_2$ (20). The molecular orbital structure of $BiRh(esp)_2C(p\text{-}MeOPh)_2$ (**20**) is summarized in Figure S6. Similar to the dirhodium case, the orbital structure largely parallels that of the $BiRh(esp)_2$ starting complex with the additional carbene σ donating and π* back-donating interactions. The former interaction destabilizes the a_1 set, whereas interaction with the carbene π* orbital lifts the degeneracy of the e set. The HOMO is the Bi-Rh σ bonding $1a_1$ orbital; the carbene π* orbital ($2b_1$) constitutes the LUMO. The $1b_1$, $1b_2$ and $1a_2$ orbitals show virtually no π or δ interactions between Bi and Rh, respectively.

Also in this complex, a set of esp-centred π orbitals lie between the Bi(6p) and Rh(4d) set. In this case, the esp contribution is especially apparent, since the Bi $2b_2$ orbital mixes quite strongly with one of the esp-centered π orbitals.

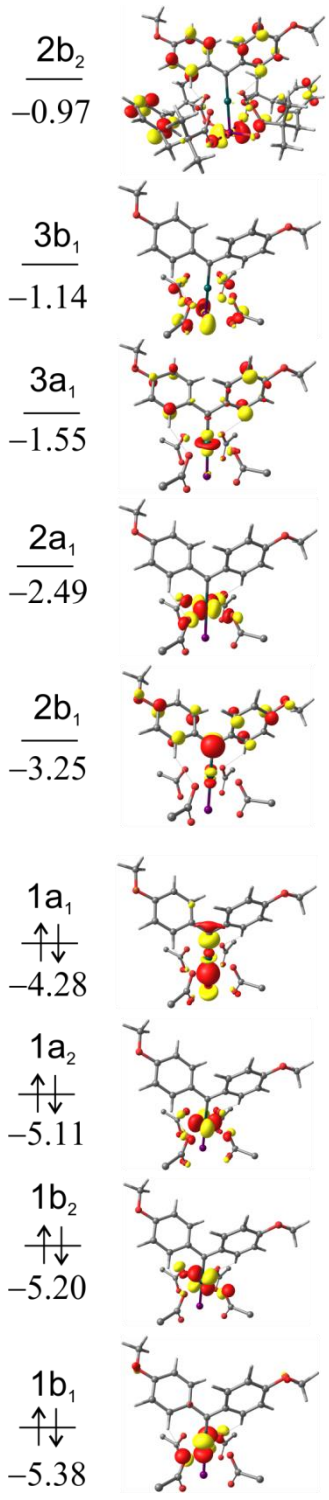

Figure S6. Molecular orbital scheme for $BiRh(esp)_2C(p\text{-}MeOPh)_2$ (**20**) with symmetry labels under approximate C_{2V} symmetry. The ligand structure has been truncated where possible for purposes of clarity. Orbital energies in eV.

In-Situ Generation of Complexes 19 and 20. Solutions of the 'donor-donor' carbene complexes **19** and **20** were generated at low temperatures upon addition of a purple CH_2Cl_2 solution of bis(para-methoxyphenyl)diazomethane (**18**) to CH_2Cl_2 solutions of the green $Rh_2(esp)_2$ or yellow $BiRh(esp)_2$ paddlewheel complexes (Scheme S1). NMR studies showed that a stoichiometric reaction of **18** with either paddlewheel complex produces a mixture of starting complex, carbene complex and diazine **21**, whose exact composition is highly sensitive to the reaction conditions (temperature, speed of addition of **18**, concentration). Solutions of complex **20** decayed (to $BiRh(esp)_2$ and diazine **21**) much more readily than the corresponding dirhodium complex **19**. Reference UV-Vis spectra were therefore collected of all starting materials and products such that, in the following spectroscopic studies, the spectroscopic signatures of the intermediate carbene species could be unambiguously identified.

Scheme S1. Reaction of 18 with $MRh(esp)_2$ (M = Rh or Bi)

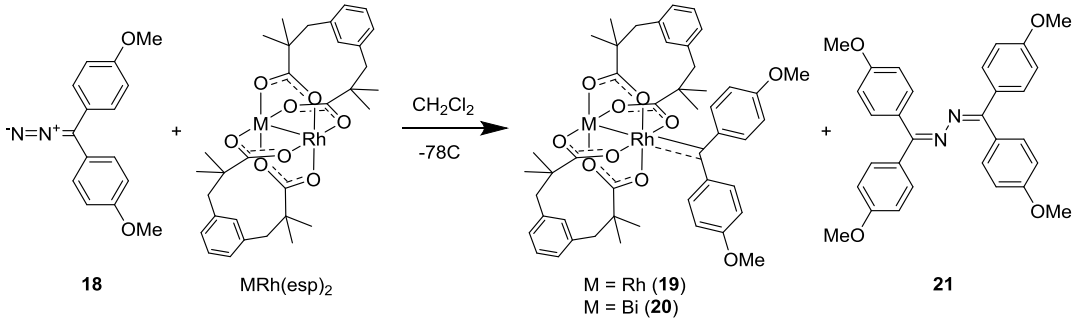

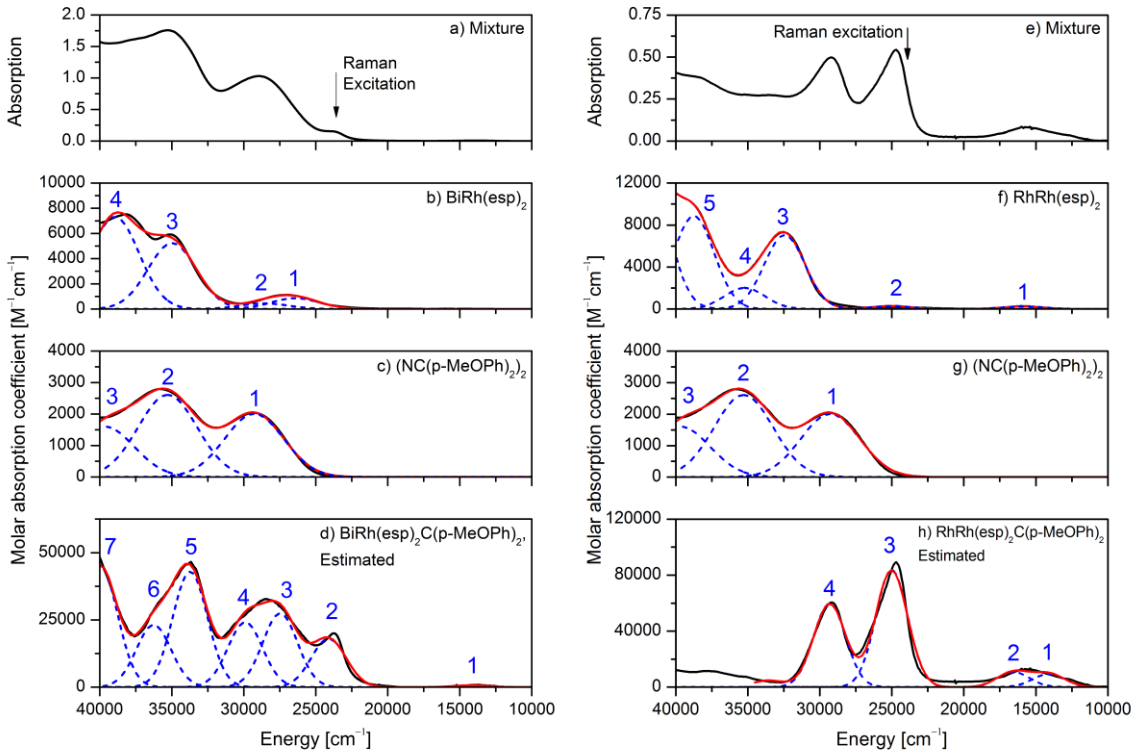

Figure S7. Overview of the absorption spectra recorded at -45°C of (a) a mixture of **20**, $BiRh(esp)_2$ and **21** (starting concentration of $BiRh(esp)_2$: 20 μM in CH_2Cl_2), (b) $BiRh(esp)_2$ (in CH_2Cl_2), (c) **21** (in CH_2Cl_2), (d) estimated spectrum of complex **20**, (e) a mixture of **19**, $Rh_2(esp)_2$ and **21** (starting concentration of $Rh_2(esp)_2$: 20 μM in CH_2Cl_2), (f) $Rh_2(esp)_2$ (in CH_2Cl_2), (g) **21** (in CH_2Cl_2), (h) estimated spectrum of complex **21**. A Gaussian deconvolution of all structural features is shown in blue and red.

UV-Vis Spectroscopy of $Rh_2(esp)_2$ and $BiRh(esp)_2$. UV-Vis spectra of $BiRh(esp)_2$ and $Rh_2(esp)_2$ are shown in Figure S7b and S7f. Both spectra have a similar appearance and consist of multiple intense bands in the UV, at energies above 30,000 cm^{-1}. The $BiRh(esp)_2$ complex also features two less intense bands in the region between 25,000 cm^{-1} and 30,000 cm^{-1}. For the $Rh_2(esp)_2$ complex, these bands are also present, but have a reduced molar absorption coefficient and one band is significantly bathochromically shifted to 15,881 cm^{-1}.

The spectra have been fitted and deconvoluted by Gaussians. Oscillator strengths and transition energies of the Gaussian bands are included in Table S3.

Table S3. Summary of Gaussian Deconvolutions of the UV-Vis Spectra of $Rh_2(esp)_2$, $BiRh(esp)_2$, 19 and 20

Band	$Rh_2(esp)_2$		$BiRh(esp)_2$		**19**		**20**	
	Center [cm^{-1}]	f_{exp}	Center [cm^{-1}]	f_{exp}	Center [cm^{-1}]	f_{exp}	Center [cm^{-1}]	f_{exp}
1	15,881	0.004	26,422	0.016	14,094	0.11	14,190	0.009
2	25,000	0.004	28,555	0.008	16,561	0.13	24,102	0.235
3	32,444	0.107	34,980	0.095	25,007	1.00	27,480	0.355
4	35,216	0.031	38,955	0.132	29,324	0.71	29,905	0.310
5	38,746	0.134					33,729	0.560
6							36,263	0.300
7							39,985	0.590

UV-Vis Spectroscopy of Diazine 21. The organic product of the reaction, diazine (NC(*p*-MeOPh)$_2$)$_2$ (**21**), was isolated and its UV-Vis spectrum recorded. The spectrum (Figures S7c and S7g) features two broad bands with energies above 25,000 cm^{-1} and molar absorption coefficients of about 3000 $M^{-1}cm^{-1}$. The spectrum can be well deconvoluted by 3 Gaussians.

The UV-Vis spectrum of **21** is required for a subtraction procedure in the next section but otherwise does not directly relate to the topic of investigating the electronic structures of $BiRh(esp)_2$ and $Rh_2(esp)_2$ and the carbene complexes **19** and **20**. For this reason, the bands in Figures S7c and S7g have not been further analysed, nor have quantum chemical calculations been performed for **21**.

UV-Vis Spectroscopy of Reaction Mixtures. UV-Vis spectra of reaction mixtures that feature the starting complexes, the diazine product **21** and the carbene complexes **20** and **19** are shown in Figures S7a and S7e, respectively. The spectra feature several new bands that do not overlap with any of those of the already discussed species. In particular, a weak band at about 23,000 cm^{-1} is

present in spectrum S7a. In spectrum S7e, there are two intense bands at about 24,000 cm^{-1} and 29,000 cm^{-1}, as well as a weaker composite band at 15,000 cm^{-1}. Since these bands do not overlap with any of the bands of $BiRh(esp)_2$, $Rh_2(esp)_2$ or **21**, they can be confidently assigned to the carbene complexes **19** and **20**.

Estimation of the UV-Vis Spectra of Complexes 19 and 20. In order to thoroughly analyze the electronic structures of the carbene complexes **19** and **20**, it would be advantageous to have knowledge of the UV-Vis spectra of the pure compounds. However, both carbene species are highly reactive intermediates and could not be isolated or attained in pure form, with the composition of reaction mixtures being very sensitive to the reaction conditions.

The procedure of estimating the UV-Vis spectrum of the carbene complex from a mixture is non-trivial and is therefore carefully described in this and the following paragraph. The main issue is that, mathematically, the task requires additional information: nothing mathematically speaks against assigning the spectra in Figures S7a and S7e to the pure compounds **20** and **19**. The reason for this is that the spectral overlap of the components contributing to the total UV-Vis spectrum in Figures S7a and S7e is principally unknown.

In an effort to extract information from the absorption spectrum, an attempt was made to obtain the absorption spectrum of pure **19** and pure **20** from the spectra of the mixtures by using additional information from NMR spectroscopy. NMR samples prepared analogously to those prepared for UV-Vis measurements showed that a stoichiometric reaction of **18** with $Rh_2(esp)_2$ leads to mixtures containing about 80% of **19**, whereas reaction with $BiRh(esp)_2$ results in mixtures containing only 30% of **20**. In Figure S7a, a much larger component of organic product **21** does indeed seem to be present than in Figure S7e, in agreement with the NMR data. Using

this information and additionally constraining the subtraction procedure to not lead to negative absorptions allows for an estimation of the spectra of the carbene complexes.

The as such obtained spectrum for complex **19** (S7h) has a more intense absorption spectrum in comparison to complex **20** with two intense bands at 25,007 cm^{-1} (ε = 85,000 $M^{-1}cm^{-1}$) and 29,324 cm^{-1} (ε = 50,000 $M^{-1}cm^{-1}$). In contrast, complex **20** features a band of much lower intensity in the corresponding region, but displays more structure in the blue part of the spectrum (S7d). Despite the complexes' intense green colors, only weak absorptions were apparent in the 600 nm - 800 nm range, with the dirhodium carbene complex **19** again having the more intense spectral features (**19**: υ = 16,561 cm^{-1}, ε = 11,445 $M^{-1}cm^{-1}$; υ = 14,094 cm^{-1}, ε = 10,300 $M^{-1}cm^{-1}$. **20**: υ = 14,190 cm^{-1}, ε = 290 $M^{-1}cm^{-1}$). The spectra of **19** and **20** have been deconvoluted by 4 and 7 Gaussians, respectively, to obtain the centers of the bands and oscillators strengths of the transitions, as indicated in Figures S7d, S7h and Table S3.

Although the estimated spectra in Figures S7d and S7h have to be used with caution, it is clear that both **19** and **20** have a well-defined and non-overlapping electronic transition at 24,000 cm^{-1} (415 nm). This allows for selective resonant excitation of **19** and **20** and thereby selective resonance enhancement by 3 to 4 orders of magnitude with respect to the other components of the reaction mixtures in resonance Raman spectroscopy.

Term Schemes. Based on the calculated electronic structures, term schemes for all four complexes have been constructed. They are given in Figures S8-S11. The figures, with labelling based on idealized symmetry of the first coordination sphere, include a summary of dipole allowed transitions, as indicated with red arrows. When considering electronic excitations for resonance Raman spectroscopy, it is noteworthy that only the z polarized transitions are expected

to be accompanied with a change in the M-Rh or Rh-C bond lengths; the x and y polarized dipole-allowed transitions will likely not induce a large geometry change.

Both starting compounds feature dipole forbidden transitions which are lower in energy than the first dipole-allowed transition. Coordination of the carbene opens up the possibility of additional dipole-allowed transitions into the carbene-centered π^* orbital. All charge transfer transitions into the carbene π^* orbital are expected to change the Rh-C bond length. As such, the carbene complexes are expected to give rise to large resonance Raman signals. In contrast, resonance enhancements are only expected for the starting compounds with z-polarized transitions which are expected to occur in the UV part of the spectrum. The term schemes therefore predict that the starting complexes will have poor resonance Raman enhancement when excited in the visible region.

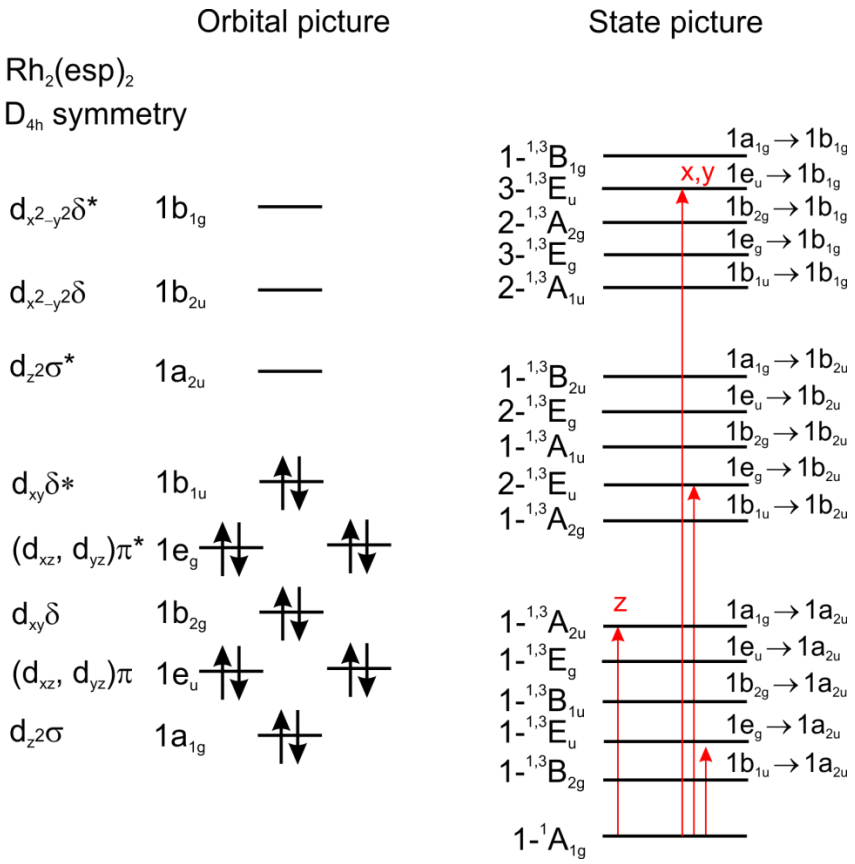

Figure S8. Term scheme for $Rh_2(esp)_2$. Dipole allowed transitions and their polarization are indicated in red. Note that the length of the arrows may not represent the actual order in which the optical transitions appear in the electronic spectrum.

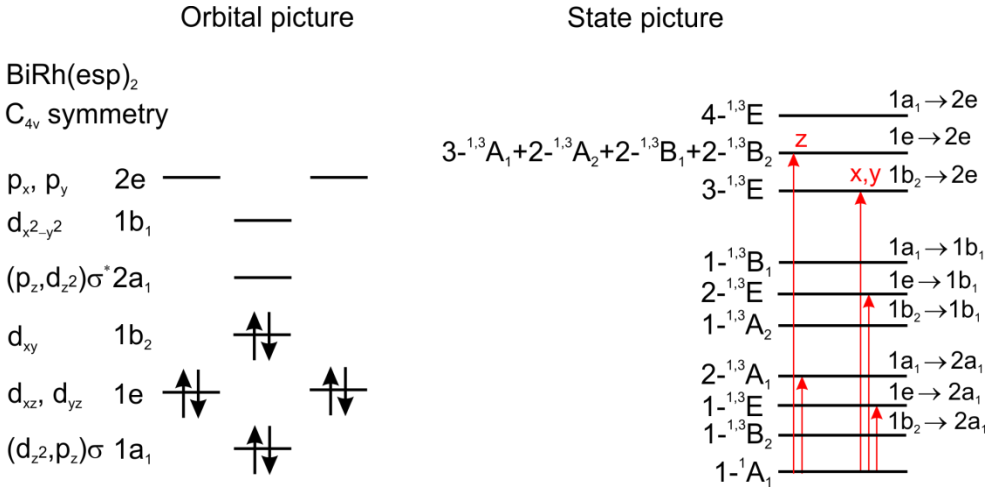

Figure S9. Term scheme for $BiRh(esp)_2$. Dipole allowed transitions and their polarization are indicated in red. Note that the length of the arrows may not represent the actual order in which the optical transitions appear in the electronic spectrum.

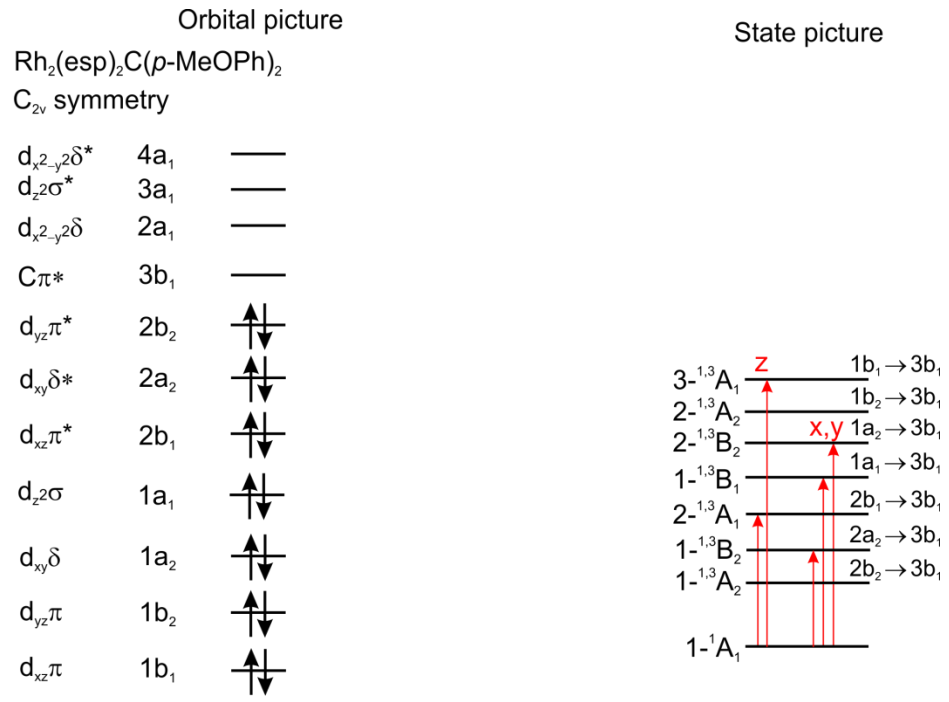

Figure S10. Term scheme for $Rh_2(esp)_2C(p\text{-MeOPh})_2$ (**19**). Dipole allowed transitions to the LUMO ($3b_1$) and their polarization are indicated in red. Note that the length of the arrows may not represent the actual order in which the optical transitions appear in the electronic spectrum.

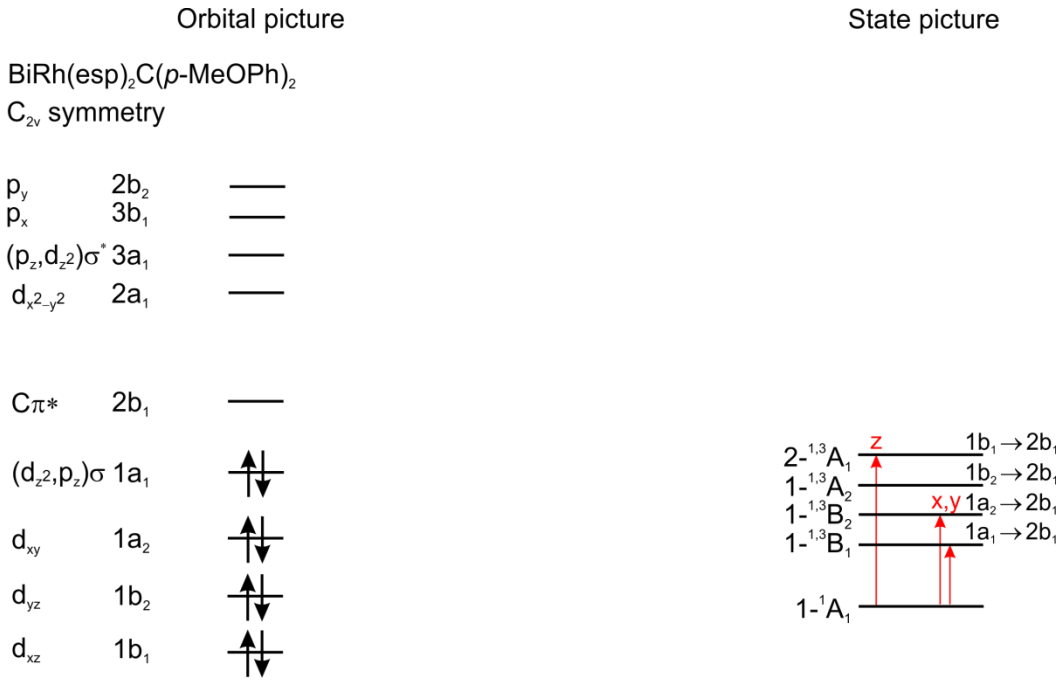

Figure S11. Term scheme for $BiRh(esp)_2C(p\text{-MeOPh})_2$ (**20**). Dipole allowed transitions to the LUMO ($2b_1$) and their polarization are indicated in red. Note that the length of the arrows may not represent the actual order in which the optical transitions appear in the electronic spectrum.

TDDFT Calculations of $Rh_2(esp)_2$ and $BiRh(esp)_2$. TDDFT calculations have been performed for the $Rh_2(esp)_2$ and $BiRh(esp)_2$ starting complexes (Figures S12 and S13). The calculated spectra reasonably well reproduce the bands observed in the experimental spectrum, as well as their intensities.

Inspection of the calculated difference densities of the most intense transitions, as well as of the natural transition orbitals for $Rh_2(esp)_2$, allow for an assignment of bands 1 and 2 to $2e_g \rightarrow 1a_{2u}$ and $1e_g \rightarrow 1b_{2u}$ transitions, respectively. In the UV region, multiple transitions from the carboxylate ($2p_x$, $2p_y$) e_g sets into the $1a_{2u}$ orbital are present. Band 4 of the Gaussian deconvolution unfortunately does not have a clear equivalent in the TDDFT calculations to allow for a definite assignment. Still, it is clear that bands 1 and 2 are d-d in nature, whereas bands 3 and 5 are oxygen-to-rhodium charge transfer (LMCT) transitions. One should also note that d-d transitions can be dipole allowed, or metal-to-metal in nature, in such bimetallic systems since a center of inversion is located in between the two Rh ions.

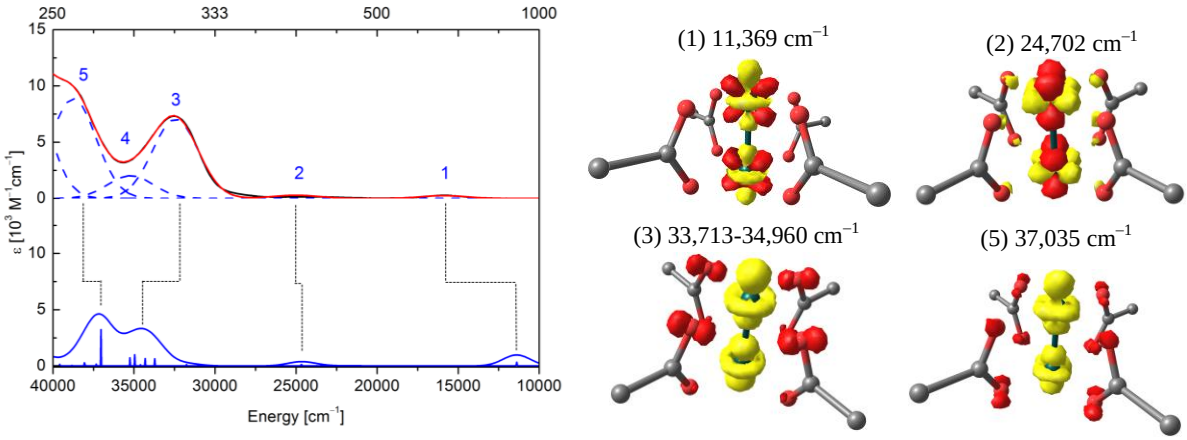

Figure S12. B3LYP, zora-def2-TZVP TDDFT calculation (bottom) of the absorption spectrum of $Rh_2(esp)_2$; Gaussian deconvoluted experimental spectrum (top) of $Rh_2(esp)_2$; difference densities for the transitions at 11,369 cm^{-1}, 24,702 cm^{-1}, 33,713-34,960 cm^{-1} and 37,035 cm^{-1} (red: negative; yellow: positive). The ligand structure has been truncated for reasons of clarity.

For $BiRh(esp)_2$, bands 1 and 2 correspond to the 1e $\rightarrow$ $2a_1$ transitions. However, both transitions feature a difference density with a significant deviation from idealized symmetry induced by the second coordination sphere, in that the positive density does not describe a pure a_1 (d_{z^2}) orbital, but takes on a flatter "$d_{z^2-x^2}$" shape, i.e., the $1b_1$ orbital mixes into the acceptor orbital. Bands 3 and 4 are $1b_2 \rightarrow 2e$ and $1e \rightarrow 2e$ transitions, respectively, and are best classified as Rh-to-Bi charge transfer transitions.

As already predicted by the term schemes, the d-d nature of transitions 1 and 2 will not induce large geometric changes. Therefore, excitation in the visible range is expected to afford small, if any, resonance Raman enhancements.

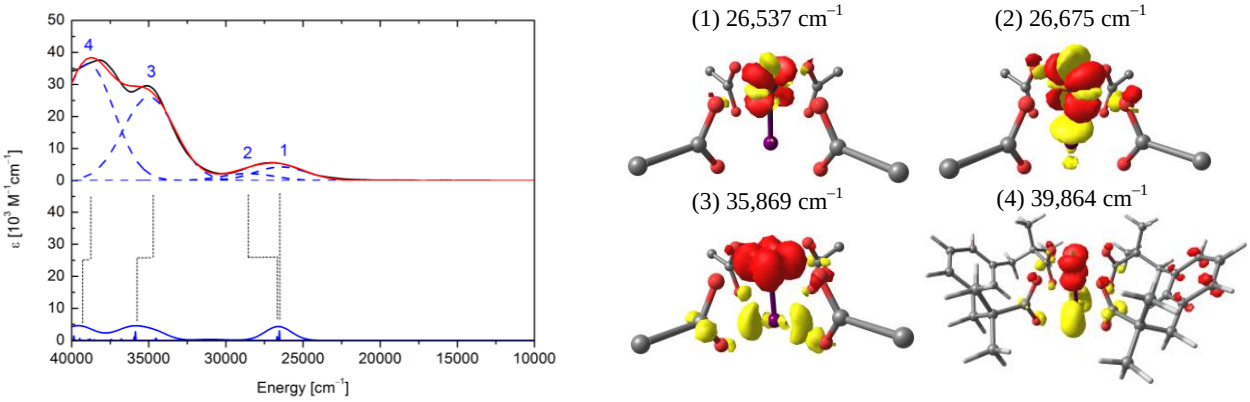

Figure S13. B3LYP, zora-def2-TZVP TDDFT calculation (bottom) of the absorption spectrum of $BiRh(esp)_2$; Gaussian deconvoluted experimental spectrum (top) of $BiRh(esp)_2$; difference densities (red: negative; yellow: positive) for the transitions at 26,537 cm^{-1}, 26,675 cm^{-1}, 35,869 cm^{-1} and 39,864 cm^{-1}. The ligand structure has been truncated where possible for reasons of clarity.

TDDFT Calculations of Complexes 19 and 20. TDDFT calculations and difference densities for the most pronounced transitions in the electronic spectra of the carbene complexes **19** and **20** are given in Figures S14 and S15, respectively. The agreement between the estimated experimental spectra and the TDDFT calculations is sufficient to warrant further interpretation.

For complex **19**, as predicted by the term schemes, the weak, low energy absorptions (bands 1 and 2) are weak Rh(distal) to carbene transitions of $2b_1 \rightarrow 3b_1$ and $1a_1 \rightarrow 3b_1$ character. The more intense bands 3 and 4 are characterized by charge transfer transitions. The former concerns a Rh(proximal) to carbene MLCT transition of $1b_2 \rightarrow 3b_1$ character, the latter is a mixed Rh(distal) to Rh(proximal) charge transfer transition for which the $2a_2 \rightarrow 2a_1$ and $1a_1 \rightarrow 3a_1$ transitions contribute.

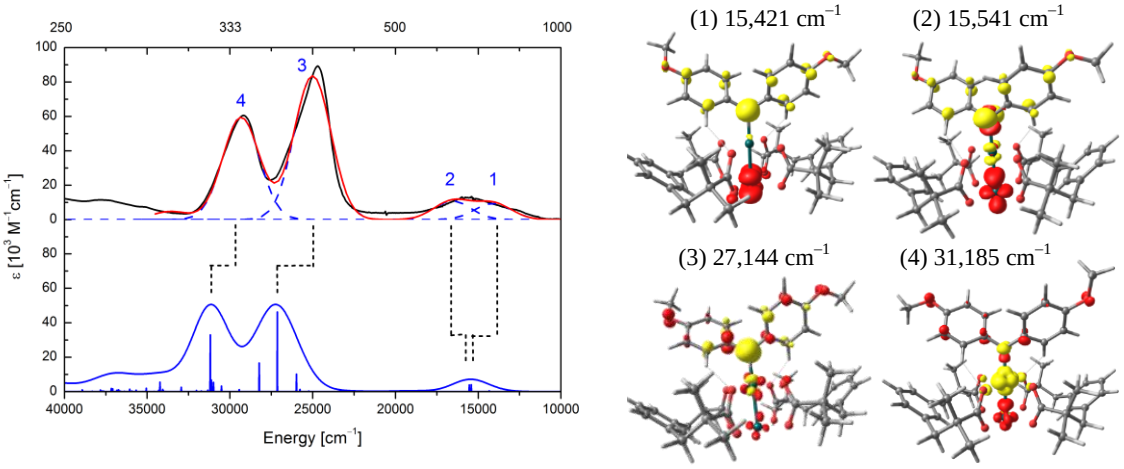

Figure S14. B3LYP, zora-def2-TZVP TDDFT calculation (bottom) of the absorption spectrum of complex **19**; Gaussian deconvoluted, estimated spectrum (top) of complex **19**; difference densities (red: negative; yellow: positive) for the transitions at 15,421 cm^{-1}, 15,541 cm^{-1}, 27,144 cm^{-1} and 31,185 cm^{-1}.

For complex **20**, band 1 represents a Bi to carbene charge transfer transition of $1a_1 \rightarrow 2b_1$ character which is dipole forbidden. Band 2 is assigned to a $\pi \rightarrow \pi^*$ ($2b_1$) transition involving the esp ligand and the carbene ligand. This transition has oscillator strength because a carbene π orbital mixes with a π orbital of the esp ligand. As such, the transition is best described as a classic ligand based $\pi \rightarrow \pi^*$ transition with oscillator strength derived from the carbene part of the donor and acceptor orbitals. Bands 3, 4 and 5 are all dipole allowed. Band 3 is a Rh(proximal) to carbene MLCT transition of $1b_1 \rightarrow 2b_1$ character. Band 4 represents a composite $\pi \rightarrow \pi^*$ ($2b_1$) transition involving the π systems of the esp and carbene ligands. Band 5 is best described as a combination of Bi to Rh and carbene to Rh charge transfers ($1a_1 \rightarrow 3a_1$). Bands 6 and 7 do not have clearly identifiable equivalents in the TDDFT calculation.

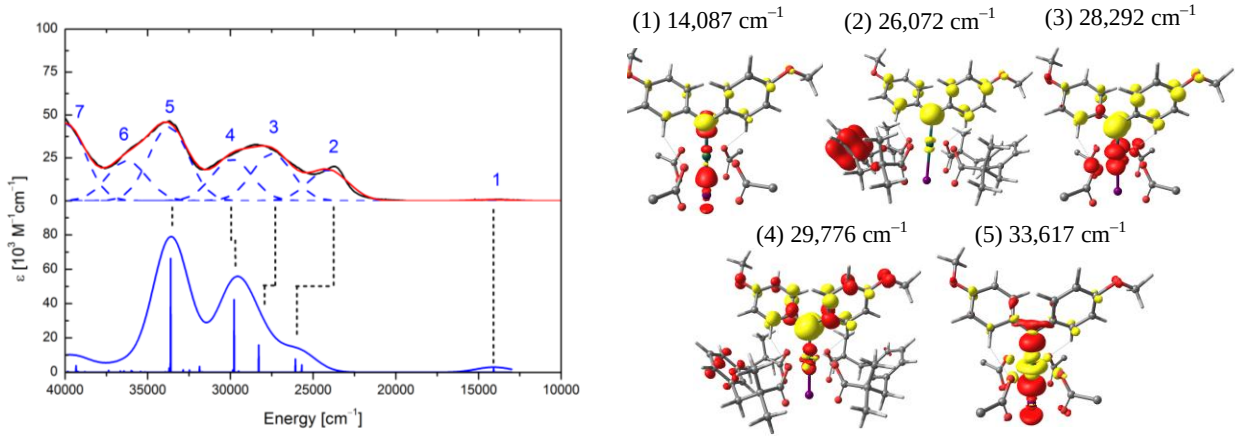

Figure S15. B3LYP, zora-def2-TZVP TDDFT calculation (bottom) of the absorption spectrum of complex **20** (shifted by +3000 cm^{-1}); Gaussian deconvoluted, estimated spectrum of complex **20** (top); difference densities (red: negative; yellow: positive) for the transitions at 14,087 cm^{-1}, 26,072 cm^{-1}, 28,292 cm^{-1}, 29,776 cm^{-1} and 33,617 cm^{-1}. The ligand structure has been truncated where possible for reasons of clarity.

Summary of the Nature of the Optical Transitions. Comparison of the electronic spectra of all four complexes with TDDFT calculations has allowed for assignment of all prominent bands in the electronic spectra. Most of these transitions involve Bi and Rh centered orbitals and, for the carbene species, the carbene centered π* orbital as an acceptor orbital. However, numerous additional bands are also present which are ligand centered (π → π*) in nature.

For $Rh_2(esp)_2$ and $BiRh(esp)_2$, the electronic spectra feature intense bands in the UV region and weak bands in the visible part of the spectrum. The latter correspond to d-d transitions whose molar absorption coefficients can still be up to 2,000 $M^{-1}cm^{-1}$ because of the bimetallic nature of the complexes. Nevertheless, these transitions are not expected to give rise to resonance Raman enhancement because d-d transitions are not likely to give rise to geometry changes of the molecule in the excited state. Resonance Raman enhancement is thus doubly penalized for these transitions which are (a) dipole forbidden and (b) give rise to small geometry changes. Resonance Raman enhancement is therefore expected to be only obtainable by excitation close to 40,000 cm^{-1} (250 nm), for which no laser is available in our laboratories.

For the carbene complexes **19** and **20**, the electronic spectra are richer and the situation for resonance Raman spectroscopy looks much more promising. The presence of the carbene π* acceptor orbital provides a new manifold of low-lying dipole allowed transitions which are Rh-to-carbene MLCT in nature. Furthermore, transitions in this manifold are z polarized and are expected to change the Rh-C and M-Rh bond distances upon electronic excitation.

When comparing the dirhodium and bismuth-rhodium variations of both the starting compounds and the carbene complexes, it becomes clear that the dirhodium complexes feature a richer and more mixed manifold of electronic transitions involving the 4d orbitals of both rhodium centers. In contrast, the bismuth-rhodium variations feature essentially disjointed sets of

Rh(4d) and Bi(6p) orbitals (with the exception of the $4d_{z^2}$ and $6p_z$ a_1 pair). It is important to note that 4d orbital mixing in the case of the dirhodium complexes results in the anti-bonding orbitals being destabilized and thus closer in energy to the LUMO than is the case of the bismuth-rhodium complexes.

Resonance Raman Spectroscopy of $Rh_2(esp)_2$ and $BiRh(esp)_2$. Resonance Raman spectra of the $Rh_2(esp)_2$ and $BiRh(esp)_2$ complexes are shown in Figure S16. As expected, the resonance enhancement is lackluster.

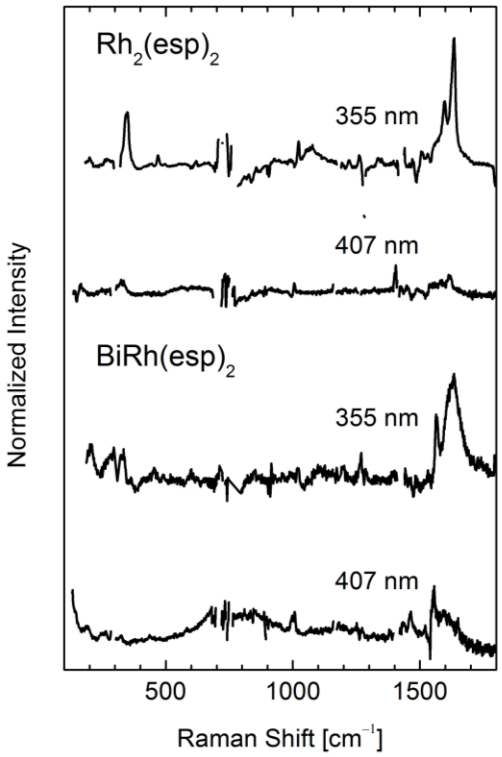

Figure S16. Normalized Raman spectra of $Rh_2(esp)_2$ and $BiRh(esp)_2$, recorded at 355 nm and 407 nm excitation (laserpower: 10 mW; T = 100 K).

The spectra recorded at 355 nm feature weak bands around 1,600 cm^{-1}. For $Rh_2(esp)_2$, an additional band appears at 320 cm^{-1}. For $BiRh(esp)_2$, bands at 300 cm^{-1} are apparent just above noise level. At excitation at 407 nm, neither complex gave Raman spectra with interpretable features.

Resonance Raman Spectroscopy of Complexes 19 and 20. Resonance Raman spectra were recorded for both carbene complexes upon selective electronic excitation with lasers at energies of 355 nm, 407 nm, 457 nm and 660 nm (730 nm in the case of **20**). In stark contrast to the starting complexes, vastly different vibrational spectra were obtained at each excitation wavelength with especially rich spectral features evident for both complexes upon excitation at 407 nm (Figure S17) and also for **19** at 660 nm, albeit with a lesser degree of resonant enhancement. Very few signals could be detected at 355 nm and 457 nm, with the latter wavelength providing essentially non-resonant excitation. Importantly, the observation of only a few signals at these wavelengths is a strong indication that no other Raman scatterers are present in the reaction mixture and that all signals observed at 407 nm excitation do stem from the carbene intermediates **19** and **20**.

As shown in Figure S17, the resonance Raman spectra of **19** and **20** recorded at 407 nm excitation are very similar in appearance and display intense bands from 200 cm^{-1} to 1,600 cm^{-1}. A list of prominent bands is given in Table S4. A description and formal assignment of these bands is provided in the following section.

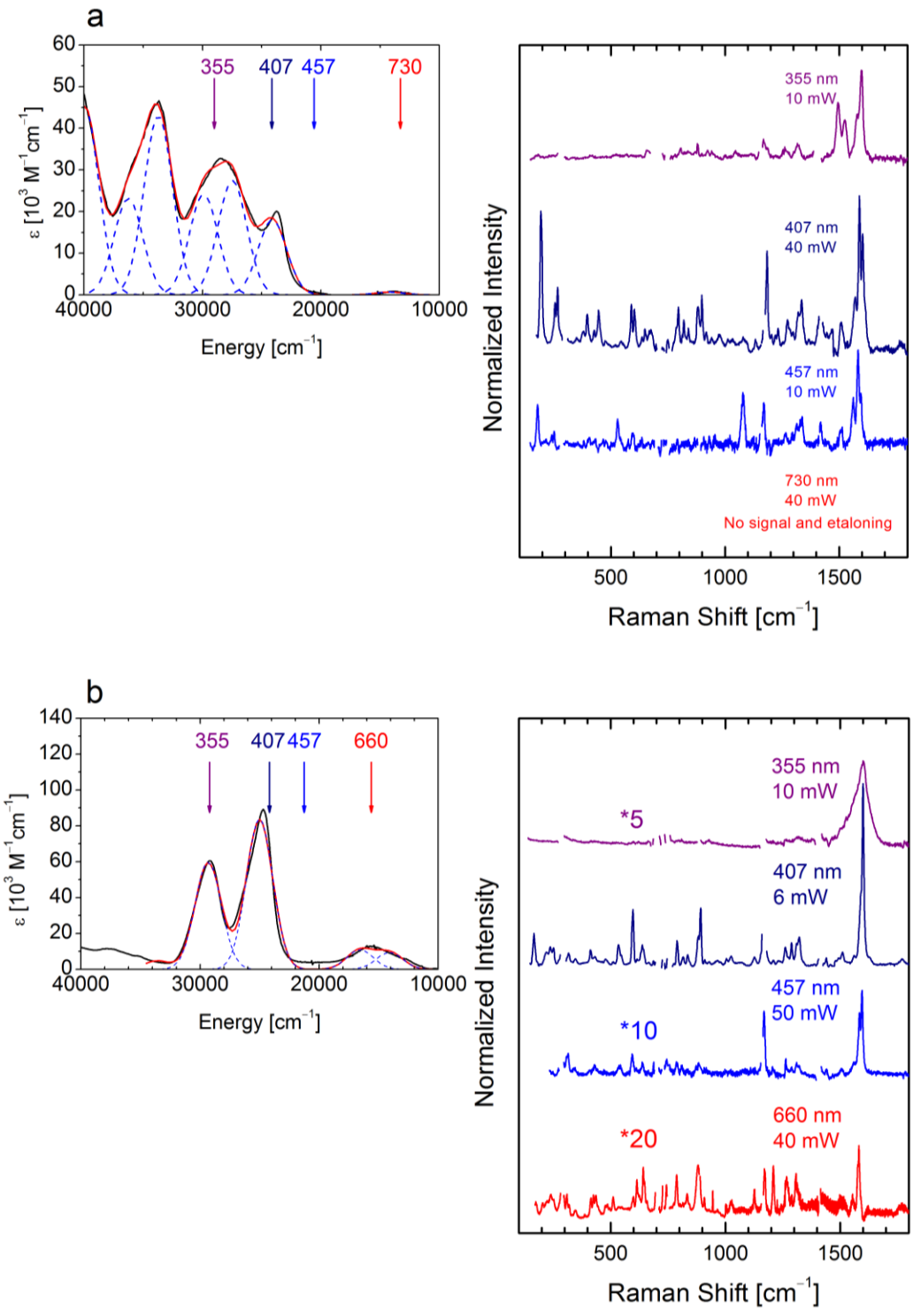

Figure S17. Normalized Resonance Raman spectra recorded at different wavelengths of (a) BiRh(esp)$_2$C(*p*-MeOPh)$_2$ (**20**) and (b) Rh$_2$(esp)$_2$C(*p*-MeOPh)$_2$ (**19**).

Table S4. Vibrational Bands (cm^{-1}) in the Resonance Raman Spectra of 19 and 20 Recorded with 407 nm Excitation.

	20	19
ν_1	193	
ν_2	261	237
ν_3	393	317
ν_4	442	412
ν_5	584	533
ν_6	602	597
ν_7	643	637
ν_8	711	
ν_9	792	789
ν_{10}	837	834
ν_{11}	878	
ν_{12}	896	893
ν_{13}	970	965
ν_{14}	1073	1026
ν_{15}	1129	1122
ν_{16}	1181	
ν_{17}	1271	1261
ν_{18}		1288
ν_{19}	1331	1321
ν_{20}	1503	1509
ν_{21}	1520	1561
ν_{22}	1597	1599

Assignment of Bands for $Rh_2(esp)_2$ and $BiRh(esp)_2$. Both starting compounds gave Raman spectra with a poor signal-to-noise ratio. However, at 355 nm excitation, a few bands could be discerned. TDDFT calculations (Figures S12 and S13) indicate that the bands at 355 nm comprise a large number of transitions with small oscillator strength, thereby inhibiting analysis of which transitions produce the observed resonance enhancement. For this reason, we only compare the vibrational frequencies and not the intensities of the bands.

In $Rh_2(esp)_2$, a band at 320 cm^{-1} appears in the experimental spectrum with 355 nm excitation. Interestingly, calculations indicate that the Rh-Rh stretching frequency occurs at 346 cm^{-1}. The $BiRh(esp)_2$ complex displays two bands at approximately 300 cm^{-1} which are just above noise level. The calculations predict the Bi-Rh stretching frequency to occur at 283 cm^{-1}. In both complexes, the good agreement between calculation and experiment (a discrepancy of 30 cm^{-1} is within the error of the calculations)[6b] suggests that we observe a small resonant enhancement of the M-Rh stretching frequencies upon electronic excitation at 355nm.

The bands observed around 1,600 cm^{-1} are at a frequency consistent with phenyl vibrations, and this is indeed reproduced by the calculations. Their resonant enhancement is due to excitation of electronic transitions involving the numerous phenyl-based orbitals of similar energies to the frontier metal-based orbitals (vide supra). A detailed interpretation of these ligand-based spectroscopic features is beyond the scope of this manuscript.

Assignment of Bands for Complexes 19 and 20. Of particular interest for the carbene complexes are the Bi-Rh, Rh-Rh and Rh-C vibrational frequencies expected around 200 cm^{-1}, 300 cm^{-1} and 850 cm^{-1}, respectively. These signals are expected to become enhanced in intensity when electronic transitions associated with significant changes to the corresponding normal

coordinates are excited. Therefore, excitation of bands 3 and 4 for complex **20** and of bands 4 and 5 for complex **19** are predicted to induce a change of the Rh-C and M-Rh bond lengths.

A full and reliable assignment of the experimentally observed bands in the Raman spectra requires critical comparison to quantum chemical calculations with respect to both frequency and intensity. In that respect, one of the first things to mention is that for resonance Raman spectroscopy, one can by no means expect good agreement between experiment and theory by considering any single resonant excitation in isolation. A few general remarks are in order. While it is certainly helpful to deconvolute the UV-Vis spectra with a limited set of Gaussians and assign the Gaussians' peak positions to those calculated transitions that dominate the oscillator strength, it is clear that many more transitions of lower oscillator strength involving different orbitals are also present and will also be excited by the same laser irradiation. The experimental resonance enhancement of these low oscillator strength transitions can still be significant if the corresponding Raman activity is sufficiently large. Given these boundary conditions, the calculations of the resonance Raman spectra (Figure S18) show remarkably good agreement between experiment and theory with respect to both the vibrational frequencies and intensities.

Analogously to $Rh_2(esp)_2$ and $BiRh(esp)_2$, significant resonant enhancement of phenyl-based vibrations (approximately 1600 cm^{-1}) was observed for complexes **19** and **20**. In light of the arguments in the previous paragraph, this is easily understood by noting the presence of numerous phenyl-based orbitals with energies similar to those of the metal-based orbitals of each complex (vide supra).

While the frequency fingerprints of **19** and **20** are relatively accurately reproduced by calculation, simulation of the intensities is difficult for the afore-mentioned reasons. Nonetheless, the Raman spectrum calculated for complex **19** upon simulated excitation of the Rh $\rightarrow$ C MLCT

transition (band 3 in the UV-Vis spectrum) reproduces the intensities in the lower frequency part of the spectrum remarkably well. The most enhanced frequencies can clearly be identified by comparison of experiment and theory. The Rh-Rh stretching vibration delocalizes over multiple modes and contributes to numerous bands between 283 cm^{-1} and 305 cm^{-1} (Figure S19). More importantly, the calculated vibrations with Rh-C character are found at 585 cm^{-1}, 771 cm^{-1} and 873 cm^{-1} and these bands are indeed clearly enhanced in the experimental spectra (Figure S18). Calculations indicate that for complex **20**, the Bi-Rh stretching frequency contributes to modes at 177 cm^{-1} and 251 cm^{-1}; the Rh-C frequency is found at 759 cm^{-1} and 853 cm^{-1} (Figure S20). Gratifyingly, there is good agreement between experiment and theory (Figure S18).

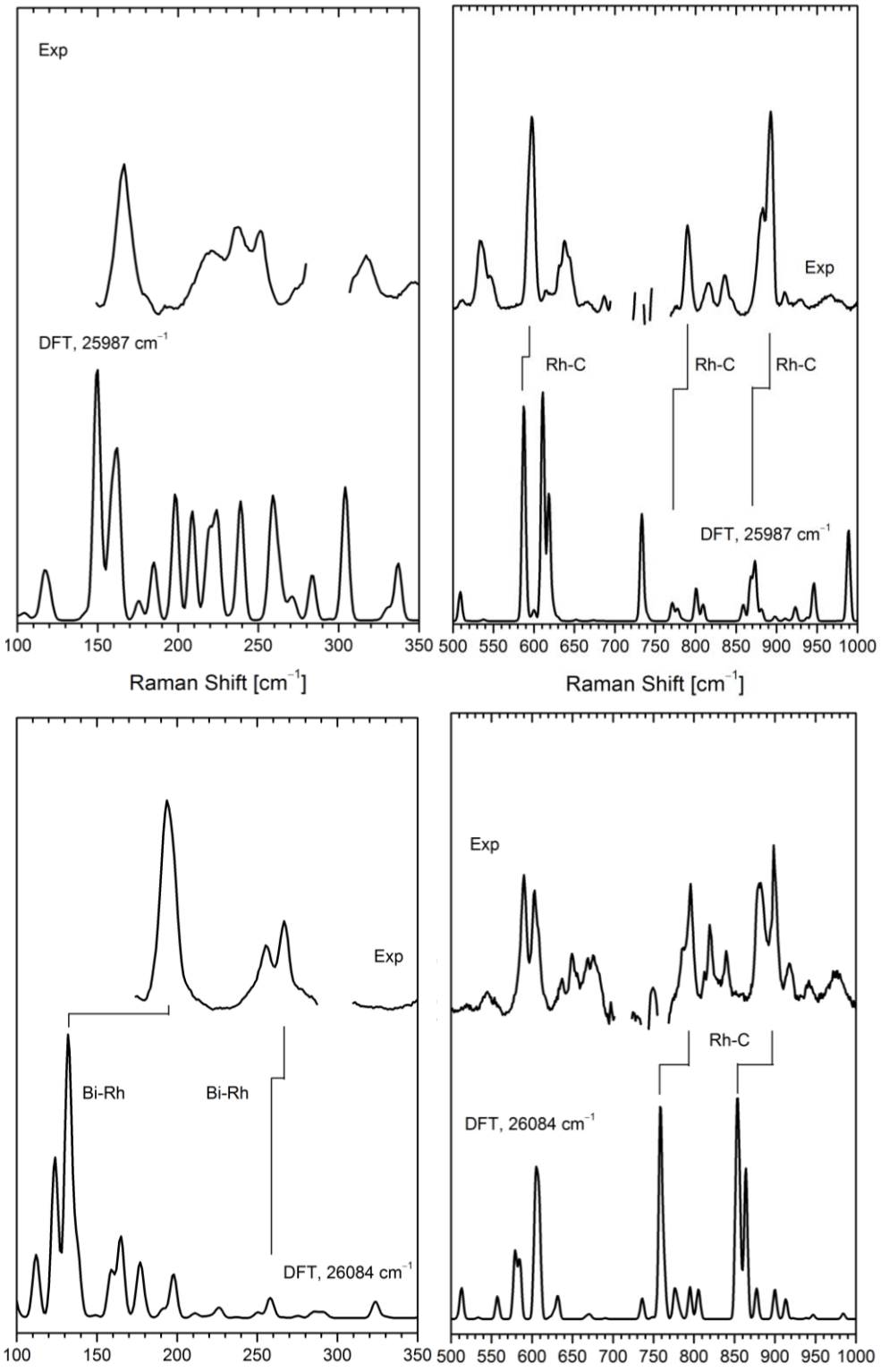

Figure S18. Experimental (above) and calculated (below) resonance Raman spectra of $Rh_2(esp)_2C(p\text{-}MeOPh)_2$ (**19**, top) and $BiRh(esp)_2C(p\text{-}MeOPh)_2$ (**20**, bottom) recorded at 407 nm excitation (6 mW and 40 mW, respectively).

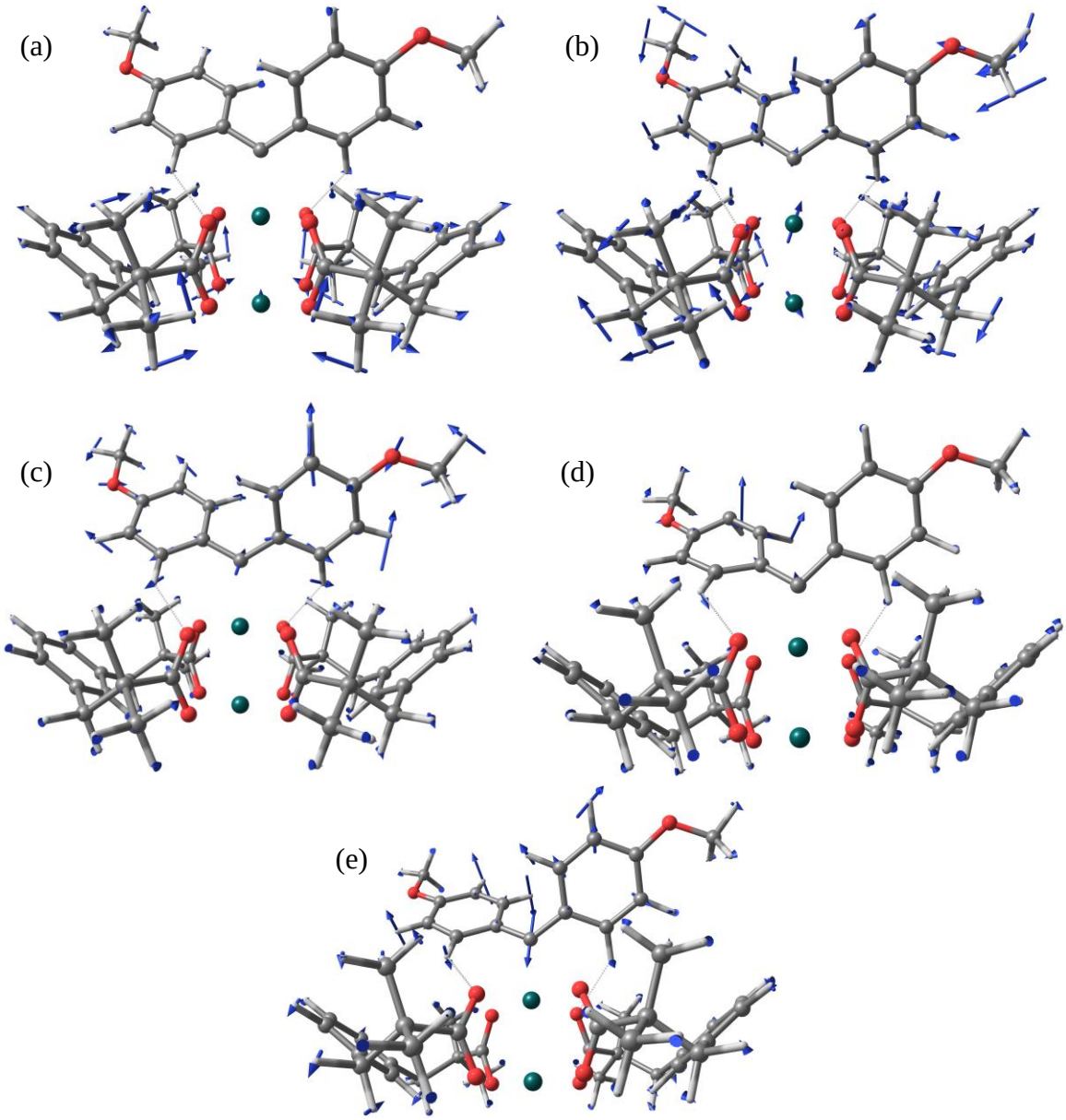

Figure S19. Schematic representation of the normal modes (atomic displacements indicated with arrows) for complex **19** with Rh-Rh stretching character at (a) 283 cm^{-1} and (b) 305 cm^{-1} and with Rh-C stretching character at (c) 585 cm^{-1}, (d) 771 cm^{-1} and (e) 873 cm^{-1}. Note that the large mass of Rh causes the actual displacements of these atoms to be proportionally small and that the atoms in the outer coordination sphere may display large displacements as a result of collective non-vibrational movement of these more distant groups as induced by small changes of an internal coordinate in the first coordination sphere of the molecule. The bonds to rhodium have been artificially removed in order to increase visibility of the arrows.

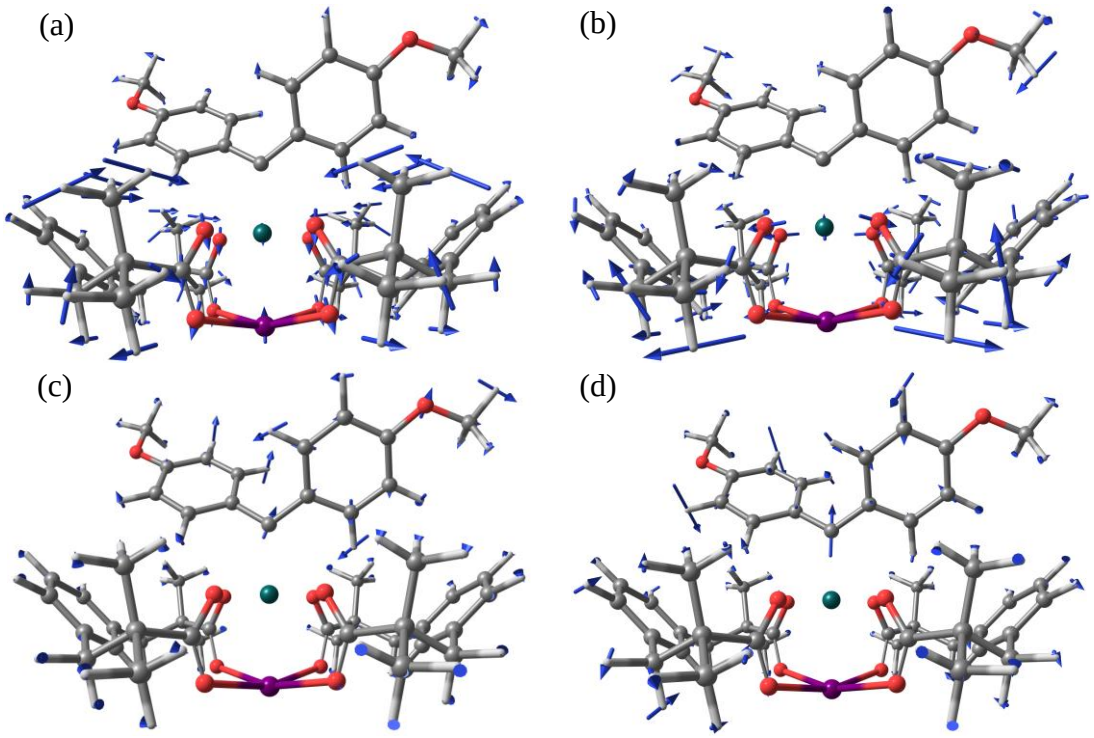

Figure S20. Schematic representation of the normal modes (atomic displacements indicated with arrows) for complex **20** with Bi-Rh stretching character at (a) 177 cm^{-1} and (b) 251 cm^{-1} and with Rh-C stretching character at (c) 759 cm^{-1} and (d) 853 cm^{-1}. Note that the large masses of Bi and Rh cause the displacements of these atoms to be proportionally small and that the atoms in the outer coordination sphere may display large displacements as a result of collective non-vibrational motion induced by small changes of an internal coordinate in the first coordination sphere of the molecule. The bonds to the rhodium atom have been artificially removed in order to increase visibility of the arrows.

Summary. In summary, the previous sections provide a detailed analysis through UV-Vis and resonance Raman spectroscopy of the electronic structure of the precursor complexes $Rh_2(esp)_2$ and $BiRh(esp)_2$ as well as the carbene complexes $Rh_2(esp)_2C(p\text{-}MeOPh)_2$ (**19**), $BiRh(esp)_2C(p\text{-}MeOPh)_2$ (**20**). The observation of resonance Raman enhancements and their reproduction by computation (S18), together with the good agreement of the experimental and calculated UV-Vis spectra (S14 and S15), provides confidence in both the successful formation of the carbene complexes as well as in our computational methodology.

The starting compounds are characterized by strong bands in the UV region of the spectrum and a set of d-d transitions in the visible region of the spectrum. Upon carbene binding, an additional carbene-centered π^* orbital takes on the role of the LUMO, affording rhodium-to-carbene MLCT transitions and giving rise to much more pronounced spectroscopic features.

Upon excitation of such MLCT transitions, rich resonance Raman spectra of carbene complexes **19** and **20** have been recorded. Analysis shows that the Rh-Rh stretching frequency of **19** mixes into multiple bands in the frequency range of 283 cm^{-1} to 305 cm^{-1} and the Rh-C stretching frequency mixes into bands at 585 cm^{-1}, 771 cm^{-1} and 873 cm^{-1}. For complex **20**, the Bi-Rh stretching frequency occurs in two modes at 177 cm^{-1} and 251 cm^{-1} and Rh-C frequencies occur in modes at 759 cm^{-1} and 853 cm^{-1}.

The largest differences between the dirhodium and bismuth-rhodium complexes stem from the fact that the two Rh(4d) manifolds mix in the former case, whereas the Bi(6p) and Rh(4d) orbitals are more localized (with the exception of the a_1 symmetry orbitals) in the latter case. This Rh(4d)-Rh(4d) orbital mixing causes the dirhodium anti-bonding 4d orbitals to be destabilized relative to the localized Rh(4d) orbitals in the bismuth-rhodium case. As a result, the dirhodium paddlewheel is able to bind more covalently to the carbene and form a stronger bond, with

stronger π back-donation interactions to the carbene. This is exemplified by complex **19** having, for example, an increased Rh-C stretching frequency and a shorter Rh-C bond than complex **20**.

Electronic Structure of $Rh_2(esp)_2C(H)(COOEt)$ (22) and $BiRh(esp)_2C(H)(COOEt)$ (23). Following our combined experimental and theoretical investigation into the more stabilized 'donor-donor' carbene complexes **19** and **20**, we turn our focus now to the corresponding carbene complexes derived from ethyl diazoacetate (**22** and **23**) for which novel reactivity was observed. Complexes **22** and **23** are highly reactive intermediates and cannot be generated in sufficient concentrations for the measurement of spectroscopic data. Cautious of the use of calculations without verifiable observables, we have invested significant effort into the study of complexes **19** and **20** to validate our computational methods. Satisfied with the level of agreement between our calculations and our experimental data, we feel justified in applying these calculations to the investigation of the electronic structure of these more unstable carbene systems.

An important difference between the donor-donor carbene complexes **19** and **20** and the acceptor-type carbene complexes **22** and **23** is the orientation of the carbene with respect to the carboxylate framework. Whereas this is staggered in complexes **19** and **20**, the carbene in complexes **22** and **23** is eclipsing one axis of the paddlewheel. Consequently, only the d_{xz} orbitals are able to provide a π-bonding interaction, with the d_{yz} being orthogonal to the carbene p_x orbital.

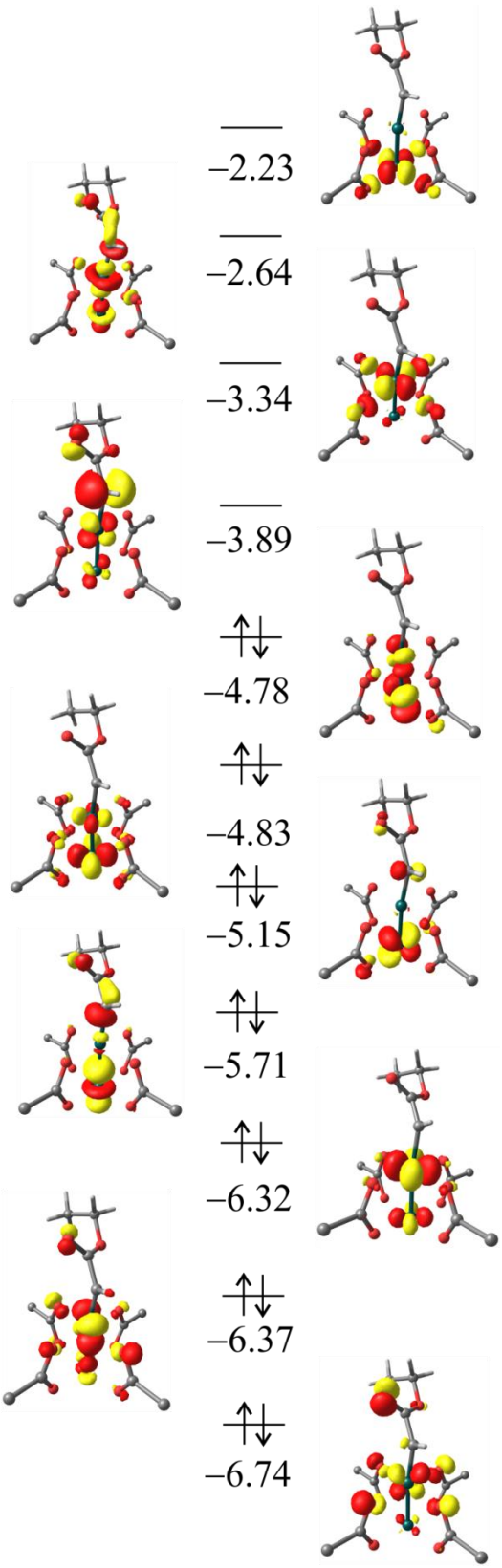

Figure S21 Molecular orbital scheme for $Rh_2(esp)_2C(H)(COOEt)$ (**22**). The ligand structure has been truncated where possible for purposes of clarity. Orbital energies in eV.

Inspection of the calculated electronic structure of the dirhodium carbene complex **22** (Figure S21) reveals the expected σ-donating interaction of the carbene with the $Rh_2(esp)_2$ $1a_{2u}$ orbital. The resulting C-Rh-Rh σ orbital (-5.71 eV) lies below the Rh-Rh π and δ antibonding manifold in energy. The π-back-bonding interaction of the d_{xz} anti-bonding orbital with the carbene splits the e set of $Rh_2(esp)_2$ into two non-degenerate orbitals (-4.78 eV and -5.15 eV). This interaction is significantly stronger than that in complex **19**, with a large energy splitting of 0.37 eV (c.f. 0.22 eV for complex **19**). Another measure of the strength of this back-bonding interaction is the Mulliken population of the carbene p_x lobe of the Rh(d_{xz})-C(p_x) (-5.15 eV) orbital. At 19.1%, this reflects a significant π back-donation of electron density from Rh to the carbene (c.f. 3.4% in complex **19**).

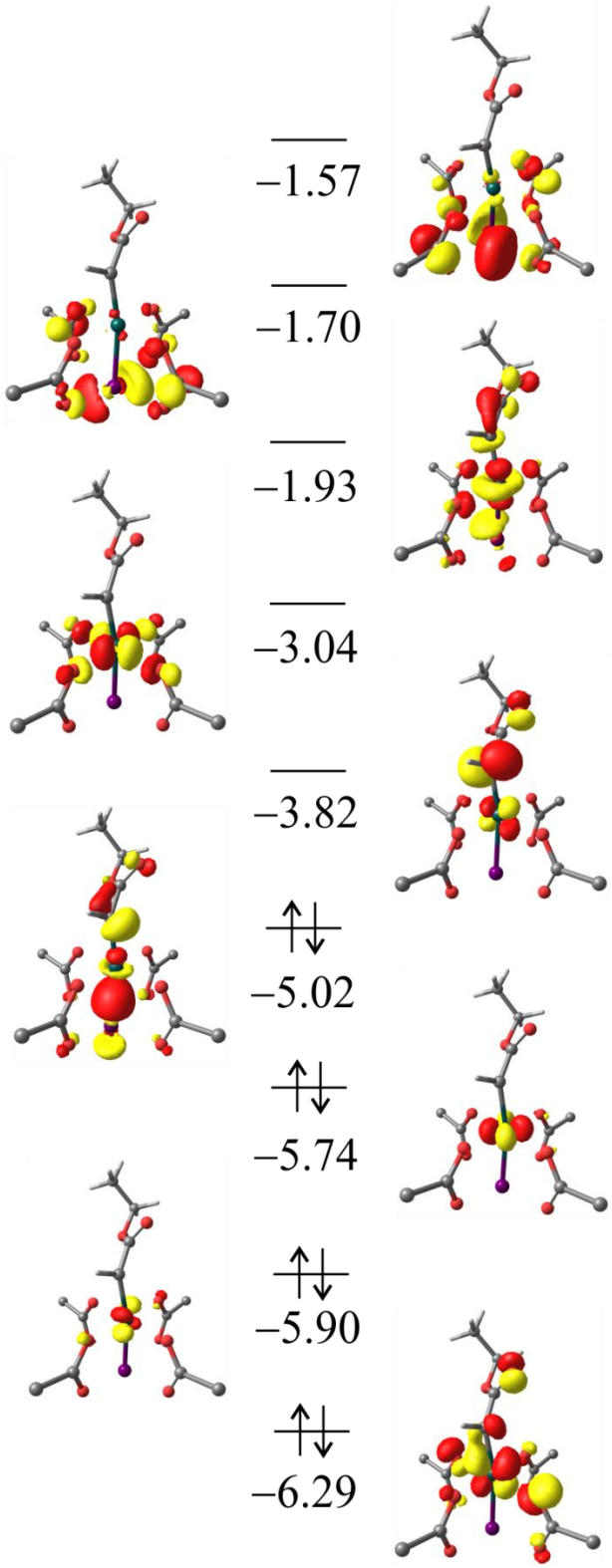

Figure S22 Molecular orbital scheme for $BiRh(esp)_2C(H)(COOEt)$ (**23**). The ligand structure has been truncated where possible for purposes of clarity. Orbital energies in eV.

In contrast to the dirhodium carbene complex **22**, the C-Rh-Bi σ orbital of bismuth-rhodium carbene complex **23** lies higher in energy (-5.02 eV) than the Rh(4d) orbitals. This mirrors the comparison between complexes **19** and **20**, with the origin lying in dirhodium complexes exhibiting mixing of Rh(4d) orbitals and bismuth-rhodium complexes having highly localized metal orbitals. Although interaction of the Rh(d_{xz}) orbital with the carbene does result in rehybridization of the e set in an analogous manner to complex **22**, direct comparison of the strength of this interaction is complicated by accidental degeneracy of the Rh(d_{yz}) orbital with an esp based phenyl orbital. Nevertheless, the Mulliken population of the Rh(d_{xz})-C(p_x) (-6.29 eV) orbital is still informative, showing significantly less delocalization (6.1%) to the carbene than the corresponding orbital in complex **22** (19.1%).

CARTESIAN COORDINATES [Å] OF GEOMETRY OPTIMIZED STRUCTURES

$Rh_2(esp)_2$

C	4.76420031352962	9.65788098149454	8.00897920386934
C	5.34006874576943	8.56285827369277	7.08983839428903
C	6.73751847594353	9.01741917363366	6.54609662204376
H	7.41502538744390	9.12069279463264	7.40672657313552
H	7.11747622812913	8.18910177328104	5.92607090793808
C	6.73594215757191	10.30410270193011	5.75081637921105
C	6.61959943079037	10.31839407299164	4.35174596491729
H	6.57264285380323	9.37559257192104	3.80179114037222
C	6.57440364090417	11.53177511663913	3.65876676103611
H	6.49946474860965	11.53177519294220	2.56900062931759
C	6.82661784187547	11.53177499643516	6.42203943620359
H	6.95639165952931	11.53177486821980	7.50529516226508
C	5.54845811732727	7.29453905575574	7.94856356041671
H	5.99165786851187	6.49869019567148	7.33073843219974
H	6.21671312791855	7.49473850476554	8.79626989928058
H	4.59062044696696	6.92242276992044	8.34071204170781
C	4.37398738420442	8.25867660676418	5.93583017552057
H	4.80485080831606	7.47137330900299	5.29751871001092
H	3.40633150595152	7.90432790176417	6.31400488748330
H	4.18800284107419	9.14506489246597	5.31636620881029
C	2.80686225897386	9.65565637364984	11.19961300478865
C	2.24575855702838	8.55700967514402	12.12372157838575
C	2.36886736746720	9.01537340426063	13.61672653895409
H	1.97364694872702	8.19160445420133	14.23264119714357
H	3.43914886024915	9.11311914128198	13.85141970442157
C	1.65718914775819	10.30389540068565	13.96298786925370
C	0.35932670449422	10.31862391293340	14.49837345472189
H	-0.15003219993504	9.37614027108344	14.71358204000389
C	-0.27920559150658	11.53177538806736	14.77247338659737
H	-1.28226192231084	11.53177556529348	15.20318966768447
C	2.29456873236847	11.53177488502153	13.73258790627007
H	3.31407409446366	11.53177466347785	13.34619439946040
C	3.11906841741284	7.29562956308702	11.93263492039905
H	4.17306776039633	7.50483884392667	12.15821928459529
H	2.76633836413888	6.49803172375821	12.60365797732472
H	3.05051861441662	6.92231016410107	10.90001553205558
C	0.78659219499315	8.23914466642920	11.76561455571555
H	0.41896856018910	7.42993591870240	12.41505032173289

H	0.13667590725265	9.11336765515013	11.89646729396202
H	0.69946297081704	7.90879236516214	10.72208539244529
O	3.58164831890199	10.07955712096537	7.76800722133640
O	5.51194589793704	10.05846170364922	8.97191173882689
O	2.05900135572094	10.07926884679736	10.25311774626057
O	4.00244962994449	10.05752776916340	11.43567693067570
Rh	2.77636473470711	11.53177456024158	8.98407764933120
Rh	4.80741485449187	11.53177473564619	10.23483206162626
C	4.76419983170879	13.40566898864552	8.00897973195526
C	5.34006799997312	14.50069187317036	7.08983902303610
C	6.73751756932073	14.04613092678629	6.54609681929874
H	7.41502482335550	13.94285753564641	7.40672654151797
H	7.11747502106137	14.87444824969044	5.92607086699535
C	6.73594138355588	12.75944734827309	5.75081660589463
C	6.61959865775425	12.74515606806893	4.35174618317658
H	6.57264136897981	13.68795762892085	3.80179154361878
C	5.54845755215037	15.76901110747396	7.94856413062644
H	5.99165748277683	16.56485980897962	7.33073894271254
H	6.21671241225716	15.56881178214374	8.79627061897411
H	4.59061987964414	16.14112761137682	8.34071240568428
C	4.37398633107499	14.80487355185743	5.93583106149327
H	4.80484928624663	15.59217724408309	5.29751976373987
H	3.40633039691659	15.15922181099141	6.31400608919008
H	4.18800190745920	13.91848537718822	5.31636688696337
O	3.58164843835542	12.98399167754118	7.76800693951239
O	5.51194520071605	13.00508874734003	8.97191263776473
C	2.80686231628608	13.40789319959315	11.19961243919034
C	2.24575909012011	14.50654009182556	12.12372090880878
C	2.36886813617070	14.04817640586726	13.61672590958486
H	1.97364823778231	14.87194553511869	14.23264068481075
H	3.43914966992423	13.95043025839205	13.85141870463867
C	1.65718953287103	12.75965463561820	13.96298750861693
C	0.35932710660216	12.74492662867170	14.49837323930976
H	-0.15003148313117	13.68741047211123	14.71358175131684
C	3.11906932810064	15.76791989013318	11.93263388490163
H	4.17306874122912	15.55871032678967	12.15821767192464
H	2.76633986049527	16.56551779616611	12.60365715675407
H	3.05051904821815	16.14123934460443	10.90001455162854
C	0.78659275066747	14.82440566601229	11.76561420749332
H	0.41896961654642	15.63361456208151	12.41505009432822
H	0.13667612829997	13.95018295475386	11.89646711025754

H	0.69946330954996	15.15475810457104	10.72208511493248
O	2.05900163815122	12.98428121237729	10.25311679120972
O	4.00244930554116	13.00602105133058	11.43567701413693

$BiRh(esp)_2$

C	5.98871134025707	9.27050206895756	8.95257299414402
C	6.36631917109868	8.07929741043054	8.04501766030006
C	7.61182525353614	8.48688359304115	7.18419237336635
H	8.43718204297558	8.70479824979049	7.87759965625243
H	7.89879232558855	7.59471861136451	6.60456002880197
C	7.41319344861513	9.65984205934056	6.24985478935551
C	7.03571203375675	9.47692713159795	4.90997633315954
H	6.91006384903704	8.46544627498757	4.51629026441518
C	6.83498853975919	10.57741052563030	4.07275835345199
H	6.55331500376064	10.42167198276254	3.02930479220948
C	7.59789371160587	10.97065738837726	6.71466117584800
H	7.92950031380540	11.12608165177658	7.74326831968088
C	6.78051419826768	6.90346666405748	8.95780040380769
H	7.10178301628482	6.05181977239838	8.33931062285222
H	7.60688209171862	7.18843499933451	9.62170426402481
H	5.93510409191971	6.57008584064573	9.57748318487633
C	5.18961685819430	7.65935516025233	7.15455205592552
H	5.48974655468855	6.80686706731980	6.52576271034968
H	4.32810250426931	7.34957647844118	7.76191581078888
H	4.86170114165237	8.47574589322276	6.50041809439804
C	3.97915412828682	9.74120327824268	12.36328156577843
C	3.23998445352345	8.80418521744149	13.34332164685146
C	3.15401037777399	9.50851054084783	14.74119330605508
H	2.67442953617772	8.78942344922644	15.42497605960794
H	4.18274237693534	9.66275915049885	15.09959005929999
C	2.40116090175568	10.82096989686030	14.77444814721035
C	1.04070569667145	10.87789959264662	15.11658184250824
H	0.51461509847714	9.96133450779647	15.39381872266676
C	0.36041797886950	12.09849406499310	15.12066126608318
H	-0.69354914597841	12.13202499982104	15.40353252536054
C	3.05672269425754	12.02023916727582	14.45516417084895
H	4.12398893845550	11.99440365678617	14.22567355536927
C	4.09168646322156	7.52543509214140	13.50482224790872
H	5.09834760864923	7.76487940237240	13.87149126655390
H	3.60573979680528	6.84669078639109	14.22220637110677

H	4.18822247244771	6.99265343304120	12.54749436531620
C	1.84271209823358	8.44055110450179	12.82221100681284
H	1.34772232719593	7.76631618535195	13.53858544191228
H	1.21483840038586	9.33048523607735	12.69024902500356
H	1.90371391726033	7.92748494283450	11.85275454567816
O	4.81516651753791	9.75744488202446	8.82495860938425
O	6.87418799747803	9.68761520656775	9.77327413146383
O	3.34997988539773	10.10163273222604	11.31203168833556
O	5.17074660627513	10.08846887369567	12.66404653288707
Rh	4.15176239858338	11.36885438553210	9.91102656099031
Bi	6.34511448016157	11.57000259630058	11.17120939374437
C	5.94331455913923	13.15788556150867	8.39801358831500
C	6.27775539346340	14.06955460206323	7.19747806957420
C	7.53208699426941	13.48558168278194	6.46186598951178
H	8.37321462951630	13.50381237501344	7.17172220906436
H	7.77607869416491	14.18883750173661	5.64877142304897
C	7.37425505590750	12.09027185262728	5.89888170669328
C	6.99499401384095	11.87577903158065	4.56431454323075
H	6.83442271124271	12.73164859685192	3.90391932768251
C	6.65185138037874	15.46135042694178	7.75312173599145
H	6.92799346629432	16.13027031106707	6.92382497055102
H	7.49830163470265	15.39242822692320	8.44936141412776
H	5.80178134781597	15.91563386659947	8.28347856398535
C	5.08338807175062	14.19022402870418	6.24141402906932
H	5.34683096810002	14.85510252189992	5.40467864029134
H	4.20970457994025	14.61428332159871	6.75430094229773
H	4.78861111690107	13.21586497577405	5.83224777005904
O	4.78361336080238	12.62183249238129	8.41704873446695
O	6.84101596525641	13.00474067411603	9.29305416598303
C	3.94873851174141	13.62388640516778	11.80265603759197
C	3.18898807455607	14.78699691505488	12.47687396760768
C	3.11981321288770	14.50999000228965	14.01736653116631
H	2.63309910709510	15.38702005133618	14.47365471389782
H	4.15178080444439	14.47312902372019	14.39715945948171
C	2.38503515562556	13.25164918958720	14.42334386139223
C	1.02428232251524	13.27680964218957	14.76944009446758
H	0.48571603926888	14.22727486667029	14.77312121217007
C	4.00890542893684	16.07752826972103	12.25338480687180
H	5.02385502121001	15.98138536187834	12.65983715649356
H	3.50906224604729	16.92318265833001	12.74930788720664
H	4.08413788811997	16.31349683424714	11.18152951120727

C	1.78447709738354	14.95503970852400	11.87987511095252
H	1.27369419787076	15.79449972801256	12.37629256724395
H	1.17492215128371	14.05235968990862	12.00903700299170
H	1.83972019756797	15.17311571117237	10.80470774662178
O	3.32772123881195	12.96632366936868	10.90025189053280
O	5.14585686551641	13.40011101742774	12.18600367541216

$Rh_2(esp)_2C(p\text{-}MeOPh)_2$ (19)

6	0.990494000	11.463204000	7.887830000
6	0.960164000	11.763131000	6.469498000
6	-0.131678000	12.476948000	5.906642000
1	-0.948147000	12.792615000	6.556993000
6	-0.166309000	12.834962000	4.561681000
1	-1.008735000	13.413676000	4.183326000
6	0.886222000	12.443970000	3.715348000
6	1.976677000	11.725915000	4.244434000
1	2.785144000	11.432837000	3.573563000
6	2.027525000	11.423376000	5.593269000
1	2.877421000	10.875316000	5.994357000
6	-0.137036000	13.440147000	1.787649000
1	0.126270000	13.551956000	0.730163000
1	-1.083767000	12.881913000	1.873546000
6	4.767806000	9.526269000	8.151352000
6	5.327928000	8.348211000	7.322681000
6	6.698855000	8.770464000	6.691194000
1	7.404144000	8.944596000	7.517398000
1	7.066398000	7.901162000	6.121547000
6	6.658049000	9.995356000	5.805051000
6	6.476657000	9.909597000	4.415396000
1	6.402947000	8.930112000	3.935863000
6	6.409466000	11.070135000	3.637910000
1	6.287244000	10.991227000	2.555048000
6	6.786587000	11.268132000	6.380592000
1	6.957905000	11.346822000	7.455409000
6	5.590903000	7.177686000	8.297042000
1	6.029049000	6.329884000	7.748155000
1	6.282441000	7.478421000	9.094307000
1	4.653500000	6.832555000	8.757943000
6	4.335286000	7.903675000	6.240034000
1	4.745132000	7.031547000	5.706676000

1	3.371947000	7.616195000	6.681381000
1	4.144626000	8.696503000	5.505097000
6	2.824103000	9.777427000	11.306504000
6	2.275449000	8.733479000	12.306736000
6	2.337321000	9.326981000	13.755800000
1	1.912646000	8.564004000	14.428568000
1	3.397967000	9.443453000	14.022901000
6	1.628604000	10.647323000	13.959453000
6	0.303395000	10.722879000	14.417234000
1	-0.235117000	9.805979000	14.669631000
6	-0.321283000	11.964237000	14.575721000
1	-1.342892000	12.013258000	14.958666000
6	2.304931000	11.845213000	13.683757000
1	3.343243000	11.799408000	13.352872000
6	3.204074000	7.499395000	12.260641000
1	4.241989000	7.778675000	12.484092000
1	2.869344000	6.756613000	13.001225000
1	3.176111000	7.023450000	11.269183000
6	0.844152000	8.315548000	11.945242000
1	0.490822000	7.558470000	12.662848000
1	0.152703000	9.167272000	11.961714000
1	0.805908000	7.879674000	10.937905000
8	3.585530000	9.933713000	7.868109000
8	5.522079000	9.995546000	9.065063000
8	2.052261000	10.132592000	10.347575000
8	4.012241000	10.194440000	11.513509000
8	0.949552000	12.717883000	2.379717000
45	2.722923000	11.510257000	8.931529000
45	4.843133000	11.569043000	10.211566000
1	-0.253279000	14.436735000	2.243148000
6	4.797507000	13.295800000	7.862942000
6	5.390183000	14.330285000	6.878375000
6	6.749550000	13.786888000	6.320196000
1	7.455008000	13.723934000	7.162194000
1	7.133796000	14.551834000	5.625201000
6	6.681664000	12.445167000	5.624955000
6	6.500312000	12.330301000	4.237164000
1	6.441046000	13.231238000	3.622010000
6	5.682631000	15.621064000	7.675460000
1	6.157869000	16.365585000	7.017961000
1	6.351285000	15.419185000	8.522339000

1	4.752457000	16.061533000	8.064239000
6	4.413336000	14.636880000	5.735163000
1	4.869545000	15.370178000	5.051052000
1	3.476719000	15.060634000	6.120404000
1	4.158470000	13.736999000	5.161938000
8	3.603807000	12.888371000	7.638136000
8	5.546154000	12.939310000	8.833207000
6	2.903100000	13.558052000	11.051725000
6	2.383044000	14.740089000	11.901813000
6	2.448644000	14.346372000	13.417019000
1	2.068951000	15.209667000	13.987173000
1	3.508385000	14.219856000	13.683133000
6	1.685082000	13.098149000	13.798735000
6	0.359191000	13.144653000	14.260040000
1	-0.136329000	14.109763000	14.390969000
6	3.334889000	15.935396000	11.673747000
1	4.370323000	15.667261000	11.920876000
1	3.026348000	16.780957000	12.307307000
1	3.302449000	16.268736000	10.625804000
6	0.954346000	15.134297000	11.500347000
1	0.641863000	16.016566000	12.080609000
1	0.237026000	14.326371000	11.693123000
1	0.899427000	15.385832000	10.433130000
8	2.118982000	13.096220000	10.148108000
8	4.079083000	13.140746000	11.308154000
6	-0.267590000	11.133051000	8.526114000
6	-0.545952000	11.475235000	9.872581000
6	-1.760011000	11.158855000	10.472880000
1	-1.940092000	11.474147000	11.499933000
6	-2.721625000	10.420259000	9.760416000
6	-2.457583000	10.027549000	8.433781000
1	-3.204802000	9.433708000	7.904704000
6	-1.267988000	10.392334000	7.828113000
1	-1.069915000	10.070899000	6.805464000
6	-4.239344000	10.379292000	11.618137000
1	-5.235880000	9.965539000	11.805486000
1	-3.517613000	9.934534000	12.321294000
8	-3.929244000	10.030930000	10.262314000
1	-4.263629000	11.472331000	11.756073000
1	0.197780000	12.040521000	10.430421000

BiRh(esp)$_2$C(*p*-MeOPh)$_2$ (20)

6	1.222157000	11.439945000	8.029542000
6	1.178324000	11.760136000	6.620057000
6	0.118410000	12.535178000	6.073189000
1	-0.665712000	12.900036000	6.737555000
6	0.088893000	12.901534000	4.730515000
1	-0.716820000	13.538133000	4.365420000
6	1.098617000	12.439993000	3.867182000
6	2.152673000	11.655845000	4.378856000
1	2.934425000	11.319172000	3.696204000
6	2.214973000	11.365742000	5.729459000
1	3.043621000	10.784536000	6.129930000
6	0.122139000	13.518213000	1.959589000
1	0.379760000	13.619651000	0.899548000
1	-0.863034000	13.032504000	2.052880000
6	5.031997000	9.424945000	8.149043000
6	5.444686000	8.283185000	7.186103000
6	6.698500000	8.761849000	6.376147000
1	7.507178000	8.941283000	7.099854000
1	7.007738000	7.914296000	5.743071000
6	6.509525000	9.994395000	5.518568000
6	6.171227000	9.897962000	4.158737000
1	6.060831000	8.913760000	3.696427000
6	6.000241000	11.050824000	3.386834000
1	5.756012000	10.963180000	2.325719000
6	6.682300000	11.273433000	6.070835000
1	6.982760000	11.361659000	7.116786000
6	5.868066000	7.073265000	8.048546000
1	6.234564000	6.264073000	7.398482000
1	6.663224000	7.350368000	8.752034000
1	5.014929000	6.683759000	8.623491000
6	4.301702000	7.871030000	6.250488000
1	4.627047000	7.026720000	5.622474000
1	3.420143000	7.552392000	6.823286000
1	3.994191000	8.688521000	5.587581000
6	2.945816000	9.680762000	11.513703000
6	2.207797000	8.670960000	12.429292000
6	2.113682000	9.291684000	13.865552000
1	1.633625000	8.534777000	14.507117000
1	3.142274000	9.426034000	14.232169000

6	1.364742000	10.602109000	13.980525000
6	0.008703000	10.643711000	14.343944000
1	-0.517611000	9.713009000	14.569673000
6	-0.662890000	11.866076000	14.444563000
1	-1.709453000	11.887585000	14.756471000
6	2.023323000	11.818687000	13.738074000
1	3.088045000	11.802358000	13.496824000
6	3.078321000	7.398140000	12.519195000
1	4.081452000	7.634648000	12.896276000
1	2.605613000	6.671039000	13.197331000
1	3.179507000	6.923516000	11.531834000
6	0.818440000	8.310811000	11.889899000
1	0.344731000	7.574291000	12.558115000
1	0.164338000	9.188394000	11.820218000
1	0.887578000	7.871020000	10.885752000
8	3.860393000	9.920769000	7.996401000
8	5.892765000	9.780671000	9.011587000
8	2.308078000	10.105391000	10.487131000
8	4.124810000	10.004580000	11.860302000
8	1.158356000	12.710490000	2.531351000
45	3.058505000	11.492148000	9.124376000
83	5.331815000	11.600763000	10.493232000
1	0.088126000	14.516119000	2.425354000
6	5.006368000	13.382503000	7.831898000
6	5.399972000	14.374013000	6.708217000
6	6.657140000	13.801573000	5.968614000
1	7.478029000	13.756671000	6.700450000
1	6.940863000	14.543307000	5.203957000
6	6.489705000	12.444433000	5.320425000
6	6.150798000	12.315182000	3.963862000
1	6.018181000	13.211530000	3.352791000
6	5.803893000	15.706470000	7.376756000
1	6.116686000	16.426837000	6.605208000
1	6.630731000	15.558668000	8.083684000
1	4.954655000	16.145066000	7.921836000
6	4.244533000	14.616478000	5.729724000
1	4.557611000	15.345059000	4.965718000
1	3.368203000	15.021891000	6.253309000
1	3.931443000	13.692609000	5.228275000
8	3.831343000	12.877207000	7.771262000
8	5.884762000	13.154254000	8.722844000

6	2.968163000	13.640671000	11.252753000
6	2.214955000	14.760812000	12.014556000
6	2.110943000	14.339421000	13.520567000
1	1.626341000	15.174374000	14.052138000
1	3.136699000	14.257532000	13.909652000
6	1.362315000	13.055329000	13.807959000
6	0.005000000	13.063688000	14.170811000
1	-0.523653000	14.015463000	14.262043000
6	3.077475000	16.040356000	11.936882000
1	4.080413000	15.864103000	12.346299000
1	2.596612000	16.848327000	12.509278000
1	3.181372000	16.380318000	10.895795000
6	0.829666000	15.034456000	11.415881000
1	0.347560000	15.859667000	11.963007000
1	0.174412000	14.156767000	11.472773000
1	0.909678000	15.323790000	10.359209000
8	2.333153000	13.064178000	10.299744000
8	4.149572000	13.380847000	11.634776000
6	-0.049332000	11.135562000	8.639298000
6	-0.316445000	11.428641000	10.002140000
6	-1.555605000	11.174473000	10.576874000
1	-1.724085000	11.452607000	11.616546000
6	-2.555428000	10.527845000	9.825986000
6	-2.301456000	10.161529000	8.489384000
1	-3.078250000	9.630849000	7.936051000
6	-1.088763000	10.480176000	7.906415000
1	-0.897705000	10.182517000	6.875570000
6	-4.107230000	10.546541000	11.656991000
1	-5.123887000	10.174831000	11.822128000
1	-3.419413000	10.064027000	12.368155000
8	-3.789477000	10.199049000	10.301756000
1	-4.085617000	11.638230000	11.803571000
1	0.462608000	11.912031000	10.587229000

$Rh_2(esp)_2C(H)(COOEt)$ (22)

6	4.665185000	9.559973000	8.101713000
6	5.157652000	8.396361000	7.216101000
6	6.566597000	8.753716000	6.631537000
1	7.262216000	8.865251000	7.476652000
1	6.894906000	7.878153000	6.048322000

6	6.612962000	9.997338000	5.771978000
6	6.486581000	9.944453000	4.374898000
1	6.399181000	8.977526000	3.873431000
6	6.483589000	11.121247000	3.620252000
1	6.400017000	11.067781000	2.532397000
6	6.756626000	11.253185000	6.379041000
1	6.894662000	11.305517000	7.459836000
6	5.313632000	7.157565000	8.127211000
1	5.708457000	6.314997000	7.539064000
1	6.002548000	7.359208000	8.957894000
1	4.343305000	6.850426000	8.544422000
6	4.153528000	8.096888000	6.094061000
1	4.522526000	7.254949000	5.487417000
1	3.173906000	7.821322000	6.505453000
1	4.008223000	8.962541000	5.435797000
6	2.821782000	9.770697000	11.340593000
6	2.257883000	8.730312000	12.332628000
6	2.464563000	9.249453000	13.795986000
1	2.057899000	8.473471000	14.464662000
1	3.547141000	9.307446000	13.981313000
6	1.828864000	10.585605000	14.109750000
6	0.546431000	10.686825000	14.672894000
1	-0.004194000	9.779660000	14.934019000
6	-0.023419000	11.940102000	14.916060000
1	-1.014446000	12.007042000	15.369049000
6	2.522408000	11.770138000	13.820629000
1	3.531888000	11.705544000	13.413524000
6	3.079952000	7.432739000	12.160283000
1	4.149453000	7.616305000	12.328154000
1	2.733361000	6.678115000	12.882695000
1	2.952162000	7.015142000	11.150189000
6	0.774605000	8.446456000	12.056226000
1	0.413551000	7.678864000	12.757937000
1	0.158882000	9.346376000	12.179391000
1	0.626539000	8.073806000	11.034024000
8	3.492988000	10.020178000	7.864250000
8	5.450733000	9.972924000	9.018719000
8	2.042772000	10.164591000	10.401121000
8	4.027577000	10.147303000	11.520954000
45	2.723837000	11.563290000	9.016486000
45	4.855843000	11.531040000	10.224173000

6	4.786977000	13.295841000	7.894394000
6	5.388975000	14.310042000	6.896726000
6	6.763462000	13.773127000	6.371633000
1	7.443615000	13.691387000	7.232258000
1	7.168965000	14.551117000	5.703841000
6	6.707375000	12.447190000	5.645541000
6	6.580449000	12.365767000	4.249588000
1	6.565119000	13.280474000	3.652537000
6	5.650588000	15.618319000	7.678068000
1	6.119153000	16.360048000	7.013152000
1	6.316621000	15.441399000	8.532865000
1	4.710091000	16.048405000	8.052874000
6	4.427247000	14.579583000	5.731745000
1	4.887424000	15.299986000	5.037358000
1	3.481676000	15.003480000	6.092038000
1	4.194461000	13.662592000	5.175864000
8	3.570317000	12.936557000	7.705574000
8	5.544889000	12.908997000	8.846394000
6	3.034620000	13.536377000	11.202785000
6	2.563424000	14.696298000	12.106977000
6	2.719325000	14.273368000	13.607737000
1	2.393785000	15.135113000	14.212661000
1	3.791420000	14.122681000	13.802897000
6	1.952825000	13.036409000	14.018986000
6	0.669032000	13.107880000	14.583220000
1	0.214003000	14.082667000	14.775002000
6	3.498187000	15.898321000	11.843326000
1	4.547015000	15.634759000	12.033449000
1	3.218597000	16.733856000	12.502829000
1	3.408596000	16.245027000	10.803051000
6	1.112209000	15.086796000	11.793687000
1	0.819704000	15.939204000	12.426234000
1	0.418313000	14.258500000	11.983655000
1	1.001570000	15.380559000	10.741886000
8	2.215463000	13.124776000	10.310709000
8	4.212161000	13.085081000	11.404608000
6	0.280576000	12.502860000	7.362941000
8	-0.056771000	12.104099000	6.249694000
6	0.946172000	11.559361000	8.260249000
8	0.102941000	13.753626000	7.833446000
6	-0.635193000	14.671219000	6.959920000

1	-1.133939000	15.351380000	7.661925000
1	-1.390416000	14.097021000	6.405770000
6	0.292811000	15.415858000	6.016540000
1	-0.287519000	16.149332000	5.436212000
1	1.068469000	15.957981000	6.574684000
1	0.776668000	14.726531000	5.312469000
1	0.325526000	10.684803000	8.511922000

$BiRh(esp)_2C(H)(COOEt)$ (23)

6	5.006084000	9.427675000	8.150763000
6	5.339200000	8.293376000	7.151675000
6	6.613731000	8.711042000	6.340589000
1	7.444940000	8.807391000	7.055283000
1	6.851881000	7.866814000	5.673476000
6	6.494358000	9.981709000	5.528577000
6	6.097667000	9.958618000	4.181422000
1	5.897292000	9.002162000	3.692928000
6	5.975424000	11.147343000	3.456992000
1	5.679278000	11.115779000	2.406584000
6	6.778319000	11.223850000	6.116335000
1	7.125522000	11.253168000	7.151001000
6	5.684674000	7.031225000	7.972842000
1	5.953419000	6.210789000	7.290310000
1	6.527752000	7.218634000	8.649981000
1	4.822589000	6.701407000	8.571342000
6	4.159203000	7.996274000	6.216230000
1	4.430174000	7.172103000	5.538846000
1	3.271421000	7.691720000	6.787270000
1	3.887082000	8.868871000	5.609932000
6	2.990186000	9.703357000	11.573413000
6	2.189183000	8.720578000	12.460390000
6	2.154414000	9.288962000	13.920651000
1	1.646540000	8.532038000	14.539953000
1	3.193666000	9.358017000	14.275271000
6	1.469748000	10.627221000	14.088802000
6	0.117846000	10.720177000	14.456035000
1	-0.452129000	9.809655000	14.655587000
6	-0.498629000	11.967844000	14.583353000
1	-1.546236000	12.027893000	14.884693000
6	2.181725000	11.816335000	13.868124000

1	3.243345000	11.758098000	13.618754000
6	2.961164000	7.382072000	12.487415000
1	3.980168000	7.520168000	12.872341000
1	2.431742000	6.666758000	13.134954000
1	3.024143000	6.943098000	11.480871000
6	0.771309000	8.498017000	11.917111000
1	0.232946000	7.795694000	12.572073000
1	0.203282000	9.434854000	11.866857000
1	0.801180000	8.070357000	10.905730000
8	3.852856000	9.972636000	8.035008000
8	5.896608000	9.726120000	9.008350000
8	2.370599000	10.189130000	10.563566000
8	4.191830000	9.952230000	11.901952000
45	3.170467000	11.537541000	9.220433000
83	5.484732000	11.511763000	10.576074000
6	5.280107000	13.357497000	7.999322000
6	5.703051000	14.362015000	6.899768000
6	6.906733000	13.748052000	6.106835000
1	7.744976000	13.630279000	6.810098000
1	7.208346000	14.502832000	5.362509000
6	6.636245000	12.430814000	5.414656000
6	6.236223000	12.376103000	4.069877000
1	6.142225000	13.301558000	3.496314000
6	6.193389000	15.647483000	7.602514000
1	6.521324000	16.375418000	6.845160000
1	7.031541000	15.435052000	8.278533000
1	5.383407000	16.110325000	8.185554000
6	4.534005000	14.696244000	5.963451000
1	4.862627000	15.438683000	5.219810000
1	3.690257000	15.116850000	6.525687000
1	4.168521000	13.808398000	5.432954000
8	4.081474000	12.918055000	7.934746000
8	6.147028000	13.054815000	8.879288000
6	3.125330000	13.610628000	11.352126000
6	2.425576000	14.742294000	12.143438000
6	2.366796000	14.328559000	13.653539000
1	1.936403000	15.183371000	14.199772000
1	3.402254000	14.205875000	14.004118000
6	1.573957000	13.077579000	13.959881000
6	0.220727000	13.138757000	14.330144000
1	-0.268591000	14.110382000	14.431269000

6	3.308718000	16.004935000	12.026051000
1	4.319106000	15.817822000	12.412113000
1	2.857045000	16.826856000	12.601859000
1	3.390482000	16.332464000	10.979014000
6	1.023460000	15.031815000	11.592125000
1	0.560894000	15.846184000	12.170679000
1	0.373011000	14.150392000	11.648092000
1	1.076959000	15.343848000	10.540453000
8	2.456047000	13.084607000	10.395383000
8	4.306343000	13.297291000	11.708091000
6	0.658219000	12.664484000	7.699357000
8	-0.497899000	12.229920000	7.769888000
6	1.668952000	11.652245000	7.908000000
8	1.005380000	13.951650000	7.536581000
6	-0.104376000	14.902700000	7.402393000
1	0.321402000	15.848515000	7.759899000
1	-0.917260000	14.593382000	8.072616000
6	-0.573286000	15.008581000	5.960324000
1	-1.341926000	15.792587000	5.881191000
1	0.259097000	15.275661000	5.294803000
1	-1.014543000	14.063565000	5.617622000
1	1.719878000	10.919891000	7.087062000

REFERENCES

(1) Neese, F. *Wiley Interdisciplinary Reviews-Computational Molecular Science* **2012**, *2*, 73.

(2) (a) Becke, A. D. *Phys. Rev. A.* **1988**, *38*, 3098. (b) Lee, C.; Yang, W.; Parr, R. G. *Phys. Rev. B.* **1988**, *37*, 785.

(3) Pantazis, D. A.; Chen, X. Y.; Landis, C. R.; Neese, F. *J. Chem. Theory Comput.* **2008**, *4*, 908.

(4) (a) Eichkorn, K.; Treutler, O.; Öhm, H.; Häser, M.; Ahlrichs, R. *Chem. Phys. Lett.* **1995**, *240*, 283. (b) Eichkorn, K.; Weigend, F.; Treutler, O.; Ahlrichs, R. *Theor. Chem. Acc.* **1997**, *97*, 119.

(5) (a) Van Lenthe, E.; Van Der Avoird, A.; Wormer, P. E. S. *J. Chem. Phys.* **1998**, *108*, 4783. (b) Van Lenthe, E.; Snijders, J. G.; Baerends, E. J. *J. Chem. Phys.* **1996**, *105*, 6505.

(6) (a) Jonas, V.; Thiel, W. *Organometallics* **1998**, *17*, 353. (b) Jonas, V.; Thiel, W. *J. Chem. Phys.* **1995**, *102*, 8474.

(7) Romelt, C.; Ye, S.; Bill, E.; Weyhermuller, T.; Van Gastel, M.; Neese, F. *Inorg. Chem.* **2018**, *57*, 2141.

(8) Reiss, G. J.; Frank, W.; Schneider, J. *Main. Group. Met. Chem.* **1995**, *18*, 287.

(9) Filatov, A. S.; Napier, M.; Vreshch, V. D.; Sumner, N. J.; Dikarev, E. V.; Petrukhina, M. A. *Inorg. Chem.* **2012**, *51*, 566.

(10) Sunderland, T. L.; Berry, J. F. *Dalton Trans.* **2016**, *45*, 50.

(11) Doyle, M. P.; Winchester, W. R.; Protopopova, M. N.; Kazala, A. P.; Westrum, L. J. *Org. Synth.* **1996**, *73*, 13.

(12) Dias, H. V.; Browning, R. G.; Polach, S. A.; Diyabalanage, H. V.; Lovely, C. J. *J. Am. Chem. Soc.* **2003**, *125*, 9270.

(13) Hansen, J.; Li, B.; Dikarev, E.; Autschbach, J.; Davies, H. M. *J. Org. Chem.* **2009**, *74*, 6564.

(14) Flores, J. A.; Badarinarayana, V.; Singh, S.; Lovely, C. J.; Dias, H. V. *Dalton Trans.* **2009**, 37, 7648.

(15) Komine, N.; Flores, J. A.; Pal, K.; Caulton, K. G.; Mindiola, D. J. *Organometallics* **2013**, *32*, 3185.

(16) Flores, J. A.; Pal, K.; Carroll, M. E.; Pink, M.; Karty, J. A.; Mindiola, D. J.; Caulton, K. G. *Organometallics* **2014**, *33*, 1544.

(17) Rustoy, E. M.; Baldessari, A. *Eur. J. Org. Chem.* **2005**, *21*, 4628.

(18) Müller, P.; Tohill, S. *Tetrahedron* **2000**, *56*, 1725.

(19) Rosenberg, M. L.; Krivokapic, A.; Tilset, M. *Org. Lett.* **2009**, *11*, 547.

(20) Werle, C.; Goddard, R.; Fürstner, A. *Angew. Chem., Int. Ed.* **2015**, *54*, 15452.

(21) Espino, C. G.; Fiori, K. W.; Kim, M.; Du Bois, J. *J. Am. Chem. Soc.* **2004**, *126*, 15378.

(22) Werle, C.; Goddard, R.; Philipps, P.; Fares, C.; Fürstner, A. *J. Am. Chem. Soc.* **2016**, *138*, 3797.